Journal of
Applied Research on Science and Technology

TCI Journal Classification tier 1
Approved during 2022-2024

INSTITUTE OF RESEARCH AND DEVELOPMENT
RAJAMANGALA UNIVERSITY OF TECHNOLOGY THANYABURI

ISSN Online 2773-9473

Volume 22 Issue 3
September – December 2023

JARST RMUTT

Journal of Applied Research on Science and Technology (JARST)
E-ISSN : 2773-9473
Vol. 22 No. 3 September – December 2023

The Journal of Applied Research on Science and Technology (JARST) aims to disseminate and share knowledge and ideas in the form of high-quality articles to academia, professionals, industrialists, and an important forum for exchanging knowledge between researchers, academics, faculty members and students both national and international, which will bring benefits in building academic cooperation and network that will lead to sustainable use of research. The articles that will be published in this journal must not be ever presented and published or in the evaluation processes in any other journals. Any piracy occurred will be only under the responsibility of the authors. The journal will not be responsible for such consequences.

Aims and Scope

The scope of the journal includes the following areas of research: General Engineering, General Materials Science, General Agricultural and Biological Sciences, General Computer Science, and General Mathematics with particular emphasis on issues that deepen in the basic and applied research. The JARST includes full length original, novel research articles and review articles. Accepted articles are immediately available online and are freely accessible without any restrictions or any other obligations to researchers and scholarly people globally.

Review Process

1. Evaluation by the Editor-in-Chief

The Editor-in-Chief will see whether the topic and theme of the article are appropriate and congruent with the stipulated objectives and format of the Journal. Plagiarism and benefits relating to theory and business contribution will also be investigated. The submitted paper may be returned to the author for preliminary revising or, if the aforesaid criteria are not met, rejected.

2. Evaluation by Review

All submitted manuscripts must be reviewed by at least two expert reviewers in the related fields. Reviewers will evaluate the quality of submitted article for publication via the double-blinded review system.

3. Evaluates the Reviews

The Editor-in-Chief make decision for article publication based on the external readers' evaluation. The said decision is either accepting the article for publication, rejecting it, or resending it back to the author for further elaborating revision.

Period of Issued Journal

The Journal of Applied Research on Science and Technology (JARST) will be 3 issues/year, as follows:

1st issue: January - April
2nd issue: May - August
3rd issue: September - December

Advisory Board

Contact

Institute of Research and Development, Rajamangala University of Technology Thanyaburi (RMUTT)
39 Moo 1, Klong 6, Khlong Luang Pathum Thani 12110 Thailand
Website: https://ph01.tci-thaijo.org/index.php/rmutt-journal/index
Phone: +66 2 5494492, +66 2 5494681
Fax: +66 2 5494680
Email: jarst@rmutt.ac.th

Editorial Note

The Journal of Applied Research on Science and Technology (JARST) is an academic journal prepared by Institute of Research and Development, Rajamangala University of Technology Thanyaburi (RMUTT). The JARST aims to disseminate and share knowledge and ideas in the form of high-quality articles related General Engineering, General Materials Science, General Agricultural and Biological Sciences, General Computer Science, and General Mathematics to researchers, academics, faculty members and students both national and international.

This journal published ten research articles. Each of the research articles presented interesting concepts such as Cold pressed virgin coconut oil production: Enhancing energy efficiency through a closed tunnel hot air generation system, Microencapsulation of moringa oil in bio-polymer by simple solvent evaporation technique, Development of a photoelectrocatalytic method to improve the efficiency of *E. coli* removal, Cellulose rubber foam composite use as oil absorbent, Boosting cordycepin production through plant-based oils for vegetarian consumption, Optimization of ballistic vest for protective atrocity and stabbing, 2-Keto-gluconate production and purification by thermotolerant acetic acid bacterium *Nguyenibacter vanlangensis* KKS-R1, The effect of maltodextrin on properties of salted egg yolk, Fabrication of PS-TiO_2 hybrid via mini-emulsion polymerization: Study the effect of crosslink on the photocatalytic properties of the hybrid, and Real-time vehicle detection system on the highway. Therefore, this journal is a channel disseminating the knowledge areas of physical sciences and life sciences which related persons could apply it for further benefits.

Lastly, the editorial team would like to considerably thank you for supporting and pushing forward this journal to occur and well accomplish. We are hopeful of your good cooperation and continuing support in the future.

Editorial Team

Contents

Research Articles	Page
Cold pressed virgin coconut oil production: Enhancing energy efficiency through a closed tunnel hot air generation system *Boonthong Wasuri, Sombat Hathairattananon and Bopit Chainok*	**251713**
Microencapsulation of moringa oil in bio-polymer by simple solvent evaporation technique *Oraya Kullawong, Amorn Chaiyasat and Preeyaporn Chaiyasat*	**253714**
Development of a photoelectrocatalytic method to improve the efficiency of *E. coli* removal *Kanyarat Hmud, Masashi Hatamoto, Somporn Moonmangmee, and Chatchai Ponchio*	**253893**
Cellulose rubber foam composite use as oil absorbent *Poptorn Klaykhem, Pruttipong Pantamanatsopaopa and Warunee Ariyawiriyana*	**254006**
Boosting cordycepin production through plant-based oils for vegetarian consumption *Watcharin Yuttavanichakul, Nipaporn Kanthong and Nuntaporn Pungsungvorn*	**254104**
Optimization of ballistic vest for protective atrocity and stabbing *Montien O-thongkham and Sujira Khojitmate*	**254151**
2-Keto-gluconate production and purification by thermotolerant acetic acid bacterium *Nguyenibacter vanlangensis* KKS-R1 *Phongsupha Chanthachaiyaphum, Somporn Moonmangmee and Duangtip Moonmangmee*	**254506**
The effect of maltodextrin on properties of salted egg yolk *Sansanee Thimthong, Nanoln Dangsungwal and Supuksorn Masavang*	**254045**
Fabrication of PS-TiO_2 hybrid via mini-emulsion polymerization: Study the effect of crosslink on the photocatalytic properties of the hybrid *Thanapong Phetsombun, Tanapak Metanawin and Siripan Metanawin*	**253757**
Real-time vehicle detection system on the highway *Pisanu Kumeechai*	**254011**

Received: March 23, 2023 | Revised: September 10, 2023 | Accepted: September 11, 2023

Cold pressed virgin coconut oil production: Enhancing energy efficiency through a closed tunnel hot air generation system

Boonthong Wasuri[1], Sombat Hathairattananon[2] and Bopit Chainok[2*]

[1]Industrial Arts Department, Faculty of Science and Technology, Nakhon Pathom Rajabhat University, Nakhon Pathom 73000, THAILAND

[2]Intelligent Control Innovation Department, Faculty of Science and Technology, Nakhon Pathom Rajabhat University, Nakhon Pathom 73000, THAILAND

[*]Corresponding author: bopitch@npru.ac.th

ABSTRACT

The primary aim of this paper was to research and develop a closed tunnel house hot air production system, focusing on cost reduction in the cold-pressed coconut oil production process. The study's scope was centered on a case analysis of Tropicana Oil Co. Ltd. situated in Sampran district, Nakhon Pathom province. The research encompassed the design of a system capable of generating hot air and conserving thermal energy within a closed tunnel house environment. This included developing and constructing a prototype system tailored to this purpose. One of the key objectives was to assess the system's efficiency within the closed tunnel house setup. The broader goal was to enhance air temperature while reducing moisture content before initiating the coconut drying process. It was achieved through an electricity-powered hot air-drying technique, the process aimed to efficiently eliminate water or moisture from dried coconut, priming it for the subsequent cold-pressed oil extraction phase. The resulting system is anticipated to yield multiple benefits. It's projected to curtail energy consumption for operators by minimizing temperature losses within the system. This is facilitated by augmenting natural heat to elevate the air and container temperature during baking. Furthermore, this research unveiled insights into the optimal tunnel house configuration as a highly effective heat source. It also advanced knowledge in creating low-humidity heat storage systems and measurement/control mechanisms tailored for specific tasks. These innovations are anticipated to have applications beyond the coconut oil industry, extending to other sectors reliant on heat energy for production processes.

Keywords: Cold pressed virgin coconut oil production, Heat production, Closed tunnel hot air, Temperature control

INTRODUCTION

The company specializes in producing cold-pressed coconut oil and its derivatives [1]. Their target audience primarily comprises health-conscious consumers who prioritize chemical-free products [2]. With an annual production capacity of 125,000 liters, the company utilizes 1,500 kilograms of shredded coconut per day to create an array of cold-pressed coconut oil products and its derivatives. The production process involves extracting moisture from shredded coconut meat, followed by oil extraction through pressing and subsequent filtration to yield pure coconut oil [3]. A pertinent challenge in this process is the management of materials and energy during coconut meat baking. The energy consumed in drying, primarily resulting from water evaporation, constitutes a significant proportion of the overall electricity usage [4]. This expense stands at approximately 111,375 baht per month (based on a production cycle of 25 days per month), or an estimated 1,336,500 baht annually.

Hence, by elevating the temperature of the grated coconut meat, the utilization of aluminum shells and air during the baking process could potentially lead to a substantial reduction in energy costs. This reduction, estimated at a minimum of 200,475.00 baht annually, is based on a conservative 15 percent decrease in losses. Considering the system's construction cost of approximately 300,000 baht, the projected time for payback stands at approximately 1.50 years or, equivalently, 18 months.

Among the various stages, the dehumidification process of coconut shavings stands out as the most energy-intensive due to the requirement to convert electrical energy into heat [5]. In response, the authors proposed an innovative approach to harness natural energy within the production process. The objective is to substantially curtail energy usage in the coconut meat baking stage, with a target reduction of no less

DOI: 10.60101/jarst.2023.251713

than 15% of the prevailing consumption. The crux of this approach is developing a specialized system that autonomously generates low-humidity hot air within a controlled tunnel environment. This innovative solution leverages a green tunnel as a heat accumulator, thereby augmenting the production of cold-pressed coconut oil. The adoption of this approach signifies a remarkable stride toward sustainable energy utilization in the production process.

The prototype from research was applied to the factory roof to harness solar heat as an energy source, aiming to reduce electricity consumption costs by more than 15 percent.

MATERIALS AND METHODS

a) Tools and equipment

Measurement and Temperature Control [6]: This tool is designed to both restrict temperature within predetermined values and adjust it within specified ranges or times; use this tool to measure and control the humidity and temperature of the baking simulation system. The temperature control system is depicted in Figure 1 (a).

Temperature and Humidity sensors and Data-logger [7]: Incorporating multiple functions, this low-power data logger integrates a high-sensitivity detector to rapidly and precisely capture temperature and humidity levels. Figure 1 (b) illustrates the temperature and humidity sensors and data-logger.

(a) (b)

Figure 1 (a) Measurement and temperature control; (b) Temperature and Humidity sensors and data-logger.

Air Velocity Meter: This device serves the purpose of measuring wind speed, temperature, and humidity, making it suitable for both general wind speed measurement and air conditioning applications. Featuring a 30 mm propeller, it's also capable of humidity measurement. Refer to Figure 2 (a) for the representation of the air velocity meter, which research uses to measure the air velocity of the air pump in the drying system model.

Illumination and solar sensor: Comprising a light sensor and a display, with illumination accuracy ±5% at 25°C, the illumination and solar sensor operates on the principle of converting incident light energy into current. This current's magnitude is determined by the light striking the sensor. The illumination and solar sensor interpret this current to calculate the light intensity and display the value on the screen. To visualize the illumination, a solar sensor measures the light intensity and ultraviolet light of the outside sun in the house; consult Figure 2 (b).

(a) (b)

Figure 2 (a) Air velocity meter; (b) Illumination and solar sensor.

Thermal Infrared Camera [8]: This instrument specializes in surface temperature measurement, accuracy ±2%, ±2°C, used to measure the heat outside the greenhouse. Operating based on the principle of non-contact and non-destructive infrared radiation assessment, it effectively gauges the temperature of an object's surface. The thermal imaging camera integrates key components like a lens, infrared detector, electronic circuitry, and a display. Here's how it works: the infrared detector captures emitted infrared rays from the target object via the device's lens, converting these rays into an electrical signal. This received infrared radiation encompasses both the target object's emission and reflections from other sources or surfaces, then, the electronic circuitry processes and transmits this data to the display. Refer to Figure 3 for a visual depiction of the thermal infrared camera.

Figure 3 Thermal Infrared Camera.

b) Prototype of closed tunnel hot air production system

The tunnel's design incorporates a semi-circular shape to minimize wind-related influences. Moreover, it is adept at accommodating a thermal energy-retaining covering material. Fabricated from

DOI: 10.60101/jarst.2023.251713

stainless steel, the tunnel boasts dimensions of 3 meters in width, 4 meters in length, and 2 meters in height. Figure 4 presents a block diagram illustrating the tunnel's configuration. Utilize a temperature sensor to measure the temperature within the house. If the temperature reaches the specified level, the device will activate the air pump to draw hot air from the house through the grated coconut meat. This process aims to facilitate moisture absorption from the coconut meat, causing it to evaporate. For a more comprehensive understanding, both the interior and exterior of the tunnel are showcased in Figure 5 and Figure 6, respectively.

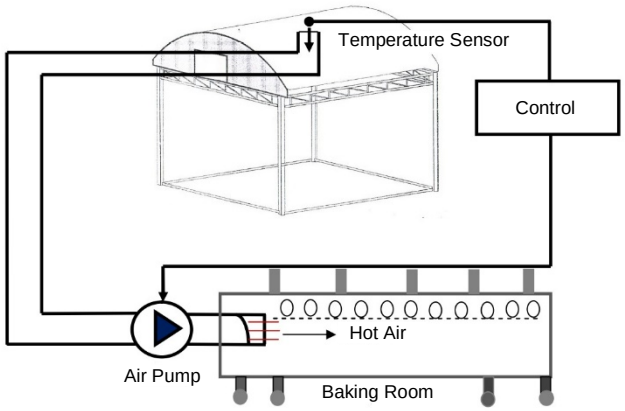

Figure 4 System Block diagram.

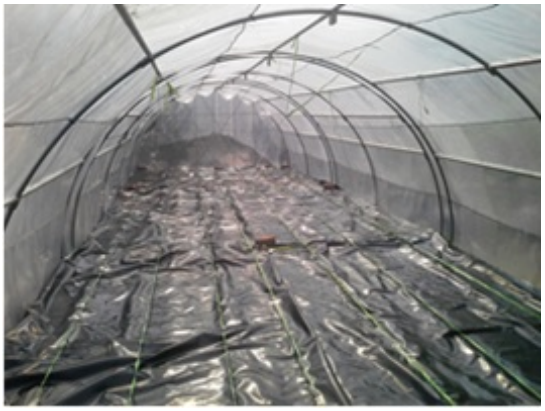

Figure 5 Inside tunnel.

Figure 6 Outside tunnel.

RESULTS AND DISCUSSIONS

a) Efficiency of closed tunnel hot air production system

Conducting temperature data storage tests inside and outside the tunnel has been instrumental in elevating heat levels from external sources. The system's efficiency capitalizes on varying heat accumulation, contingent on weather conditions. Notably, daytime temperatures within the tunnel can rise 10-20°C higher than the exterior, while nighttime temperatures align closely. A heat collector with heat-storing materials [9] has been implemented to optimize this. This augmentation prolongs heat accumulation and transfer from the baking process, effectively leveraging the stored heat within the tunnel for continuous baking. The evolved system for generating hot air within the enclosed tunnel encompasses a control unit that monitors the tunnel's temperature. Activation of the blower to draw in hot air for subsequent baking is triggered when the tunnel's temperature surpasses 50°C [10]. Furthermore, the terminal section of the tube exhibits temperatures 15-25°C higher than outdoors. The incorporation of 9 temperature sensors inside and outside the tunnel, coupled with the strategic placement of black plastic on the tunnel floor, has notably augmented heat accumulation via solar radiation [11]. This approach has demonstrated the capacity to elevate temperatures beyond the original range of 20-35 degrees Celsius, as illustrated in Figure 7.

Figure 7 Using a blower to draw hot air to use in baking.

Experiments were also conducted to expel hot air from the tunnel, employing an air pump to channel the heated air for drying to eliminate moisture from the shredded coconut meat. During the experiment, 400 g of shredded coconut was placed in an aluminum tray and subsequently positioned within an incubator. This incubator harnessed the hot air sourced from the tunnel to facilitate moisture removal. Impressively, the outcome revealed that approximately 200 g of moisture could be effectively eradicated within 90 minutes. Refer to Figure 8 and Figure 9 for visual insights into this process.

DOI: 10.60101/jarst.2023.251713

Figure 8 Coconut meat before baking, weight 400 g.

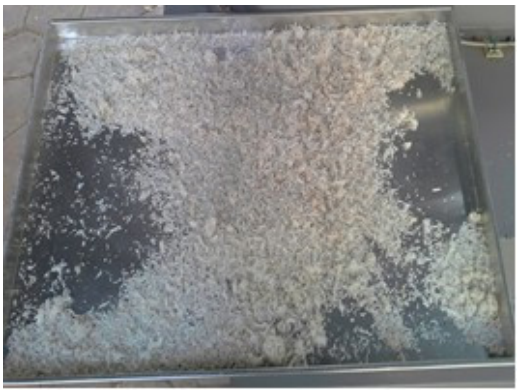

Figure 9 Coconut meat before baking, weight 200 g.

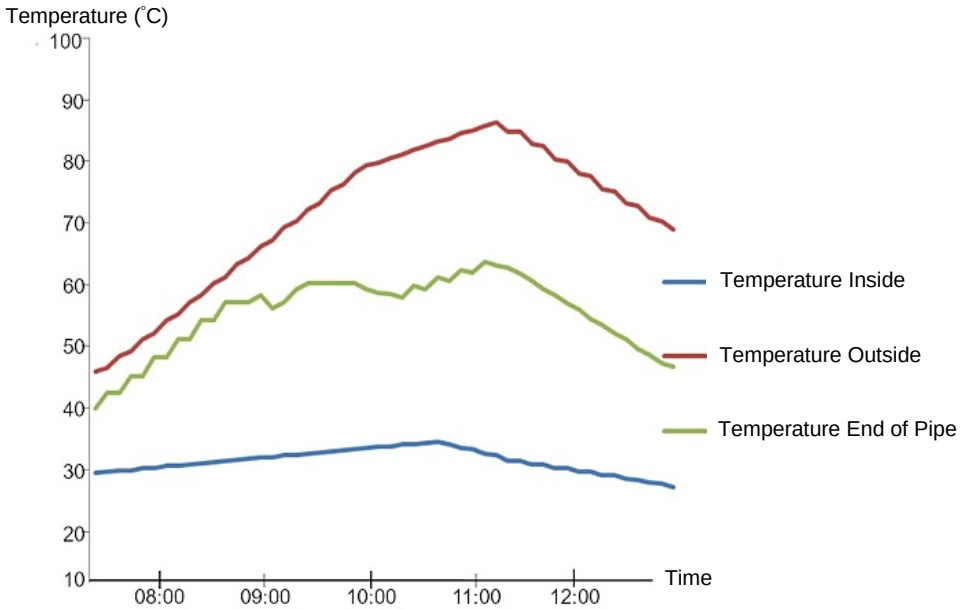

Figure 10 Coconut meat before baking, weight 200 g.

Figure 10 illustrates the temperature records at the end of the pipe employed for baking. By utilizing an air pump to direct the heated air externally, a comparison was drawn between the interior and exterior temperatures and the temperature outside the tunnel. This analysis revealed that the average temperature at the pipe's end used in the baking process ranged from 40 to 60°C. This was in contrast to the average temperature within the tunnel, which ranged from 46 to 8°C, and the average temperature outside the tunnel, falling within the range of 27 to 33 degrees Celsius.

The amount of coconut introduced to the incubator per drying cycle remained consistent at 10 kg, originating from coconuts with an initial moisture content of about 65% (wb = 0.6) before drying. Before entering the factory production line, the desired moisture content was targeted at 25% (wb = 0.25). As a result, the volume of water to be eliminated per cycle equated to 5.3 kg.

In daily operations, baking occurred thrice, each lasting 150 minutes. Consequently, the aggregate water removal from raw materials amounted to 15.9 kg per day, equivalent to an energy demand of 95.40 MJ per day (factoring in water evaporation at 6.0 MJ/kg). The heat at the end of the pipe can be estimated using Equation (1).

$$Q_{blow} = (C_p(T_{in} - T_{out}) + L_v \Delta q)\varrho_a F_v \qquad (1)$$

Where, Q_{blow} is ventilation heat, C_p is the specific heat capacity of dry air, T_{in} is the inside tunnel temperature, T_{out} is the outside tunnel temperature, L_v is the latent heat of vaporization, Δq is the specific humidity difference from inside to outside, ϱ_a is the density of air, F_v is the volumetric airflow due to ventilation.

Given these parameters, the amount of heat is calculated to be 101.835 MJ.

b) The efficiency of the closed tunnel hot air production system in Phase II

After placing black plastic on the tunnel floor to facilitate heat accumulation from the sun's rays, various measurements were taken, including wind speed, light intensity, and temperature at

DOI: 10.60101/jarst.2023.251713

different locations. This resulted in significant heat buildup within the tunnel, raising the temperature by approximately 20 - 35 degrees Celsius compared to its initial state.

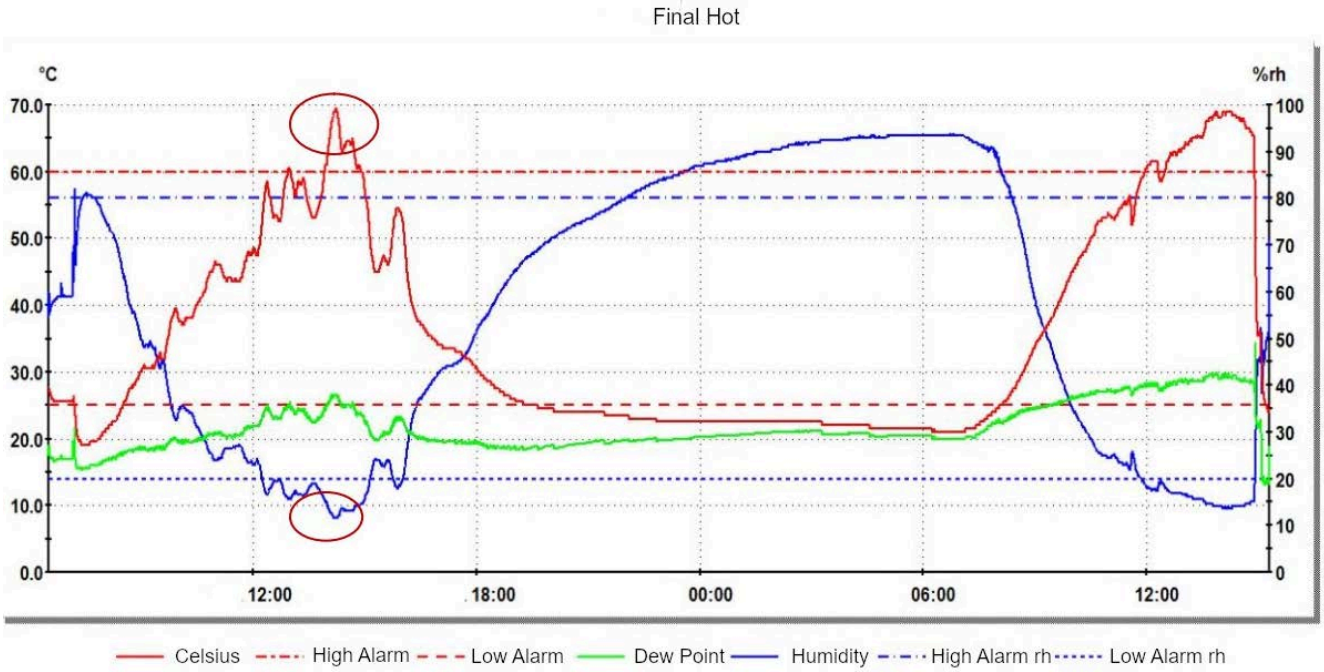

Figure 11 The temperature inside tunnel.

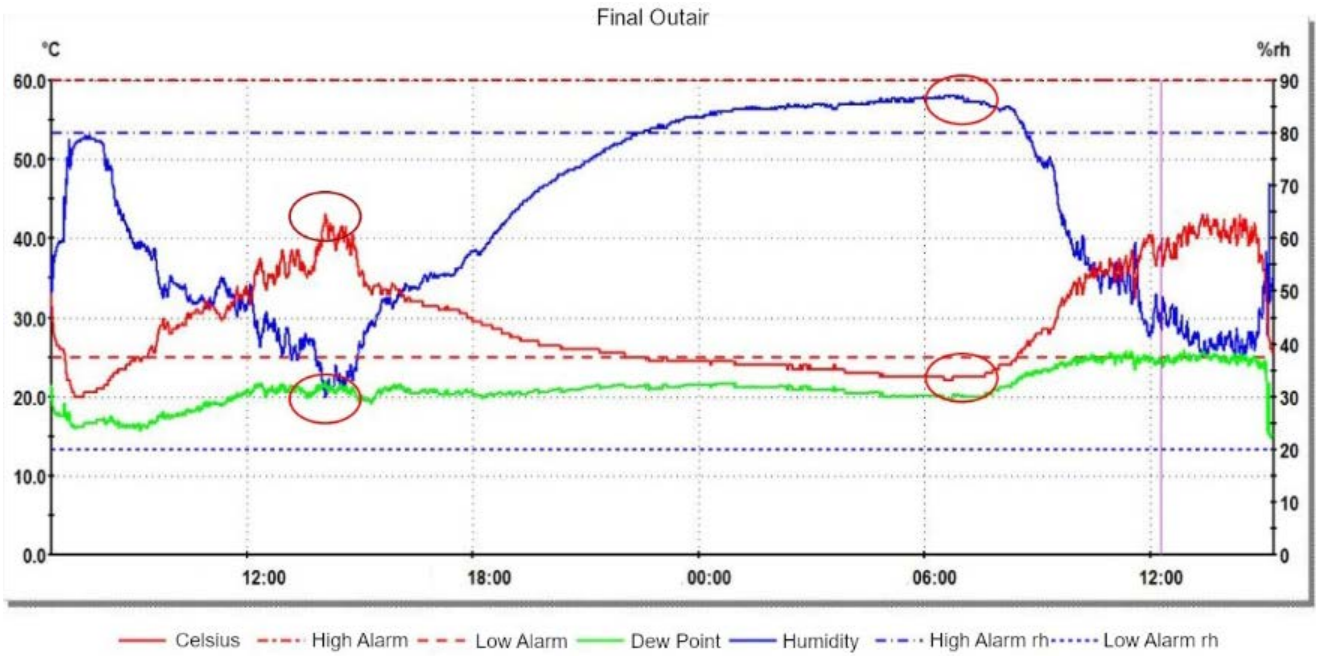

Figure 12 The temperature outside tunnel.

Based on the data presented in Figure 11 and Figure 12, the maximum temperature difference recorded was approximately 26 degrees Celsius, fluctuating between 70 and 44 degrees Celsius. In practical experimentation, hot air from the tunnel was tested using an air pump for drying. This involved employing hot air to eliminate moisture from 500 grams of shredded coconut placed in an aluminum tray. Subsequently, the tray was positioned in a cabinet that utilized the hot air from the tunnel for moisture removal. The results indicated that around 270 grams of moisture (water) could be extracted within approximately 150 minutes, as illustrated in Figure 13.

The heat energy balance of the tunnel is based on the principle that energy entering the system equals energy leaving the system. In other words, the net energy is zero. This balance can be achieved through analyzing various factors contributing to energy input and output.

DOI: 10.60101/jarst.2023.251713

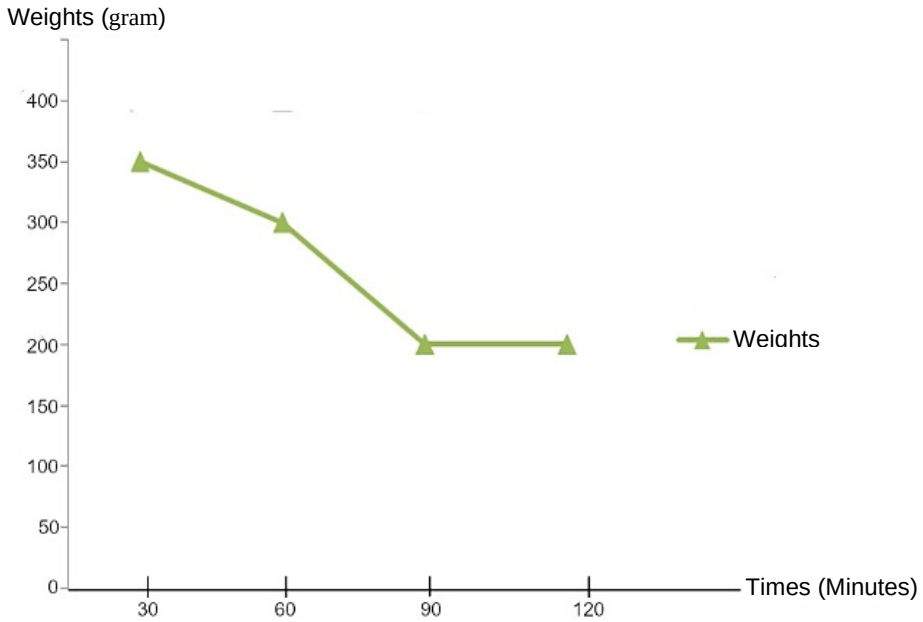

Figure 13 Dehumidification process in 500 grams of grated coconut meat.

c) Heat energy balance of the tunnel

Energy entering the system is equal to energy leaving the system. Net energy is equal to energy entering the tunnel - energy leaving the tunnel since the net energy equals zero.

1) The energy that is put into the tunnel consists of:

a) Heat energy from solar radiation.

b) Heat energy, exothermic heat for condensation.

2) Energy from the tunnel

a) Transfer of heat energy, input into various joints around the tunnel.

b) Heat energy and ventilation transfer to the outside depending on the environment.

c) Transfer of heat energy, suction of warm air by fan.

d) Tunnel data collection

The author used a thermal infrared camera to collect temperature data at various points in the tunnel: the temperature at the surface of the covering material, the temperature under the tunnel, the temperature out of the tunnel, and the temperature at which the blower enters the cabinet.

CONCLUSION

The company aims to reduce thermal energy consumption. Tropicana Oil Co., Ltd. strives to transform the factory into a green facility that relies on natural sources to conserve energy and contribute to environmental preservation. Thus, the findings of this research demonstrate how solar heat can be harnessed for heating purposes in the factory, the prototype was applied to the factory roof to harness solar heat as an energy source for the factory, aiming to reduce electricity consumption costs by more than 15 percent.

REFERENCES

1. Tropicana Organic Cold-Pressed Virgin Coconut Oil [Internet]. Tropicana (2002) Co.,Ltd, c2022. [cited 2022 Jan 1]. Available From: https://tropicanaoil.com/en/.
2. Valente FX, Cândido FG, Lopes LL, Dias DM, Carvalho SDL, Pereira PF, et al. Effects of coconut oil consumption on energy metabolism, cardiometabolic risk markers, and appetitive responses in women with excess body fat. Eur J Nutr. 2018;57(4): 1627-37.
3. Ng YJ, Tham PE, Khoo KS, Cheng CK, Chew KW, Show PL. A comprehensive review on the techniques for coconut oil extraction and its application. Bioprocess Biosyst Eng. 2021;44(9): 1807-18.
4. Obeng GY, Amoah DY, Opoku R, Sekyere CKK, Adjei EA, Mensah E. Coconut wastes as bioresource for sustainable energy: Quantifying wastes, calorific values and emissions in Ghana. Energies. 2020;13(9):2178-91.
5. Nejib N, Bawadekji A, El-Bary AA, Becheikh N, Alassaf Y, Hassan GE, et al. Greentunnel desalination by humidification–dehumidification using a novel green packing material. Water. 2022;14(6):869-83.
6. Measurement and temperature control [Internet]. Thai Tadashi Calibration and Service Co., Ltd., c2022. [cited 2022 Jan 1]. Available From: https://www.thaitadashi.com/th/.

DOI: 10.60101/jarst.2023.251713

7. Temperature and Humidity sensors and data-logger [Internet]. DIGILIFE Pluit Jakarta, Indonesia, c2022. [cited 2022 Jan 1]. Available From: http://digilifeweb.com/.
8. Fluke TIS20 Thermal Imaging Camera Bundle [Internet]. RS Components Co., Ltd., c2022. [cited 2022 Jan 1]. Available From: https://th.rs-online.com/web/p/thermal-imaging-cameras/.
9. Ashutosh A, Pitchumani R, Chauhan R. Solar air heating systems with latent heat storage - A review of state-of-the-art. Journal of Energy Storage. 2022;48:104013.
10. Chen Q, Li N. Energy, emissions, economic analysis of air-source heat pump with radiant heating system in hot-summer and cold-winter zone in China. Energy Sustain Dev. 2022;70:10-22.
11. Alkilani MM, Sopian K, Alghoul MA, Sohif M, Ruslan MH. Review of solar air collectors with thermal storage units. Renewable and Sustainable Energy Reviews. 2011;15(3):1476-90.

DOI: 10.60101/jarst.2023.251713

Received: August 8, 2023 | Revised: September 7, 2023 | Accepted: September 10, 2023

Microencapsulation of moringa oil in bio-polymer by simple solvent evaporation technique

Oraya Kullawong[1], Amorn Chaiyasat[1, 2] and Preeyaporn Chaiyasat[1, 2*]

[1]Department of Chemistry, Faculty of Science and Technology, Rajamangala University of Technology Thanyaburi, Pathum Thani 12110, THAILAND

[2]Advanced Materials Design and Development (AMDD) Research Unit, Faculty of Science and Technology, Rajamangala University of Technology Thanyaburi, Pathum Thani 12110, THAILAND

[*]Corresponding author: p_chaiyasat@mail.rmutt.ac.th

ABSTRACT

Moringa oil (MO) contains various bioactive components and pharmacology. It is attractive to use as a raw ingredient in various products. However, there are limitations on its direct utilization, especially MO's instability and hastening the active ingredient's degradation from external environmental factors, including temperature, humidity, oxidation, light, and heat. To solve these problems, in this work, microencapsulation of MO using different biopolymers as cellulose acetate butyrate (CAB), ethyl cellulose (EC), and poly(L-lactic acid) (PLLA) were carried out by a simple solvent evaporation technique. The prepared polymer microcapsule suspensions were highly colloidal stable for all types of biopolymers and ratios. The spherical biopolymer capsules were formed to a micrometer size after solvent evaporation under all conditions. However, when the microcapsules were dried, aggregation was found with the polymer microcapsules at a ratio of PLLA to MO of 50:50 for all three types of polymers, possibly due to the low amount of polymer to completely encapsulate all of MO. When polymer contents increased to 70%, the dried spherical polymer microcapsules were smoothly produced. Using 70% polymers, the PLLA microcapsule surface was smoother than the polymer microcapsules prepared by CAB and EC which exhibited the dent or hole on the outer surface. Micrometer size, spherical polymer capsules with a core-shell morphology were fabricated. Due to the higher hydrophilicity of the polymer than the MO, the polymer moves outward, forming a strong shell around the MO. Then, all three biopolymers can be used for the microencapsulation of MO at a suitable polymer to MO ratio. However, using PLLA at a ratio of PLLA to MO of 70:30 presented the highest encapsulation efficiency (74.08%), which may be due to its high molecular weight. Because of the non-toxicity and biodegradability of biopolymers, the fabricated microcapsules would be well applied in cosmetic products.

Keywords: Moringa oil, Microencapsulation, Solvent evaporation technique, Poly-L-lactic acid

INTRODUCTION

Moringa oil (MO) is extracted from parts of the Moringa tree (Drumstick tree), such as leaves and seeds. It is currently widely used as a raw material in the health and beauty industries [1]. MO is a natural extract that is 100% natural, providing a chemical-free and non-toxicity. Because of its high antioxidant activity and other beneficial biological and pharmacological properties, natural MO is increasingly used as an anti-inflammatory, anti-bacterial, anti-fungal, etc. [2-4]. Although MO can be used directly, several restrictions remain such as the accelerated degradation of bioactive components when exposed to environmental variables, including heat, light, oxygen depletion, and moisture or the reaction with other ingredients in the product. This decreases the product's efficiency and lifespan. To solve these problems, encapsulation technology is therefore applied for encapsulating active substances.

Encapsulation has gained much attention and is widely applied to various products. If a highly efficient encapsulation technology is used to store MO, the quality of MO will be improved. This active ingredient is more stable after being encapsulated because it is protected from degradation or reaction with the external environment and other substances in the emulsion of the cosmetic product [5, 6]. The encapsulation increases the response's surface area and controls the release of bioactive components at the desired rate as well. Physical encapsulation

DOI: 10.60101/jarst.2023.253714

techniques are typically simple, repeatable, and scalable for the industry. Among encapsulation techniques, solvent evaporation is one of the most simple and efficient methods to produce polymer capsules encapsulating various substances [7-9]. It is a repeatable, low-cost, and easily scalable method for the industry at room temperature. The microencapsulation of jasmine oil with polymethyl methacrylate was successfully prepared by solvent evaporation in an oil-in-water emulsion (O/W) system. The amount of encapsulated jasmine oil (23.04%) and the encapsulation efficiency was 72% [7]. Therefore, the possibility of using this technique in the production of microcapsules is interesting.

Biopolymers, produced from renewable resources, are used in pharmaceutical and cosmetic products because of their non-toxicity. Various groups of them were used especially polyesters, including poly(L-lactic acid) (PLLA), and cellulose derivatives. PLLA and cellulose derivatives e. g., ethyl cellulose (EC) and cellulose acetate butyrate (CAB) are well-known biopolymers used for the preparation of polymer capsules [10-13]. Because they are natural polymers that are readily available, inexpensive, non-toxic, biologically friendly, and can be biodegradable [14-17]. Spherical CAB microcapsules containing diltiazem resin were prepared by solvent evaporation. The microcapsule size increased with the concentration of CAB [18]. EC microcapsules were produced for the encapsulation of probiotics to extend their viability [13]. In addition, the EC microcapsules were successfully prepared and applied to the fabric samples. The textile surfaces desired antibacterial activities have been achieved to an acceptable level [19]. As well as a well-known biopolymer, PLLA capsules containing linalool were non-toxic to human cells and prevented the growth of *Staphylococcus aureus*, *Escherichia coli*, and *Candida albicans* [20]. The spherical and smooth surface PLLA microcapsules containing phase change material, Rubitherm 27 (RT27), with a high encapsulation efficiency (96%) were fabricated [21]. Polymer capsules encapsulating vitamin E were successfully created utilizing PLLA by the conventional solvent evaporation method. Meanwhile, the particle size distribution of PLLA capsules encapsulating vitamin E using phase inversion emulsification is narrower than that of capsules produced via the conventional solvent evaporation method [9].

Therefore, in this work, the preparation of polymer microcapsules encapsulating MO by a simple solvent evaporation method is studied. Various types of biopolymers e. g. PLLA, EC, and CAB are used. The influences of polymer types and polymer: MO ratios on the microcapsule morphology and encapsulation efficiency of MO are determined.

MATERIALS AND METHODS

Moringa oil (MO; Organic Thailand), cellulose acetate butyrate (CAB; laboratory reagent, Sigma-Aldrich; Mn 77,000), ethyl cellulose (EC; laboratory reagent, Sigma-Aldrich; Mn 51,000), and poly(L-lactic acid) (PLLA; commercial, B. C. Polymer Marketing; Mn 95,000) were used as biopolymers as received. Polyvinyl alcohol (PVA; analytical reagent, Sigma-Aldrich) was used as a surfactant. Ethyl acetate (EA; 99.9% purity, RCI Labscan), dichloromethane (DCM; 99.9% purity, RCI Labscan), and tetrahydrofuran (THF; analytical reagent, RCI Labscan) were used as solvents as received. Deionized water was used throughout the study.

Solubility test

Biopolymers of CAB, EC, and PLLA were used as microcapsule shells. Before the microcapsule preparation, polymers and MO must be completely dissolved in appropriate solvent. Then, solubility testing was studied at a 1:1 ratio of polymers to MO with various polymer:solvent ratios under the conditions shown in Tables 1 and 2. CAB and EC could be dissolved in EA and PLLA in DCM.

Table 1 Reagent amounts for the solubility testing of CAB and PLLA.

Chemicals		Polymer: MO: Solvent		
		1: 1: 5	1: 1: 6	1: 1: 7
MO	g	1.00	1.00	1.00
Polymer[a]	g	1.00	1.00	1.00
Solvent[b]	g	5.00	6.00	7.00

[a]; CAB and PLLA
[b]; CAB using EA and PLLA using DCM

Table 2 Reagent amounts for the solubility testing of EC.

Chemicals		EC: MO: EA		
		1: 1: 9	1: 1: 10	1: 1: 11
MO	g	1.00	1.00	1.00
EC	g	1.00	1.00	1.00
EA	g	9.00	10.00	11.00

Preparation of polymer microcapsule encapsulated MO

PLLA was homogeneously dissolved in DCM and CAB, or EC was homogeneously dissolved in EA before mixed with MO as an oil phase. It was then poured into PVA aqueous solution before homogenizing at 5,000 rpm for 5 min to generate oil droplet suspension. The suspension was gentle stirred for solvent evaporation to produce polymer microcapsules, as shown in Fig. 1. The effects of the type of polymer and the ratio of polymer:MO were investigated under the conditions listed in Table 3.

DOI: 10.60101/jarst.2023.253714

JOURNAL OF APPLIED RESEARCH ON SCIENCE AND TECHNOLOGY

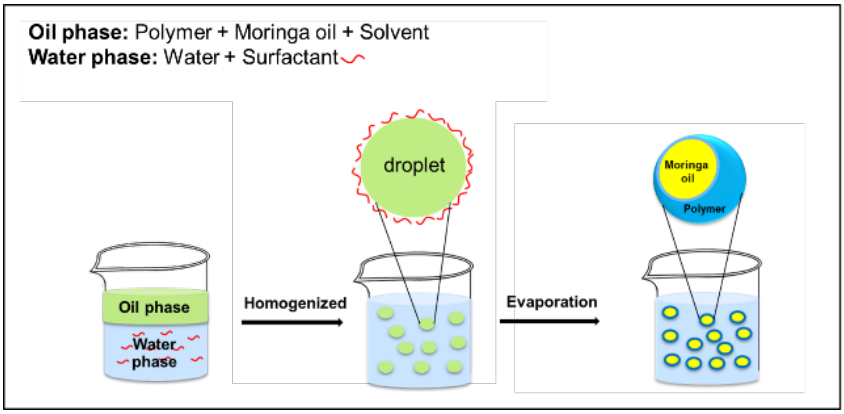

Figure 1 Schematic diagram for the preparation of polymer microcapsules by solvent evaporation.

Table 3 Reagent amounts for the preparation of polymer microcapsules by solvent evaporation at various polymer:MO ratios.

Chemicals			Polymer: MO	
			50: 50	70: 30
Oil	Polymer [a]	g	1.25	1.75
	MO	g	1.25	0.75
Water	PVA	g	0.23	0.23
	Water	g	22.5	22.5

[a]; PLLA, CAB and EC

Characterization

The suspensions of oil droplets and microcapsules encapsulated MO after solvent evaporation were observed with an optical microscope (OM, SK-100EB & SK-100 ET, Seek Inter) to investigate their shape and inner structure. A scanning electron microscope (SEM, JSM 6510, JEOL) was used to study the surface morphology of the microcapsules by distribution of the dried polymer microcapsules on a nickel SEM stub and coating it with Au. The amount of the encapsulated MO was measured by a UV-visible spectrophotometer (Lambda 35, Perkin Elmer). About weighed 0.1 g polymer microcapsules and MO standards [22, 23] were dissolved in tetrahydrofuran and adjusted the volume of the solution to 25 ml. Then, the absorbances of the standard solution at various concentrations and the sample solution were measured at λ_{max} 293 nm. The measured absorbance of the sample solution was used to calculate the amount of MO encapsulated in polymer microcapsules using the following equations.

MO in polymer microcapsules from experimental 0.1 g.

$$W_{MO;\ Capsules\ (Exp.)}\ (mg) = \frac{[MO]\ x\ 25\ mL}{1{,}000} \quad (1)$$

MO in polymer microcapsules from theory 0.1 g.

$$W_{MO;\ Capsules\ (th.)}\ (mg) = \frac{W_{MO;\ th.}\ (g)\ x\ 0.1\ g}{[PLLA\ (g) + MO\ (g)]}\ x\ 1{,}000 \quad (2)$$

Loading efficiency (%)

$$\%L_E = \frac{W_{MO;Capsules\ (Exp.)}\ (mg)}{0.1\ (g)\ x\ 10^3}\ x\ 100 \quad (3)$$

$$\%L_{th} = \frac{W_{MO;Capsules\ (th.)}\ (mg)}{0.1\ (g)\ x\ 10^3}\ x\ 100 \quad (4)$$

Encapsulation efficiency (%)

$$\%EE = \frac{\%L_E}{\%L_{th}} \times 100 \quad (5)$$

Where

[MO] is the concentration of MO from calculation with the calibration curve (mg/L).

$W_{MO;Capsules\ (Exp.)}$ is the weight of MO (mg) in the polymer microcapsule obtained from the experiment.

$W_{MO;Capsules\ (th.)}$ is the weight of MO (mg) in the polymer microcapsule from the calculation.

L_E is the loading percent of MO in polymer microcapsule obtained from the experiment.

L_{th} is the loading percent of MO in polymer microcapsule obtained from the calculation.

RESULTS AND DISCUSSIONS

Solubility test

In the first step of polymer capsule preparation, the homogeneous oil droplets are required. Then, it is necessary to completely dissolve polymer and core substance using the appropriate solvent type and ratio. CAB, EC, and PLLA, biopolymers, were used as polymer shells at a ratio of polymer: MO of 1: 1. The prepared oil-phase solution requires the minimum amount of solvent that can completely dissolve the MO and polymer providing low viscosity suitable for internal phase separation. Polymers and MO were completely dissolved giving clear solutions for all conditions, as shown in Fig. 2. EA, a non-toxic solvent [24, 25], is a good solvent for CAB and EC. 1: 1: 6 and 1: 1: 10 were suitable ratios for CAB: MO: EA and EC: MO: EA, respectively, giving a homogeneous solution with low viscosity. For PLLA, DCM was used as a good solvent [26] at a ratio of 1: 1: 6.

DOI: 10.60101/jarst.2023.253714

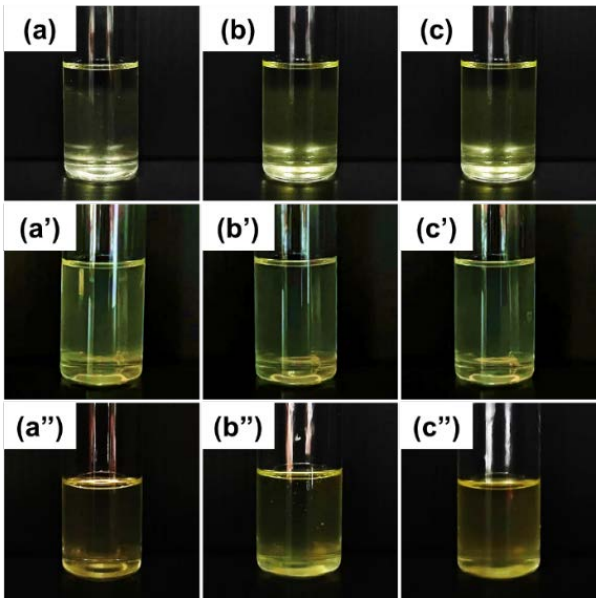

Figure 2 Solubility testing of CAB (a-c), EC (a'-c'), and PLLA (a''-c'') in a solvent at various ratios of Polymer: MO: solvent (w/w); CAB: MO: EA at 1: 1: 5 (a), 1: 1: 6 (b), and 1: 1: 7 (c); EC: MO: EA at 1: 1: 9 (a'), 1: 1: 10 (b'), and 1: 1: 11 (c') and PLLA: MO: DCM at 1: 1: 5 (a''), 1: 1: 6 (b''), and 1: 1: 7 (c'').

Effect of polymer type and polymer: MO ratio

The polymer microcapsules were prepared by the solvent evaporation method in an O/W system. The colloidally stable milky suspensions of the polymer/MO microcapsules were obtained for all types and ratios, as shown in Fig. 3.

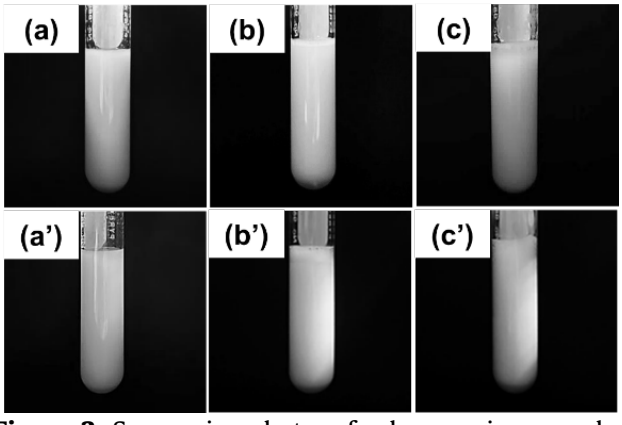

Figure 3 Suspension photos of polymer microcapsules using polymer: MO at 50: 50 (a-c) and 70: 30 (a'-c') of various polymers: CAB (a, a'), EC (b, b'), and PLLA (c, c').

The prepared polymer microcapsules were observed by optical microscope. Spherical microcapsules in a micrometer size were formed in all conditions, as shown in Figs. 4 and 5. The microcapsules were well distributed without coagulation. After drying, the polymer microcapsule powders were observed by SEM. Using EC, the microcapsules were spherical for both EC:MO ratios, as shown in Figs. 6b and 5b'. Rough surfaces or holes, which may be due to the evaporation of solvent were observed. However, at low polymer content (50:50), some aggregation of polymer microcapsules was found. The non-spherical CAB/MO microcapsules were formed with large aggregation due to the distribution of oil on the surface at a ratio of 50: 50, as shown in Fig. 6a. It is possibly because the low amount of CAB is not enough to completely encapsulate all of MO. When CAB content is increased to 70%, more stable spherical CAB/MO microcapsules are produced, as shown in Fig. 6a'. Similarly with CAB, stable PLLA/MO microcapsules at a ratio of 50:50 could not be prepared in dry state. Some aggregation of PLLA/MO microcapsules was clearly observed, as shown in Fig. 6c. In contrast, the spherical PLLA/MO microcapsules were formed at a ratio of 70:30 as shown in Fig. 6c'. Moreover, smoother surface than in the other conditions was clearly observed. After crushed, a core-shell morphology of the prepared microcapsules using all three types of polymers were clearly observed, as shown in Fig. 7. Phase separation of dissolved polymer chains and MO is smoothly proceeded during solvent evaporation leading to the formation of polymer shell enveloping the MO core. Therefore, all three types of polymers can be used to prepare stable MO encapsulated microcapsules at appropriate polymer to MO ratio.

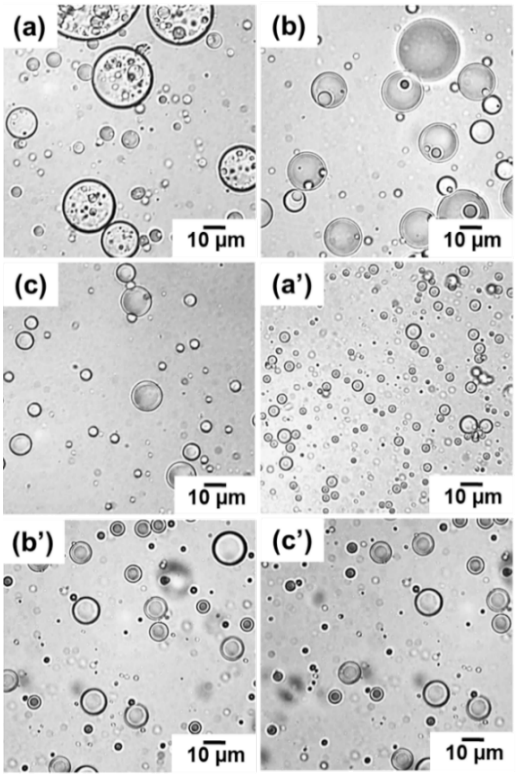

Figure 4 Optical micrographs of polymer microcapsules using Polymer: MO at 50: 50 before (a-c) and after solvent evaporation (a'-c') of various polymers: CAB (a, a'), EC (b, b'), and PLLA (c, c').

DOI: 10.60101/jarst.2023.253714

JOURNAL OF APPLIED RESEARCH ON SCIENCE AND TECHNOLOGY

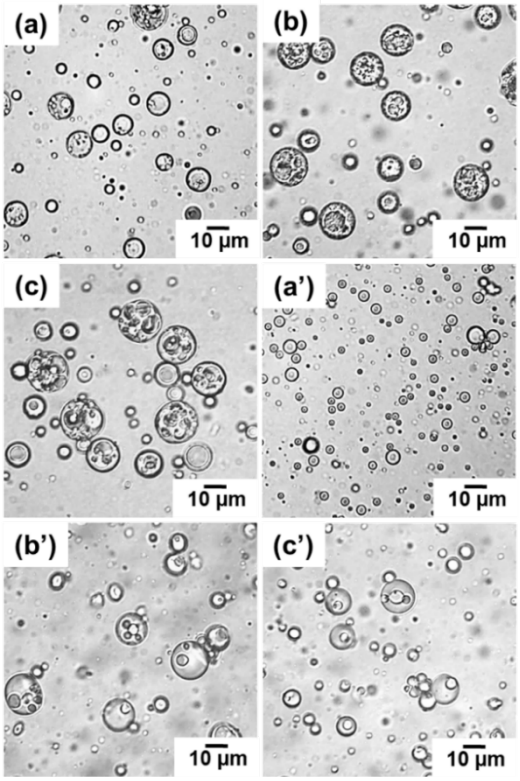

Figure 5 Optical micrographs of polymer microcapsules using Polymer: MO at 70: 30 before (a-c) and after solvent evaporation (a'-c') of various polymers: CAB (a, a'), EC (b, b'), and PLLA (c, c').

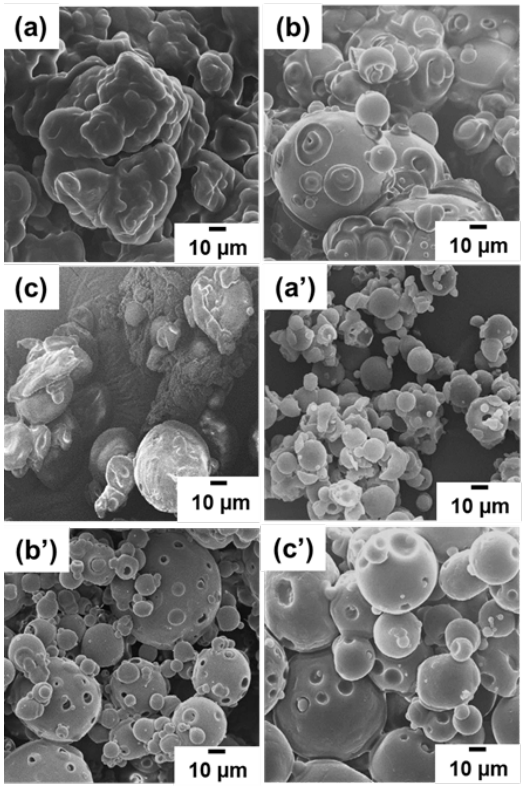

Figure 6 SEM micrographs of polymer microcapsules using Polymer: MO at 50: 50 (a-c) and 70: 30 (a'-c') of various polymers: CAB (a, a'), EC (b, b'), and PLLA (c, c').

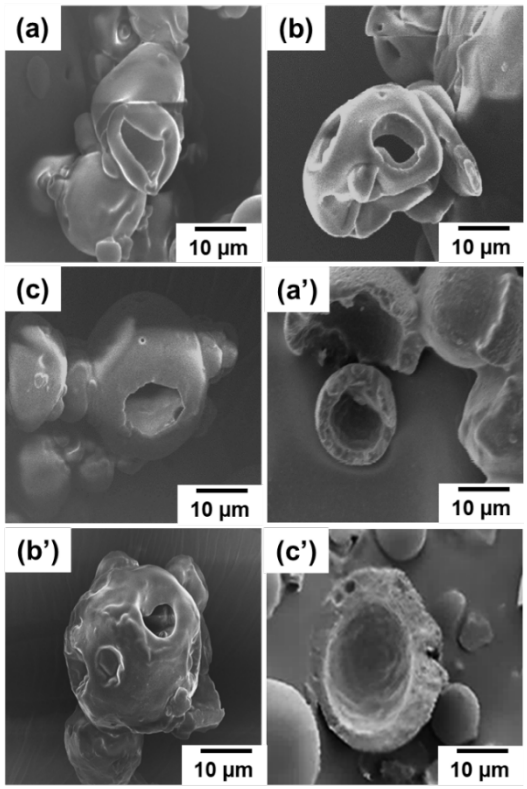

Figure 7 SEM micrograph of crushed microcapsules using Polymer: MO at 50: 50 (a-c) and 70: 30 (a'-b') of various polymers: CAB (a, a'), EC (b, b'), and PLLA (c, c').

Encapsulation efficiency

The loading and encapsulation efficiency (EE) of the prepared microcapsules were determined by UV-visible spectrophotometry, as shown in Table 4. The measured absorbance peak of the sample solution was used to calculate the amount of MO encapsulated in polymer microcapsules compared with the standard peaks of MO, as shown in Fig. 8. Corresponding with SEM observation, polymer microcapsules of all three kinds of polymers at a ratio of 50:50 presented low EE which may be due to the excessive amount of MO. Polymers are insufficient to totally encapsulate MO. EE increased with polymer content due to the larger amount of polymer needed to encapsulate MO for all types of polymers. Using PLLA at a ratio of 70:30 provided the highest EE at about 74%. This is probably due to the higher MW of PLLA (95,000 g/mol) used in this work than that of CAB (77,000 g/mol) and EC (51,000 g/mol). Using high MW polymer chains, MO was encapsulated more completely and formed a stronger shell [27]. As seen, only the dent occurs on the outer surface of PLLA microcapsules, as shown in Fig.7b' and 7c'. In contrast, the lowest %EE values of both EC/MO microcapsule ratios were obtained. Due to the rough surface with holes of the EC/MO microcapsules, some MO may loss to the outer region resulting in a reduction of the encapsulated MO content.

DOI: 10.60101/jarst.2023.253714

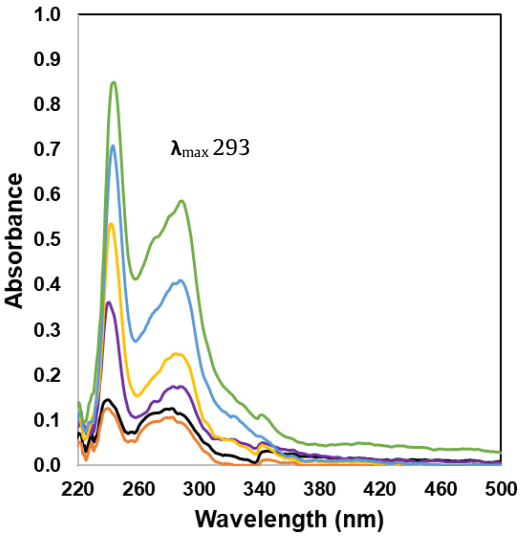

Figure 8 UV spectrum of MO standards (ppm); 2,000 (—), 4,000 (—), 6,000 (—), 8,000 (—) and 10,000 (—) and EC/MO microcapsules solution (—).

Table 4 Loading and encapsulation efficiency of polymer microcapsules prepared by solvent evaporation using various types of polymer.

Microcapsules	Polymer: MO	Loading (%wt)		Encapsulation (%wt)
		Experiment	Theory	
CAB/MO	50: 50	15.98 ± 0.17	50.44	31.68 ± 0.33
	70: 30	12.72 ± 0.03	30.02	42.37 ± 0.10
EC/MO	50: 50	12.34 ± 0.30	50.38	24.49 ± 0.58
	70: 30	12.28 ± 0.29	30.06	40.85 ± 0.96
PLLA/MO	50: 50	14.38 ± 0.16	51.13	28.12± 0.31
	70: 30	22.41 ± 0.29	30.25	74.08 ± 0.96

CONCLUSIONS

The stable spherical biopolymer microcapsules were successfully produced by simple solvent evaporation. All three biopolymer kinds, CAB, EC, and PLLA, can be used to produce spherical microcapsules encapsulating MO at appropriate polymer to MO ratio. Using PLLA, a stable core-shell microcapsule with a smooth surface were formed. The loading and EE increased with polymer content. Using a ratio of PLLA:MO of 70:30 presented the highest loading and EE. Because of its non-toxicity and biodegradability, it would be well applied to cosmetic products.

ACKNOWLEDGEMENT

This research project is supported by National Research Council of Thailand (NRCT): Contract No. N41A640334. The authors also thank BEAUTY MY COSMED CO., LTD. for their support.

REFERENCES

1. Ozioko FUOFU. Synthesis and study of properties of biolubricant based on Moringa oleifera oil for industrial application. AU Journal of Technology. 2014;17(3):137-42.
2. Cáceres A, Saravia A, Rizzo S, Zabala L, De Leon E, Nave F. Pharmacologie properties of Moringa oleifera. 2: Screening for antispasmodic, antiinflammatory and diuretic activity. J Ethnopharmacol. 1992;36(3):233-7.
3. Mahmood KT, Mugal T, Haq IU. Moringa oleifera: a natural gift-A review. Journal of Pharmaceutical Sciences and Research. 2010;2(11):775.
4. Ferreira RS, Napoleão TH, Santos AFS, Sá RA, Carneiro-da-Cunha MG, Morais MMC, et al. Coagulant and antibacterial activities of the water-soluble seed lectin from Moringa oleifera. Lett Appl Microbiol. 2011;53(2):186-92.
5. Burt S. Essential oils: their antibacterial properties and potential applications in foods—a review. Int J Food Microbiol. 2004;94(3):223-53.
6. Paulo F, Santos L. Design of experiments for microencapsulation applications: A review. Materials Science and Engineering: C. 2017;77: 1327-40.
7. Teeka P, Chaiyasat A, Chaiyasat P. Preparation of poly (methyl methacrylate) microcapsule with encapsulated jasmine oil. Enrgy Proced. 2014;56: 181-6.
8. Chaiyasat P, Pholsrimuang P, Boontung W, Chaiyasat A. Influence of poly(l-lactic acid) molecular weight on the encapsulation efficiency of urea in microcapsule using a simple solvent evaporation technique. Polym-Plast Technol. 2016;55(11):1131-6.
9. Chaiyasat P, Chaiyasat A, Teeka P, Noppalit S, Srinorachun U. Preparation of poly(l-lactic acid) microencapsulated Vitamin E. Enrgy Proced. 2013;34:656-63.
10. Chaiyasat P, Kamlangmak N, Hangmi K, Rattanawongwiboon T, Chaiyasat A. Fabrication of cellulose-based particles/capsules using gamma radiation-initiated radical precipitation polymerization. Int J Polym Mater Po. 2022;1-11.
11. Pang L, Gao Z, Feng H, Wang S, Wang Q. Cellulose based materials for controlled release formulations of agrochemicals: A review of modifications and applications. Journal of Controlled Release. 2019; 316:105-15.
12. Wang X, Yin H, Chen Z, Xia L. Epoxy resin/ethyl cellulose microcapsules prepared by solvent evaporation for repairing microcracks: Particle properties and slow-release performance. Materials Today Communications. 2020;22:100854.

DOI: 10.60101/jarst.2023.253714

13. Moreno JS, Dima P, Chronakis IS, Mendes AC. Electrosprayed ethyl cellulose core-shell microcapsules for the encapsulation of probiotics. Pharmaceutics. 2022;14(1):7.

14. Ponce Cevallos PA, Buera MP, Elizalde BE. Encapsulation of cinnamon and thyme essential oils components (cinnamaldehyde and thymol) in β-cyclodextrin: Effect of interactions with water on complex stability. J Food Eng. 2010; 99(1):70-5.

15. Amit Kumar P, Shinichi S. Recent Developments in the Crystallization of PLLA-Based Blends, Block Copolymers, and Nanocomposites. In: Youssef Ben S, Riadh M, editors. Crystallization and Applications. Rijeka: IntechOpen; 2021. p. Ch. 5.

16. Jelvehgari M, Montazam SH. Comparison of microencapsulation by emulsion-solvent extraction/ evaporation technique using derivatives cellulose and acrylate-methacrylate copolymer as carriers. Jundishapur J Nat Pharm Prod. 2012;7(4):144-52.

17. Prakash K, Raju P, Shanta K, Lakshmi M. Preparation and characterization of lamivudine microcapsules using various cellulose polymers. Trop J Pharm Res. 2007;6(4):841-7.

18. Junyaprasert VB, Manwiwattanakul G. Release profile comparison and stability of diltiazem–resin microcapsules in sustained release suspensions. International Journal of Pharmaceutics. 2008;352(1):81-91.

19. Beşen BS. Tea tree oil/ethyl cellulose microcapsule loaded antimicrobial textiles. AATCC Journal of Research. 2020;7(2):1-6.

20. Khotchana C, Phapugrangkul P, Opaprakasit P, Kaewpa D, Chaiyasat P, Chaiyasat A. Synthesis of uniform submicron poly(lactic acid)-based particles/ capsules by radical precipitation polymerization. Colloids and Surfaces B: Biointerfaces. 2021;208: 112122.

21. Sangjun P, Chaiyasat A. Poly(l-lactic acid)-based microcapsule containing phase-change material: Influence of polymer shell on particle morphology. Fiber Polym. 2020;21(5):935-43.

22. Kesente M, Kavetsou E, Roussaki M, Blidi S, Loupassaki S, Chanioti S, et al. Encapsulation of olive leaves extracts in biodegradable PLA nanoparticles for use in cosmetic formulation. Bioengineering. 2017;4(3):75-89.

23. Brlek I, Ludaš A, Sutlović A. Synthesis and Spectrophotometric analysis of microcapsules containing immortelle essential oil. Molecules. 2021;26(8):2390-9.

24. Amim J, Kosaka PM, Petri DFS. Characteristics of thin cellulose ester films spin-coated from acetone and ethyl acetate solutions. Cellulose. 2008;15(4):527-35.

25. Liu L, Yang JP, Ju XJ, Xie R, Yang L, Liang B, et al. Microfluidic preparation of monodisperse ethyl cellulose hollow microcapsules with non-toxic solvent. Journal of Colloid and Interface Science. 2009;336(1):100-6.

26. Chung TW, Huang YY, Liu YZ. Effects of the rate of solvent evaporation on the characteristics of drug loaded PLLA and PDLLA microspheres. International Journal of Pharmaceutics. 2001; 212(2):161-9.

27. Liu R, Ma G, Meng FT, Su ZG. Preparation of uniform-sized PLA microcapsules by combining Shirasu porous glass membrane emulsification technique and multiple emulsion-solvent evaporation method. J Control Release. 2005; 103(1):31-43.

DOI: 10.60101/jarst.2023.253714

Received: August 26, 2023 | Revised: October 3, 2023 | Accepted: October 4, 2023

JOURNAL OF APPLIED RESEARCH ON SCIENCE AND TECHNOLOGY
JARST
INSTITUTE OF RESEARCH AND DEVELOPMENT
RAJAMANGALA UNIVERSITY OF TECHNOLOGY THANYABURI
ISSN ONLINE: 2773-9473
https://ph01.tci-thaijo.org/index.php/rmutt-journal

Development of a photoelectrocatalytic method to improve the efficiency of *E. coli* removal

Kanyarat Hmud[1], Masashi Hatamoto[2], Somporn Moonmangmee[3] and Chatchai Ponchio[1, 4*]

[1]Department of Chemistry, Faculty of Science and Technology, Rajamangala University of Technology Thanyaburi, Pathum Thani 12120, THAILAND
[2]Department of Environmental Systems Engineering, Nagaoka University of Technology, Niigata 940-2188, JAPAN
[3]Biodiversity Research Center, Thailand Institute of Scientific and Technological Research, Pathum Thani 12120, THAILAND
[4]Advanced Photochemical and Electrochemical Materials Research Unit (APEM) Research Unit, Faculty of Science and Technology, Rajamangala University of Technology Thanyaburi, Pathum Thani 12110, THAILAND
[*]Corresponding author: chatchai@rmutt.ac.th

ABSTRACT

The photoelectrocatalytic technology has attracted significant attention for effectively eliminating organic matter and microbiological pollutants in the environment, owing to its remarkable efficiency and low power consumption. The major goal of this research is to develop and determine the optimal conditions that will facilitate the photoelectrocatalytic technique's enhancement of *E. coli* eradication. The $WO_3/BiVO_4$ photoanode was fabricated on a conductive glass substrate using the automatic dip coating process, employing a layer-by-layer deposition method. Subsequently, the $WO_3/BiVO_4$ photoanode was calcinated at 550 °C for 60 minutes. The produced $WO_3/BiVO_4$ electrodes were employed as working electrodes to investigate and determine the optimal parameters for enhancing the eradication of *E. coli* process. The primary factors investigated in this study were the concentration of KCl electrolyte solution and the applied potential. These parameters were examined to identify the best circumstances that would result in the highest efficiency for the degradation of *E. coli* in a photoelectrochemical system. The study also aimed to comprehend the catalytic mechanism implicated in eliminating *E. coli* by implementing three different processes: photocatalysis, electrocatalysis, and photoelectrocatalysis. We discovered that the key factors directly influencing *E. coli* eradication effectiveness under the photoelectrocatalytic process were applied potential and electrolyte solution concentration. The optimum conditions eliminated 99.99% of *E. coli* in 150 minutes with an initial concentration of 10^6 CFU/ml, an electrolyte concentration of 0.01 M KCl, and an applied potential of 2.0 V. The study confirmed photoelectrocatalytic cells' efficacy in removing microorganisms and recommended their application in a wider range of wastewater treatment systems.

Keywords: Photoelectrocatalytic cell, *E. coli* removal, $WO_3/BiVO_4$ photoanode

INTRODUCTION

Contaminated wastewater has serious consequences for human and animal health due to the presence of bacteria and microbes [1, 2]. *Escherichia coli* (*E. coli*) is one of the most prevalent antibiotic-resistant pathogens. Therefore, it is necessary to develop effluent treatment methods [3-5]. Photoelectrocatalytic (PEC) technique, an advanced electrochemical technique that catalyzes the reaction with light and applied potential, has attracted great interest in applications for microbial elimination [4, 6-9]. The development of PEC technique can be achieved by finding optimum conditions for the highest efficiency in removing target substances or improving the reaction process [10, 11]. This research aims to study factors affecting the efficiency of eliminating *E. coli* using PEC techniques. We have investigated the factors that affect the efficacy of *E. coli* degradation, including electrolyte solution concentration, electric potential, and the catalytic mechanism at the electrode surface. We investigated and determined the optimal conditions for PEC cells to maximize the efficacy of *E. coli* elimination and confirm the mechanism responsible for the acceleration of elimination at the electrode surface. This research holds significant potential and carries implications for the advancement of novel technologies aimed at eradicating microorganisms in water and for further enhancing water treatment systems.

MATERIALS AND METHODS

FTO/WO_3/$BiVO_4$ electrode preparation

This study prepares the electrodes with an automatic dip coating machine, as displayed in figure 1. Fluorine-doped tin oxide (FTO) conductive glass was used as a support material for the fabrication of

DOI: 10.60101/jarst.2023.253893

JOURNAL OF APPLIED RESEARCH ON SCIENCE AND TECHNOLOGY

semiconductor thin films by ultrasonic cleaning in various solutions for 10 minutes, as detailed as follows: solution of detergent, 3 M sodium hydroxide solution, ethanol solution, and deionized water. The FTO conductive glass was immersed in a 0.1 M WO_3 solution, dried at 150 °C for five minutes, and then calcined at 500 °C for thirty minutes. Then, using an automatic dip coater, the FTO/WO_3 electrode was immersed in 0.05 M $BiVO_4$ solution. Then, they are dried at 150 °C for 5 minutes and calcined at 550 °C for 60 minutes. In the experimental setup, FTO/WO_3/$BiVO_4$ electrodes are employed as an anode electrode to further examine the effectiveness of *E. coli* eradication.

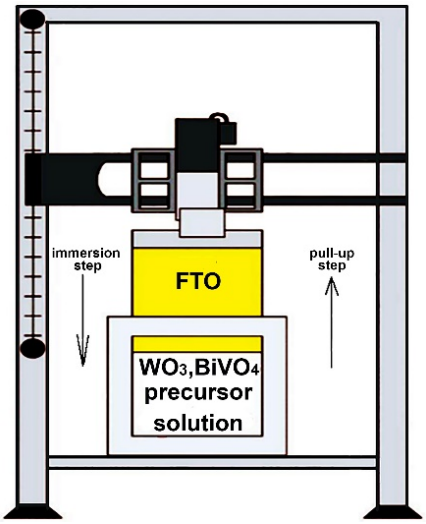

Figure 1 The schematic dip coating machine for FTO/WO_3/$BiVO_4$ electrode fabrication process.

E. coli removal efficiency study

The FTO/WO_3/$BiVO_4$ electrode was employed to investigate the effectiveness of eradicating *E. coli* by utilizing the PEC approach. The concentrations of KCl electrolyte solutions at 0, 0.01, 0.025, 0.05, 0.075, and 0.1 M and applied potentials of 0, 0.5, 1.0, 1.5, 2.0, and 2.5 V were studied to determine the optimal conditions for the highest PEC *E. coli* degradation efficiency. In addition, the catalytic mechanism for the eradication of *E. coli* was investigated using Photocatalytic (PC), Electrocatalytic (EC), Photoelectrocatalytic (PEC), and control containing approximately 10^6 CFU/ml of *E. coli*. The concentration of *E. coli* was examined utilizing the spread plate technique at different time intervals. Subsequently, the concentration and percentage degradation were determined and represented by Equation (1) [12] and Equation (2), respectively.

$$\text{CFU/ml} = \frac{\text{Total number of colonies obtain x dilution factor}}{\text{Volume of specimen used}} \quad (1)$$

$$\textit{E. coli}\ \text{degradation}\ (\%) = \frac{A_0 - A_t \times 100}{A_0} \quad (2)$$

where A_0 represents the quantity of *E. coli* present at the beginning of the elimination process in CFU/ml. A_t represents the quantity of remaining *E. coli* at the time in CFU/ml.

RESULTS AND DISCUSSIONS

Optimization of PEC cell for E. coli degradation

The experimental results demonstrated a direct relationship between an increase in applied voltage within the range of 0 to 2.5 V and the subsequent enhancement in the efficiency of *E. coli* removal, as demonstrated in figure 2.

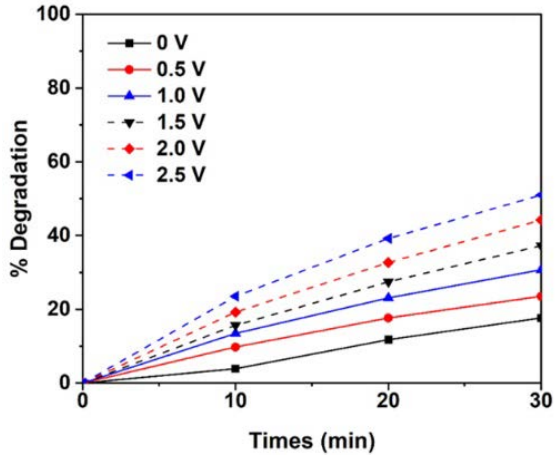

Figure 2 The effect of applied potential on *E. coli* degradation efficiency.

This phenomenon occurs due to the acceleration of charge transfer and the subsequent increase in electron flow from the anode to the cathode when the applied voltage is raised in the positive direction. Increasing the positive potential also increases the amount of positively charged (hole; h^+) at the anode, which supports a high oxidizing efficiency for the degradation of *E. coli* [13]. However, the electrode life may be compromised if the system voltage is too high.

Figure 3 illustrates the effect of varying concentrations of potassium chloride (KCl) electrolyte solution on eradicating *E. coli*. The efficacy of eradicating *E. coli* is directly proportional to the concentration of electrolytes within the range of 0 to 0.1 M. The results that were noticed through the investigation of KCl concentration. Increasing electrolyte concentration facilitates enhanced electrical conductivity and charge transfer between the electrodes, hence promoting electrode surface reactions that contribute to more effective degradation of *E. coli* [14]. Increasing the concentration of KCl can also result in the dissociation of chloride ions in the solution. The chloride ion present in the electrolyte undergoes a constant reaction with the hydroxyl radical, resulting in the formation of chlorine compounds that exhibit exceptional efficacy in eradicating *E. coli*.

DOI: 10.60101/jarst.2023.253893

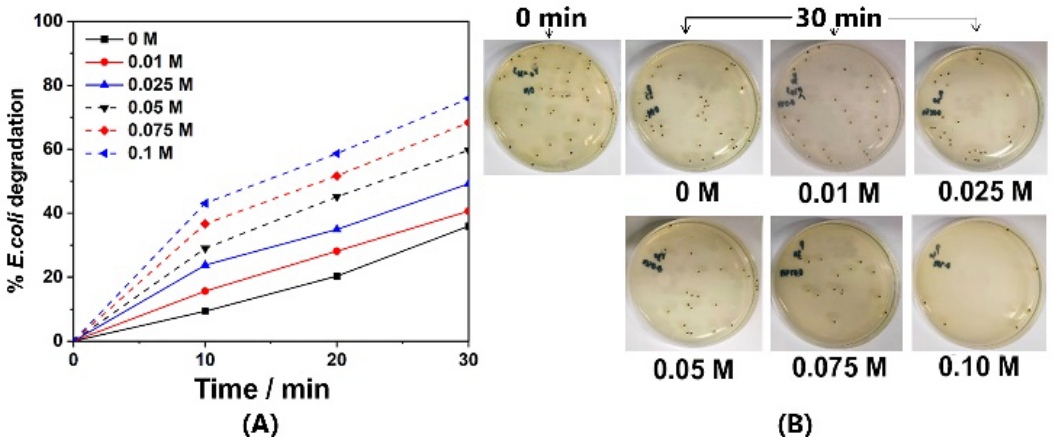

Figure 3 The effect of KCl electrolyte concentration on the efficacy of *E. coli* degradation, where (A) the percentage of *E. coli* degradation and (B) the photo of *E. coli* depending on KCl concentration and time degradation.

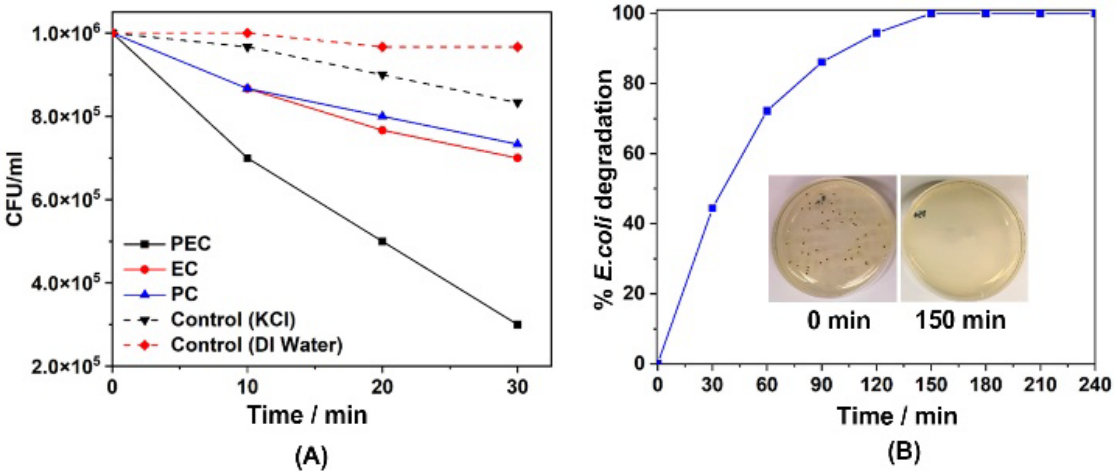

Figure 4 The catalytic mechanism in *E. coli* degradation was investigated; (A) reduction of *E. coli* in CFU/ml and (B) *E. coli* degradation efficiency under optimal conditions and inset of photographs of *E. coli* analysis.

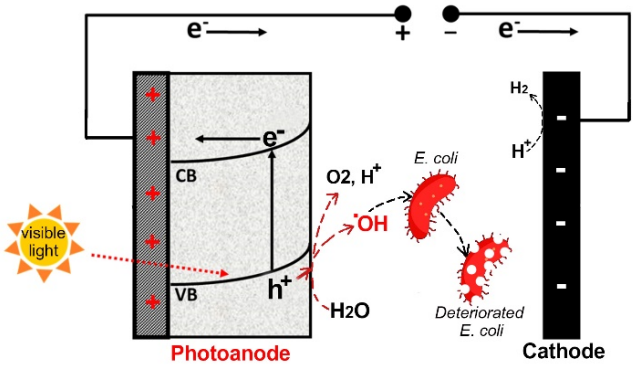

Figure 5 Diagrammatic representation of the process at the semiconductor anode surface for PEC-based removal of *E. coli*.

Catalytic mechanism and E. coli degradation efficiency

Figure 4 demonstrates that the PEC catalytic mechanism has the highest *E. coli* degradation efficiency of 70% within 60 minutes, followed by the EC, PC catalytic mechanism, and solution-based potassium chloride control system, which eliminated only 20%, 26%, and 17%, respectively. In contrast, controls that do not utilise potassium chloride electrolyte solution can only remove a small amount. In addition, figure 4B demonstrated that *E. coli* at a concentration of 10^6 CFU/ml could be eliminated 100% in 150 minutes using a potassium chloride electrolyte concentration of 0.01 M and an applied potential of 2 V with the PEC technique.

Figure 5 exhibits the schematic diagram illustrating the reaction occurring at the surface of the semiconductor anode, specifically in the presence of photo-acceleration and electric potential. When the valence band (VB) layer of a semiconductor is stimulated by light within a certain range, it leads to the dissociation of electrons (e^-) from the VB to the conduction band (CB) [9, 15], while simultaneously creating a positively charged vacancy (hole; h^+) inside the VB. The VB layer has a notable propensity to facilitate water oxidation at the surface of the semiconductor electrode $WO_3/BiVO_4$, generating hydroxyl radicals (^oOH). This generated ^oOH has powerful oxidizing capabilities, efficiently oxidizing *E. coli* in aqueous solution [16]. In addition, controlling the positive potential at the anode electrode

DOI: 10.60101/jarst.2023.253893

may accelerate transport and induce e^- flow at the CB layer from the anode electrode to the cathode electrode to convert H^+ to H_2 [17]. This procedure can potentially mitigate the recombination occurrence of electron-hole pairs (e^- and h^+) and enhance the PEC characteristics for eliminating *E. coli*.

CONCLUSION

This research successfully applied a $WO_3/BiVO_4$ photoanode to eliminate *E. coli* under a photoelectrocatalytic process effectively. The electrolyte concentration and potential applied factors in the *E. coli* elimination system were investigated. We demonstrated that when the proposed PEC approach was optimized with a 0.01 M potassium chloride electrolyte solution and an applied voltage of 2 V, *E. coli* at 10^6 CFU/mL was 100% eliminated in 150 minutes. This study generates information for developing a new alternative technique for treating wastewater contaminated with microorganisms and other organic waste.

ACKNOWLEDGEMENT

This research was supported by Reinventing University Project (RMUTT) 2022, Office of the Ministry of Higher Education, Science, Research and Innovation, Thailand Science Research and Innovation. Moreover, the research was also supported by The Science, Research and Innovation Promotion Funding (TSRI) (Grant no. FRB650070/0168). This research block grants was managed under Rajamangala University of Technology Thanyaburi (FRB65E0605C.2).

REFERENCES

1. Oliveira R, Silva RM, Castro AR, Rodrigues LR, Pereira MA. 10 - Biological processes and the use of microorganisms in oily wastewater treatment. In: Basile A, Cassano A, Rahimpour MR, Makarem MA, editors. Advanced Technologies in Wastewater Treatment: Elsevier; 2023. p. 257-88.
2. Techaoei S. Bacterial and fungal contamination of personal care product in Northern Thailand. J Appl Res Sci Tech. 2017;16(1-2):32-8.
3. Maniakova G, Polo-López MI, Oller I, Abeledo-Lameiro MJ, Malato S, Rizzo L. Simultaneous disinfection and microcontaminants elimination of urban wastewater secondary effluent by solar advanced oxidation sequential treatment at pilot scale. J Hazard Mater. 2022;436:129134.
4. Srevarit W, Moonmangmee S, Phapugrangkul P, Kuboon S, Klamchuen A, Saito N, et al. Photoelectrocatalytic H_2 evolution enhancement over CuO-decorated TiO_2 nanocatalysts and promoting *E. coli* degradation. J Alloy Compd. 2021;859:157818.
5. Seekhaw P, Chuaboonmee R, Surayot P, Chadpan S, Thurnkul N. Evaluation of phytochemical screening, antioxidant and antimicrobial activities from ethanolic extracts of the *Flacourtia indica* (Burm.f.) Merr. fruits. J Appl Res Sci Tech. 2020;19 (1):124-36.
6. Rather RA, Lo IMC. Photoelectrochemical sewage treatment by a multifunctional g-C_3N_4/Ag/AgCl/$BiVO_4$ photoanode for the simultaneous degradation of emerging pollutants and hydrogen production, and the disinfection of *E. coli*. Water Res. 2020; 168:115166.
7. Dang Q, Wang L, Liu J, Wang D, Chai J, Wu M, et al. Recent progress of photoelectrocatalysis systems for wastewater treatment. Journal of Water Process Engineering. 2023;53:103609.
8. Chen W, Liu S, Fu Y, Yan H, Qin L, Lai C, et al. Recent advances in photoelectrocatalysis for environmental applications: Sensing, pollutants removal and microbial inactivation. Coordin Chem Rev. 2022;454:214341.
9. Liu J, Ma N, Wu W, He Q. Recent progress on photocatalytic heterostructures with full solar spectral responses. Chemical Engineering Journal. 2020;393:124719.
10. Nareejun W, Ponchio C. Novel photoelectrocatalytic/solar cell improvement for organic dye degradation based on simple dip coating $WO_3/BiVO_4$ photoanode electrode. Sol Energ Mat Sol. 2020;212:110556.
11. Arunima SR, Deepa MJ, Nair AJ, Shibli SMA. Exploration of $WO_3/BiVO_4$ composite based hot-dip zinc coating to combat biocorrosion. Materials Science and Engineering: B. 2021;271:115302.
12. Reynolds J. Serial dilution protocols. American Society for Microbiology: Washington, DC, USA. 2005:1-7.
13. Qi Z, Li G, Wang M, Chen C, Xu Z, An T. Photoelectrocatalytic inactivation mechanism of *E. coli* DH5α (TET) and synergistic degradation of corresponding antibiotics in water. Water Res. 2022;215:118240.
14. He H, Sun S, Gao J, Huang B, Zhao T, Deng H, et al. Photoelectrocatalytic simultaneous removal of 17α-ethinylestradiol and *E. coli* using the anode of Ag and SnO_2-Sb 3D-loaded TiO_2 nanotube arrays. Journal of Hazardous Materials. 2020;398:122805.
15. Li G, Yang C, He Q, Liu J. Ag-based photocatalytic heterostructures: Construction and photocatalytic energy conversion application. Journal of

DOI: 10.60101/jarst.2023.253893

Environmental Chemical Engineering. 2022;10(3): 107374.

16. McMichael S, Tolosana-Moranchel A, Cortes MALRM, Hamilton JWJ, Fernandez-Ibanez P, Byrne JA. An investigation of photoelectrocatalytic disinfection of water using titania nanotube photoanodes with carbon cathodes and determination of the radicals produced. Applied Catalysis B: Environmental. 2022;311:121339.
17. Thongthep P, Moonmangmee S, Ponchio C. Solar/photoelectrocatalytic cell development for H_2 production and simultaneous organic dye degradation. Mat Sci Semicon Proc. 2021;124: 105597.

DOI: 10.60101/jarst.2023.253893

Received: September 12, 2023 | Revised: November 2, 2023 | Accepted: November 2, 2023

JOURNAL OF APPLIED RESEARCH ON SCIENCE AND TECHNOLOGY
JARST
INSTITUTE OF RESEARCH AND DEVELOPMENT
RAJAMANGALA UNIVERSITY OF TECHNOLOGY THANYABURI
ISSN ONLINE: 2773-9473
https://ph01.tci-thaijo.org/index.php/rmutt-journal

Cellulose rubber foam composite use as oil absorbent

Poptorn Klaykhem[1], Pruttipong Pantamanatsopa[1,2] and Warunee Ariyawiriyanan[1,3*]

[1]Department of Materials and Metallurgical Engineering, Faculty of Engineering, Rajamangala University of Technology Thanyaburi, Pathum Thani 12110, THAILAND

[2]Department of Industrial Engineering, Faculty of Engineering, Rajamangala University of Technology Srivijaya, Songkhla 90000, THAILAND

[3]Systems Research and Innovation Development Research Unit, Rajamangala University of Technology Thanyaburi, Pathum Thani 12110, THAILAND

[*]Corresponding author: warunee.a@en.rmutt.ac.th

ABSTRACT

The focus of this study was to explore the fabrication of cellulose rubber foam (CRF) using kapok fibers (KF) as an oil absorbent material. Chemical methods such as sodium hydroxide surface treatment, hydrogen peroxide treatment, and acid hydrolysis were employed to prepare cellulose nanocrystals (CNC). The results of the nuclear magnetic resonance (NMR) spectroscopy test indicated that the chemical modification of kapok fiber resulted in the removal of lignin and hemicellulose by a disappearing peak at 17, 52, and 148 ppm, respectively. Hydrolysis process of the kapok fiber resulted in nanometer-sized cellulose, with a yield of 72% as revealed by transmission electron microscopy (TEM). The amount of cellulose nanocrystals from kapok fiber (KF-CNC) used in the study varied from 0 to 5 phr during the formation of the cellulose rubber foam, and it was found that the foam density increased as the number of cellulose nanocrystals from kapok fiber increased. Additionally, the percentage of collapse from the compressive strength of cellulose rubber foam decreased as the amount of cellulose nanocrystals from kapok fiber increased. Fourier transform infrared spectroscopy (FTIR) confirmed the incorporation of cellulose nanocrystals from kapok fiber into the rubber foam (RF) as the amount of cellulose nanocrystals from kapok fiber increased. The oil absorbent of cellulose rubber foam composite with 1 phr cellulose nanocrystals from kapok fiber show highest absorption capacity was 17.8 g/g. The cellulose rubber foam composite absorbs oil before absorbing water when water and oil are combined. Moreover, the cellulose rubber foam could be reused more than 50 times.

Keywords: Kapok fiber, Rubber foam, Cellulose nanocrystals, Cellulose rubber foam, Oil absorbent

INTRODUCTION

Nowadays, the problem of natural oil contamination is still a big problem everywhere in the world and humans are involved due to the use of oil in everyday life. The leakage or contamination of oil may affect nature. The water source is the habitat of various living things, including human water resources. Many materials are used to eliminate the problem of oil contamination in water supplies. Most commercial adsorbents used in oil removal are plastic-based materials with a lot of porosity. Commercial materials may increase plastic waste that is difficult to biodegrade. Absorbent materials made from natural materials can help reduce the problem of plastic waste even more. The material that can be developed as an absorbent material is natural rubber. Thailand is the world's number one natural rubber producer but most of them are exported in the form of raw latex. Therefore, the processing of natural rubber into products may increase the benefits of using more widely available rubber. Rubber foam is a porous, lightweight material that can be used in a wide range of applications such as absorbents, cushioning materials and sound-absorbing materials, etc. [1, 2].

Composite material made from natural fibers has received widespread attention both in plastic molding industry instead of using synthetic fibers. The advantages of natural fibers are that they are cheap and easily found naturally with low toxicity. There are many natural fibers that are plentiful in Thailand such as water hyacinth, bamboo, rice husk, bagasse, etc. [3]. And there is another type that is abundant in Thailand but is still rarely used is kapok fiber. Kapok in the form of stuffed pillows, because it is light and soft, is one of the high cellulose fibers. Kapok fibers have interesting properties for example natural skin coatings. This will prevent water so that the cotton fibers do not get wet but have oil-absorbing

DOI: 10.60101/jarst.2023.254006

properties which can be applied to many aspects of work such as the environment including various oil stains occurring in daily life, etc. Therefore, it is interesting to bring local resources and develop them into oil-absorbing cellulose rubber foam. Therefore, in this research, we are interested in using natural fibers, kapok fibers which are relatively high cellulose fibers as an oil-absorbing material. In the previous work, the oil absorbency is supplemented by the addition of kapok fibers in larger quantities, resulting in a significant increase in oil absorbency [4]. However, using natural fibers may have a detrimental effect on the properties of the material. Kapok fibers must therefore be cleaned by bleaching them with hydrogen peroxide and sodium hydroxide to remove impurities or unwanted substances such as hemicellulose, lignin, and other impurities. Cellulose is hydrolyzed with acid in sulfuric acid [5] and then mixed with natural rubber foam and cellulose nanocrystals from kapok fibers with different cellulose nanocrystal contents.

MATERIALS AND METHODS

Materials

Kapok fiber (KF), HANR 60% DRC (NORRAWAT CHEMICAL Part., Ltd.), Chemicals used include sodium hydroxide (NaOH), hydrogen peroxide (H_2O_2), sulfuric acid 98% (H_2SO_4), potassium hydroxide (KOH), zinc diethyl-dithiocarbamate dispersion (ZDEC), zinc mercaptobenzo-thiazole dispersion, (ZMBT), Wingstay L, Potassium Oleate, Diphenyl guanidine (DPG), Sodium silicofluoride (SFF), Zinc oxide (ZnO)

KF pretreatment process

The KF was boiled in a 2M NaOH solution at 90 °C for 60 minutes and filtered by a sieve (involved in alkalization at mm openings) and washed with deionized (DI) water to remove NaOH. Then, the kapok alkaline fiber was subsequently bleached using 0.05 M aqueous NaOH buffer and 10% v/v aqueous H_2O_2 at 90 °C for 120 minutes with constant mechanical stirring. The bleached KF was then sieved and thoroughly washed with DI water. To further remove the impurities, the second bleaching was carried out under the same conditions and oven-dried at 60 °C for 24 hours. The bleached kapok is labeled KF-B. The alkalization and bleaching were undertaken to remove impurities before proceeding with the hydrolysis.

Isolation of KF-CNC

CNC was prepared by sulfuric acid hydrolysis [6]. The KF-B was subsequently hydrolyzed by using a diluted H_2SO_4 solution (50% v/v) at 600 rpm, 50 °C for 40 minutes. The hydrolysis was stopped by adding 200 mL of water. The resulting suspension was centrifuged five times at 9,000 rpm, 25°C for 10 minutes to obtain more concentrated cellulose nanocrystal water and centrifuged at 10°C for 50 minutes until KF-CNC deposits were obtained.

Preparation of Rubber Foam (RF) and Cellulose Rubber Foam (CRF)

The preparation of RF and CRF is shown in Table 1. The concentrated natural latex (60% DRC) was stirred for 1 minute to remove ammonia and mixing process for CRF compound preparation is shown in Table 2. Then, pour the latex into the mold and leave the RF set for 10 minutes. The prepared RF was baked at 100 °C for 2 hours, then wash with hot water at 70 °C for 50 minutes and bake again at 80 °C until dry shown in figure 1.

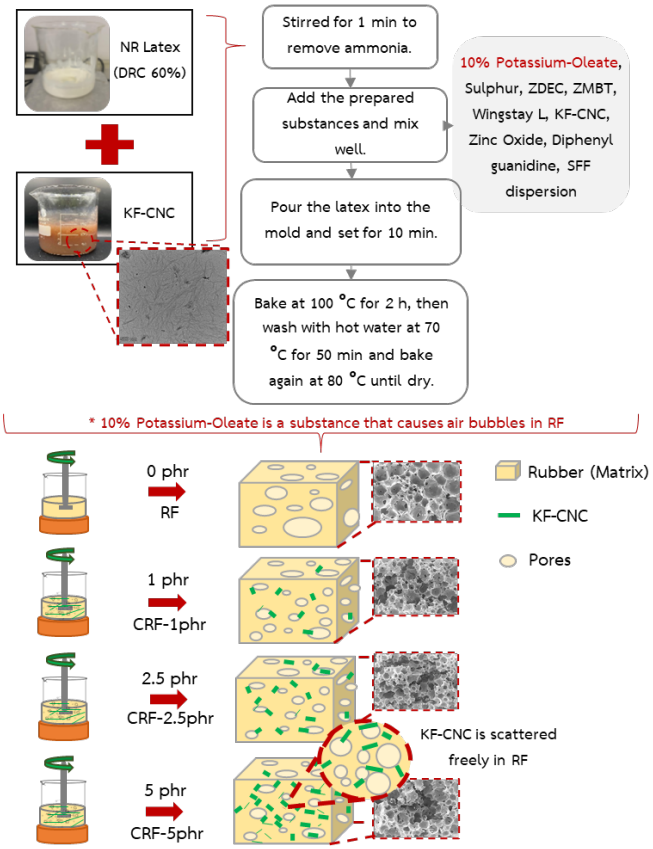

Figure 1 Images of preparation of RF and CRF.

Table 1 Formulations of RF and CRF.

Chemical substances	Weight (phr)
NR latex 60% DRC	100
Potassium-Oleate solution 10%	1.0
Sulphur dispersion 50%	2.5
ZDEC dispersion 50%	1.0
ZMBT dispersion 50%	1.0
Wingstay L dispersion 50%	1.0
ZnO dispersion 50%	5.0
Diphenyl guanidine dispersion 33%	1.0
Sodium silicofluoride dispersion 12.5%	0.5
KF-CNC	0, 1, 2.5, 5

DOI: 10.60101/jarst.2023.254006

JOURNAL OF APPLIED RESEARCH ON SCIENCE AND TECHNOLOGY

Table 2 Mixing procedure for CRF compound preparation.

Order	Ingredient	Mixing time (Minutes)
1	Latex (DRC 60%)	1
2	10% Potassium-Oleate, Sulphur, ZDEC, ZMBT, Wingstay L, KF-CNC	3
3	Zinc Oxide, Diphenyl guanidine	1
4	SFF dispersion	1

Yield of KF-CNC

The yield of KF-CNC of the dry weight ratio between KF-CNC and KF-B [7] (Equation 1), where W_{KF-CNC} was the dry weight of KF-CNC and W_{KF-B} was the dry weight of KF-B. The yield value was obtained from an average of three replications.

$$\text{Yield of KF-CNC (\%)} = \frac{W_{KF-CNC}}{W_{KF-B}} \times 10 \quad (1)$$

Chemical composition of KF-CNC, RF and CRF

The chemical composition was analyzed by Fourier transform infrared spectroscopy (FTIR; Frontier, Perkin Elmer) and nuclear magnetic resonance (NMR) spectroscopy (JEOL; JNM-ECZR 500MHz). Prior to the FTIR and NMR analyses, samples of KF-CNC, RF and CRF were oven-dried at 60 °C for 2 hours. for produce dried film. The dried samples were then scanned using the FTIR spectrometer in attenuated total reflectance mode at 4000 and 600 cm^{-1} and the NMR spectrometer in ^{13}C solid state with a chemical shift between 0-200 ppm.

Morphology of KF, KF-B, KF-CNC, RF and CRF

The morphology of KF, KF-B, RF and CRF was characterized by a scanning electron microscope (SEM) (JEOL; JSM-5410 LV). SEM was utilized to determine the dimensions and physical appearance of raw KF, KF-B, RF and CRF. Prior to SEM analysis the raw KF, KF-B, RF and CRF were stuck to the stub with carbon tape and then coated with gold. The morphology of KF-CNC was characterized by a transmission electron microscope, TEM (TEM; Thermo Scientific, TALOS F200X). TEM was utilized to determine the dimensions (i.e., diameter and length) and the physical appearance of KF-CNC. Specimen preparation prior to analysis was done by dropping KF-CNC solution on the surface of carbon grid and leaving it to dry at room temperature.

Compression testing of RF and CRF

The compression testing was conducted according to ASTM D 395 standard [8]. Prior to test cutting a circular specimen with a diameter of 29 mm, height of 19 mm, placing the specimen in a compressed steel plate, pressing to deflate 50% from its original height and holding for about 15 minutes and bake at 70 °C for 22 hours, remove from the oven. Place the specimen for 30 minutes, then measure the height of the specimen. The calculation formula is as shown in (Equation 2).

$$\text{Compression set \%} = \left(\frac{t_0 - t}{t_0}\right) \times 100 \quad (2)$$

Where t_0 = thickness after test (mm) and t = original thickness (mm)

Density of RF and CRF

The density analysis was performed according to the ASTM D 3574-95 standard [9]. Prior to test cutting a rectangular piece of CRF. Weight and calculate the density of the sample using the formula as in (Equation 3).

$$D = \frac{M}{V} \quad (3)$$

Where D= density of specimen (g/cm^3), M= specimen weight (g) and V= specimen volume (cm^3)

Ability to oil absorbent of RF and CRF

The ability to absorb oil for RF and CRF analysis is determined by cutting the test specimen to a size of 2.5x2.5x2.5 cm then dropping the sample into the beaker with the oil at varying time with 15, 30, 60, 120, 180 and 1440 minutes, respectively. Then, take the sample out of the oil beaker. Clean the oil on the surface of the CRF. Then weigh and calculate the adsorption capacity (oil sorption capacity) in (Equation 4) [10].

$$\text{Oil sorption capacity (g/g)} = \frac{Ms - Mi}{Mi} \quad (4)$$

Where M_s = weight after adsorption (weight of RF and CRF and oil in grams) and M_i = weight before adsorption (RF and CRF weight in grams).

RESULTS AND DISCUSSION

KF preparation results

Figure 2a and 2b are the photographs of KF and KF-B. In figure 2a, the color of RF is light brown. Figure 2b shows the KF-B, the color of KF-B is white. The change in color was confirmed by the removal of wax, lignin, hemicellulose and other impurities following the chemical treatment (alkalinization and bleaching).

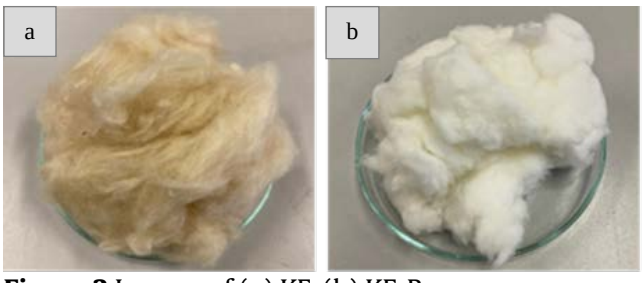

Figure 2 Images of (a) KF, (b) KF-B.

DOI: 10.60101/jarst.2023.254006

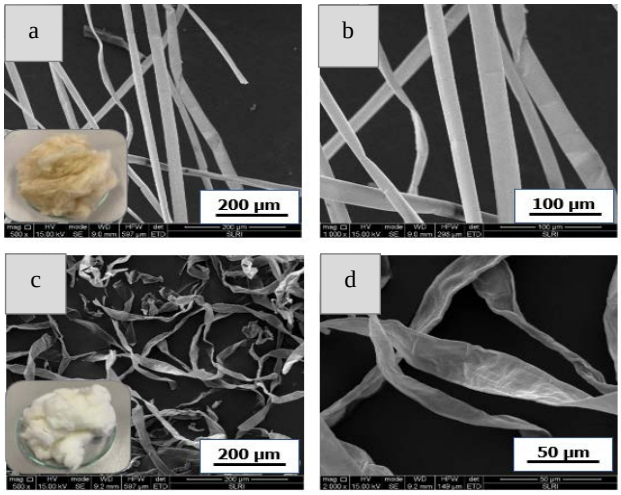

Figure 3 The morphological test results of (a,b) KF, (c,d) KF-B were observed using a scanning electron microscopy (SEM).

Morphology results of KF and KF-B

Figure 3a-3d show the microstructure of KF and KF-B by using SEM. In Figure 3a and 3b, the KF was bundled together and the fibers are thick. Following the alkalization and KF-B. In Figure 3c-3d bleaching future thinned out the fibers, resulting in the microfibers (KF-B). The smoother and thinner fibers were effective in removing non-cellulosic components and other impurities (i.e., pectin and wax) which serve as the protective layer of KF.

The yield of KF-CNC

After acid hydrolysis process. The resulting of yield of KF-CNC was 72%, the aqueous suspension of KF-CNC was stable after hold on after 96 hours. Furthermore, the flow birefringence was carried out under a cross-polarized light setup, that specified the particle of cellulose in the KF-CNC aqueous suspension. Table 3 show the aqueous suspension, given hydrolysis condition, under normal light and under cross-polarized light.

Table 3 Hydrolysis and KF-CNC synthesis.

KF-CNC (Deep yellow, translucent solution Yield = 72%)		
normal light	**polarized light**	**CNC gel**
		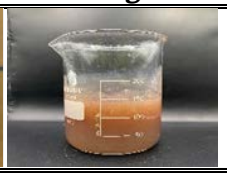

TEM Morphology KF-CNC

Figure 4a and 4b show the TEM image of KF-CNC under acid hydrolysis condition. The KF-CNC was of whisker shape as the acid remove the amorphous region of KF-B while retaining the straight crystalline regions. The length and diameter of KF-CNC show in nano scale. The reduce size of KF-CNC effective from amorphous domain was remove after acid hydrolysis.

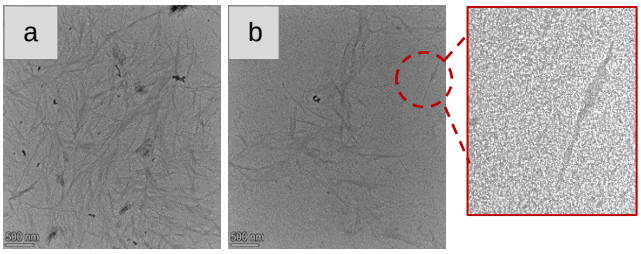

Figure 4 Morphology of KF-CNC (a,b) observed using a transmission electron microscope (TEM).

NMR chemical composition

Figure 5a-5c present the NMR curves of KF, KF-B, and KF-CNC, respectively. The peak at 17, 52, and 148 were hemicellulose and lignin. However, all peaks with lignin and hemicellulose disappeared after alkalization and bleaching, which meansthe alkalization and bleaching effectively removed hemicellulose and lignin.

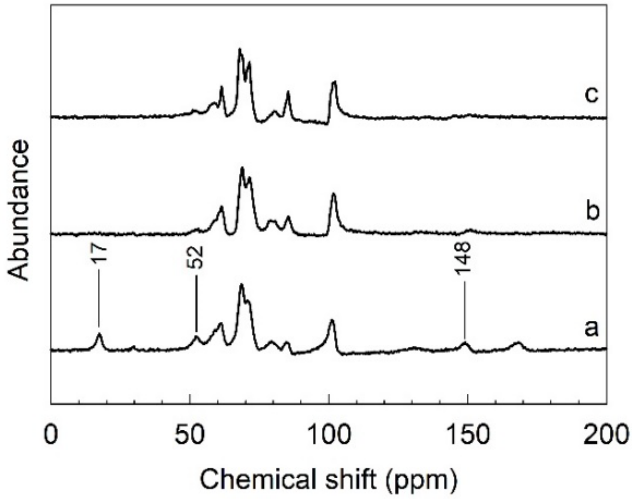

Figure 5 NMR spectrum of (a) KF, (b) KF-B, (c) KF-CNC.

FTIR chemical composition

Peaks for RF found in the FTIR microscopy results are 1209, 1270, and 1502 cm^{-1} (Figure 6). On the other hand, it was observed that the apparent peak gradually faded as more KF-CNC was added to create CRF. It may be possible that a peak point significantly disappeared as a result of KF-CNC filling into RF.

Morphology of RF and CRF

CRF was produced by using a natural rubber latex composite with varying KF-CNC (0 phr, 2.5 phr, and 5 phr). Figure 7a-7d shows the cell structures of RF and CRF. Figure 7a shows the cell structure of RF as a big hole and a close cell. Besides, after adding KF-CNC as shown in Figure 7B-7C.

DOI: 10.60101/jarst.2023.254006

JOURNAL OF APPLIED RESEARCH ON SCIENCE AND TECHNOLOGY

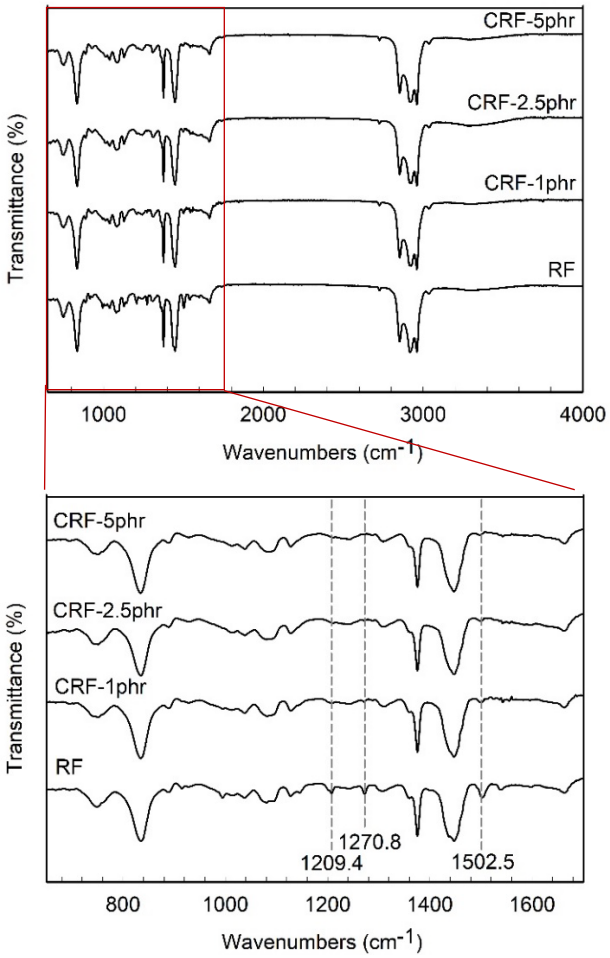

Figure 6 FTIR spectrum of RF and CRF.

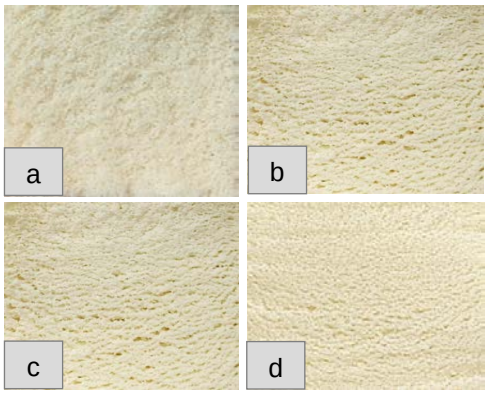

Figure 7 Cell structure of RF and CRF (a) RF, (b) CRF-1phr, (c) CRF-2.5phr, (d) CRF-5phr.

Figure 8a-8d shows the properties of RF and CRF at 0, 1, 2.5, and 5 phr respectively. Figure 8a show average hole size of RF is 400 µm, which bigger than KF-CNC (Figure 8b-8Dd) were show average hole size is 200 µm. the cell structure of RF and CRF is open cell. That has good properties for oil absorption.

Compression test result of RF and CRF

The percentage of CRF compression decreased. When the concentration of KF-CNC was increased (Figure 9). Compression % it shows that 1 phr is better than 2.5 and 5 phr because 1 phr is soft, but 2.5phr and 5phr are hard, which may result in poor oil retention performance. However, the results are not significantly different since the size of cellulose at the nanoscale appears tiny. It is possible that the smaller cellulose will not affect the bubble cells in the RF as much as the larger cellulose will.

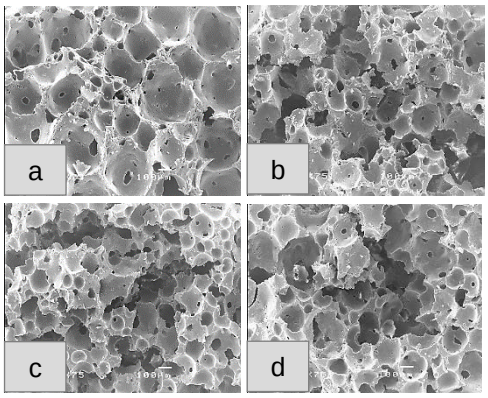

Figure 8 SEM micrographs 75x of RF and CRF composites (a) RF, (b) CRF-1phr, (c) CRF-2.5phr, (d) CRF-5phr.

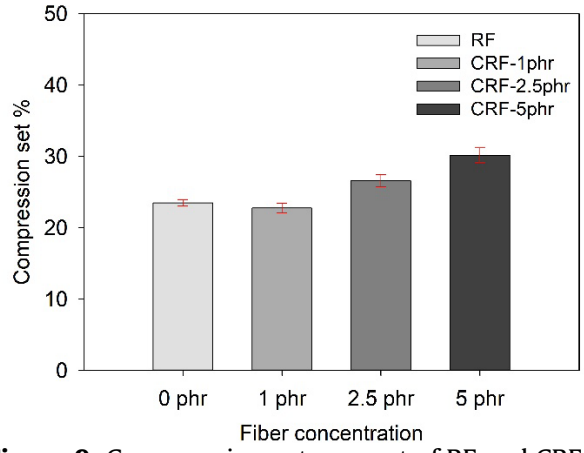

Figure 9 Compression set percent of RF and CRF.

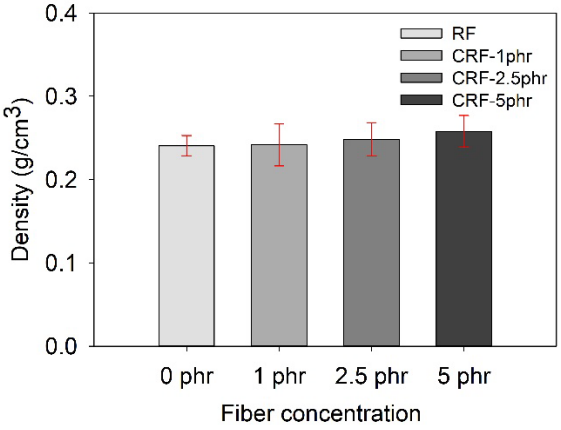

Figure 10 Density of RF and CRF.

Density test results of RF and CRF

Figure 10 shows the density comparison between RF and CRF. The density of RF (excluding

DOI: 10.60101/jarst.2023.254006

KF-CNC) is notably lower due to its larger pore sizes. On the other hand, the density of CRF exhibits a direct correlation with the volume of KF-CNC incorporated. As the quantity of KF-CNC is augmented, it contributes to the overall weight of the CRF, consequently leading to an increase in its density. This phenomenon is attributed to the introduction of KF-CNC, which possesses a denser composition compared to CRF.

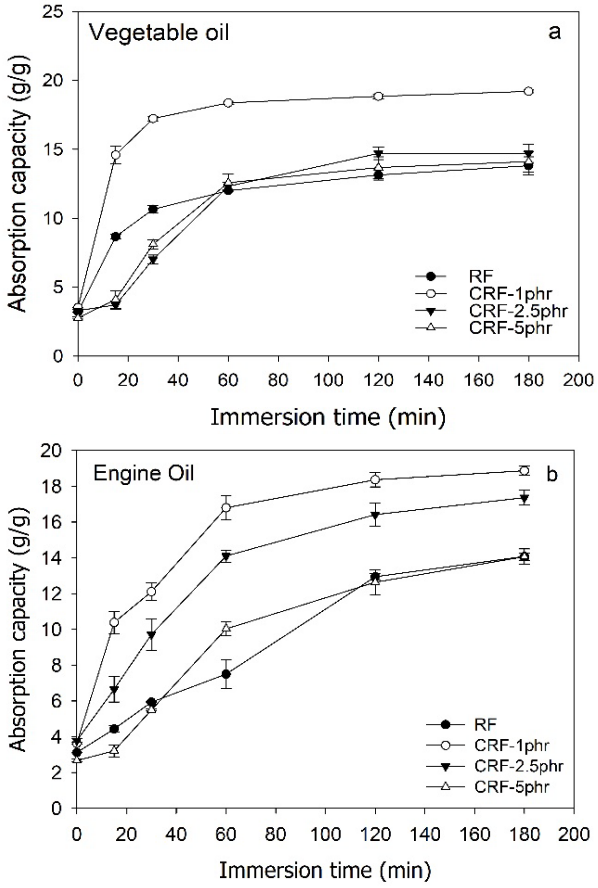

Figure 11 Absorption capacity of RF and CRF. From the graph (a) vegetable oil and (b) engine oil.

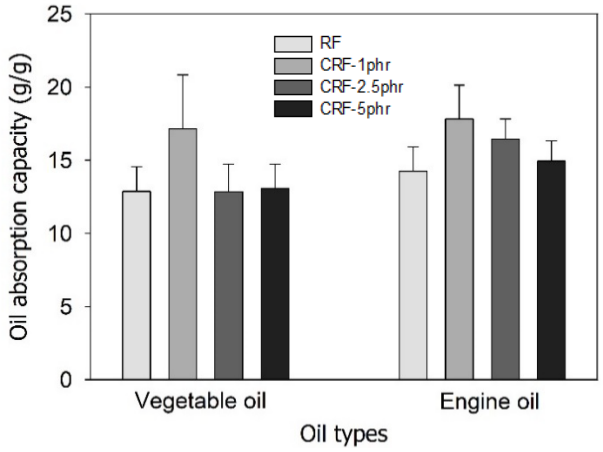

Figure 12 Oil absorption capacity of RF and CRF. From the graph shows vegetable oil and engine oil.

Oil absorption capacity of RF and CRF

Figure 11 shows the oil absorption of both oils. It can be seen that CRF-1phr (6.8-11.1 g/g) had higher oil absorption in the first 15 minutes compared to RF (1.3-5.5 g/g), CRF-2.5phr (0.4-2.9 g/g), and CRF-5 phr (0.5-1.3 g/g), but CRF absorbs more oil than RF for 60 minutes or more (Figure 12). CRF-1phr (17.1-17.8 g/g) absorbs the most of both oils. Probably because KF-CNC makes the material porous enough to absorb oil when filled. The use of particles as additives, such as nanoparticles, is generally limited to foams. Because the foams are in a solid state during the oil or solvent absorption and extraction processes, the additive materials (in varying particle sizes) and the different sizes of pores in the foam play an essential role in defining the foam's absorption capacity. It is widely acknowledged that smaller nanoparticles and pores, i.e., smaller regions, have a more highly active surface area and boundaries. The considerably smaller size of the foam particles and pores aids in the molecular interactions of the adsorbate ions and groups for improved oil and solvent absorption ability [11].

The absorption of RF and CRF (CRF-1phr) in water is shown in Figure 13. RF and CRF-1phr absorbed with time intervals of 15, 30, 60, 120, and 180 minutes. The CRF-1phr were adsorbent absorbs more oil. Furthermore, the chart shows that RF and CRF do not absorb water but instead prefer to absorb oil first.

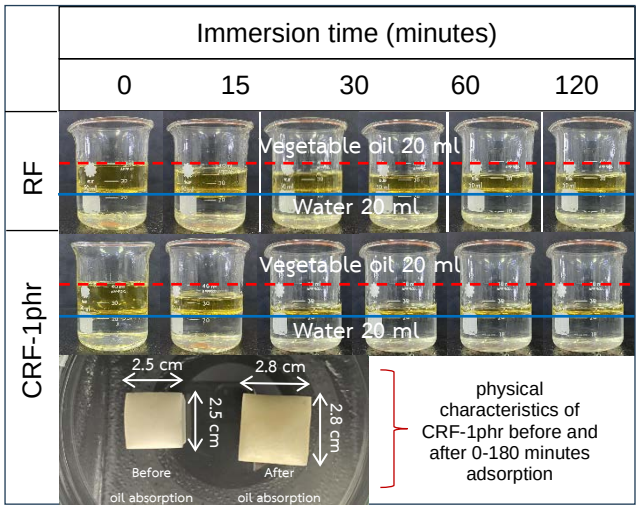

Figure 13 Absorption capacity of RF and CRF-1phr in water. The table shows the vegetable oil and physical characteristics of CRF-1 phr before and after 0-180 minutes adsorption.

Reusability of the CRF

CRF-1phr, the result of oil absorption by CRF, was selected to test the reusability of the material since it absorbs both types of oil the best (Figure 14) [12]. More than 50 times can be used with one CRF-

DOI: 10.60101/jarst.2023.254006

JOURNAL OF APPLIED RESEARCH ON SCIENCE AND TECHNOLOGY

1phr. Absorbs between 337.8 (Engine oil) and 553.4 (Vegetable oil) g/g without noticeably losing any of its quality over time. The difference in oil absorption between the two types of RF and CRF could be explained that the viscosity of Engine oil at the same temperature was lower than that of vegetable oil which was conducive to oil penetration into the porous skeleton of the RF and CRF. However, the low viscosity of the engine oil produced a negative effect on its adherence to the cellulose skeleton of the RF and CRF, resulting in a reduction in the amount of oil maintained in the RF and CRF [13].

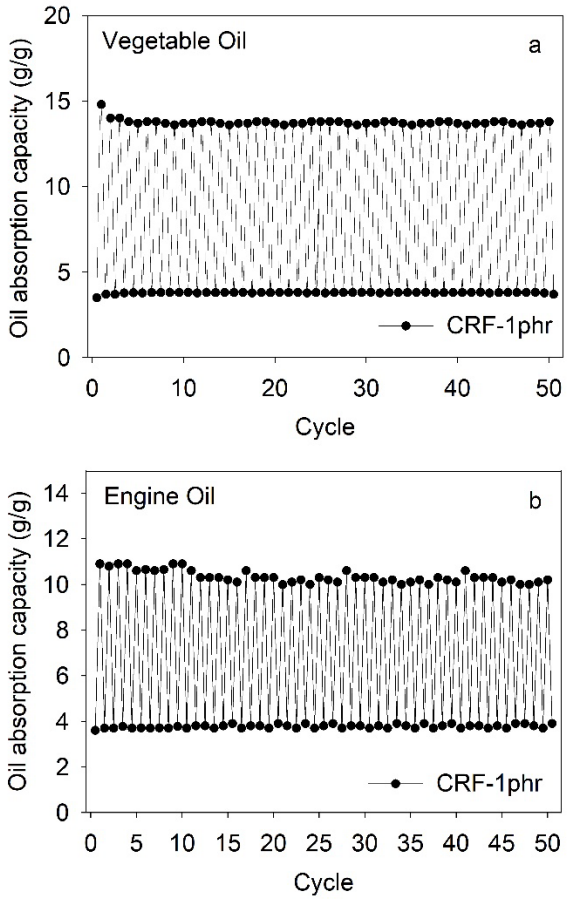

Figure 14 Reusability of CRF. From the graph (a) vegetable oil and (b) engine oil.

CONCLUSIONS

Results from KF and KF-CNC preparation

Chemical processes can be used to produce KF. Hydrogen peroxide and sodium hydroxide were used as the chemical treatments. According to the results of the morphological tests, chemical cleaning made the fibers purer than those seen with a scanning electron microscope (SEM), and the fact that KF are nanometer-sized indicates that hydrolysis can reduce the fiber size down to the nanometer level observed with a transmission electron microscope (TEM). On the NMR curve, it can be noticed that there are 17, 52, and 148 ppm of missing waves after the line improvement by chemical technique. This demonstrates that the fiber is purer in terms of fiber enhancement by chemical techniques. The end product of five centrifugations is KF-CNC water, which is produced by spinning at 9,000 rpm for 10 minutes at 25 °C. And a 72% yield of KF-CNC can be obtained by centrifuging it at 10°C for 50 minutes.

Results from RF and CRF preparation

The properties of RF and CRF at densities of 0, 1, 2.5, and 5 phr appear in the morphological results of RF and CRF from SEM micrographs 75x. It was discovered that the foam cell structure had an open-cell morphology. When KF-CNC and RF are mixed, the KF-CNC is scattered throughout the rubber foam, where the KF-CNC position is scattered freely. The spread of KF-CNC makes it harder to produce large air bubbles, resulting in smaller foam porosity [14].

RF peaks were observed in the FTIR microscopy data at 1209.4, 1270.8, and 1502.5 cm^{-1}. To produce CRF, however, CNC was added, and it was seen that the apparent peak progressively vanished. The amount of KF-CNC employed in the study was chosen at 0, 1, 2.5, and 5 phr to make CRF. It was discovered that as the amount of KF-CNC grows, the density of CRF increases. Compression % in CRF reduced. When the concentration of KF-CNC was raised. In the oil absorption test for both vegetable oil and engine oil, it was discovered that at 1 phr (CRF-1phr), it absorbs more oil (17.1-17.8 g/g) and faster in the first 15 minutes, and it can also be reused more than 50 times. The adsorbed content ranged from 337.76 to 553.33 g/g and did not absorb water but instead preferred to absorb oil first. The difference in oil absorption between the two types of RF and CRF from the decrease in compression % shows that 1 phr is soft, but 2.5 phr and 5 phr are hard, causing poor oil retention performance.

ACKNOWLEDGEMENT

The research project funded by the fundamental fund (FF) of Rajamangala University of Technology Thanyaburi under the annual research and innovation promotion fund 2022 (FRB65E0708) was created and achieved with the encouragement and assistance of many individuals and associations, to whom the researchers should be grateful on this occasion.

REFERENCES

1. Phomrak S, Nimpaiboon A, Newby B-mZ, Phisalaphong M. Natural rubber latex foam reinforced with micro- and nanofibrillated cellulose via Dunlop method. Polymers. 2020;12(9):1959.
2. Karim AFA, Ismail H, Ariff ZM. Properties and characterization of kenaf-filled natural rubber latex foam. BioResources. 2016;11(1):1080-91.
3. Kengkhetkit N, Amornsakchai T. Utilisation of

DOI: 10.60101/jarst.2023.254006

pineapple leaf waste for plastic reinforcement: 1. A novel extraction method for short pineapple leaf fiber. Ind Crop Prod. 2012;40:55-61.

4. Dong T, Xu G, Wang F. Oil spill cleanup by structured natural sorbents made from cattail fibers. Ind Crop Prod. 2015;76:25-33.
5. Lee BM, Jeun JP, Kang PH, Choi JH, Hong SK. Isolation and characterization of nanocrystalline cellulose from different precursor materials. Fiber Polym. 2017;18:272-7.
6. Arnata IW, Suprihatin S, Fahma F, Richana N, Candra Sunarti T. Cellulose production from sago frond with alkaline delignification and bleaching on various types of bleach agents. Orient J Chem. 2019;35(1):8-19.
7. Pantamanatsopa P, Ariyawiriyanan W, Ekgasit S. Production of Cellulose Nanocrystals Suspension with High Yields from Water Hyacinth. J Nat Fibers. 2023;20(1):2134266.
8. 395 AD. Standard test method for rubber property-compression set of vulcanized rubber. 1955.
9. Yuan Y, Shutov F. Foam-in-foam polyurethane composite. J Cell Plast. 2002;38(6):497-506.
10. 726-12 Standard Test Method for Sorbent Performance of Adsorbents 2012. ASTM F, editor. ASTM Philadelphia.
11. Dilamian M, Noroozi B. Rice straw agri-waste for water pollutant adsorption: Relevant mesoporous super hydrophobic cellulose aerogel. Carbohydr Polym. 2021;251:117016.
12. Ratcha A, Samart C, Yoosuk B, Sawada H, Reubroycharoen P, Kongparakul S. Polyisoprene modified poly (alkyl acrylate) foam as oil sorbent material. J Appl Polym Sci. 2015;132(42).
13. Udayakumar KV, Gore PM, Kandasubramanian B. Foamed materials for oil-water separation. Chemical Engineering Journal Advances. 2021;5:100076.
14. Yousefian H, Rodrigue D. Morphological, physical and mechanical properties of nanocrystalline cellulose filled Nylon 6 foams. J Cell Plast. 2016;53(3):253-71.

DOI: 10.60101/jarst.2023.254006

Received: September 13, 2023 | Revised: November 5, 2023 | Accepted: November 6, 2023

Boosting cordycepin production through plant-based oils for vegetarian consumption

Watcharin Yuttavanichakul*, Nipaporn Kanthong and Nuntaporn Pungsungvorn

Department of Biotechnology, Faculty of Science and Technology, Rajamangala University of Technology Tawan-ok, Chonburi 20110, THAILAND

*Corresponding author: Watcharin_yu@rmutto.ac.th

ABSTRACT

Cordyceps fungi, including species such as *Cordyceps sinensis* and *Cordyceps militaris*, are known for producing bioactive chemicals, notably cordycepin. Traditional cordyceps cultivation in Thailand relies on silkworm pupae as a substrate in solid-state fermentation, posing challenges in catering to vegetarian consumers. This study aimed to develop a solid-state fermentation process for cordyceps cultivation using vegetable oils, thus modifying the cereals medium and eliminating the need for silkworm pupae while enhancing bioactive chemical production and promoting cordyceps growth. The findings demonstrate that *C. militaris* can successfully grow and produce adenosine and cordycepin when the culture medium is modified with plant oils. Plant oils, including olive, soybean, peanut, palm, sesame, coconut, and sunflower oil, proved effective for cultivating *C. militaris* on PDA. Notably, adding a 3% mixture of palm oil in PDA resulted in the most significant promotion of *C. militaris* mycelium, with a diameter of 5.93 cm. Consequently, the modified cereals medium, incorporating palm oil, was adopted for solid-state fermentation of *C. militaris*. The results demonstrate that *C. militaris* can be successfully cultured to produce fruiting bodies comparable and total yields to those obtained using traditional cereals and silkworm pupa medium. Furthermore, there is a notable increase in adenosine and cordycepin production, indicating the potential of this method to enhance *C. militaris* yield and bioactive chemical output. This research highlights the feasibility of incorporating plant oils as substitutes or additives to silkworm pupae, improving productivity and enabling the production of *C. militaris* suitable for vegetarian consumption.

Keywords: C. militaris, Adenosine, Cordycepin, Vegetable oils, Vegetarian

INTRODUCTION

Cordyceps is a mushroom that has gained significant popularity as a widely consumed and highly sought-after product in the global market. The emergence of the COVID-19 pandemic has further increased the focus on maintaining health, leading to a heightened interest in cordyceps. These mushrooms have a long history of traditional medicinal use spanning thousands of years. Scientists from various fields have studied the nutritional benefits and bioactive compounds found in cordyceps, focusing on the important compound called cordycepin. Cordycepin, also known as 3'-deoxyadenosine, is a bioactive compound abundantly present in *Cordyceps* spp. Its potential therapeutic properties have captured significant attention within the scientific community. Cordycepin exhibits various biological activities, including anti-inflammatory, anticancer, antiviral, immunomodulatory, and antioxidant effects [1-3]. The medical field has embraced the application of cordyceps to enhance immunity and treat various diseases, including cancer, kidney disease, and diabetes [4]. Moreover, they have found utilization in the beauty industry and as health supplements [5]. Cordycepin has exhibited significant antiviral activity against various viruses, including influenza, hepatitis B, and herpes simplex [6]. While the therapeutic potential of cordyceps is promising across various domains, further research is warranted to elucidate their mechanisms of action and clinical applications comprehensively. Acknowledging that the properties and active compounds may exhibit variations among different Cordyceps species and cultivation conditions is important.

Cultivating cordyceps holds immense potential for harnessing their medicinal benefits. The cultivation process involves the propagation and maintenance of fungal cultures, ultimately providing a sustainable source for cordycepin production. Numerous studies have dedicated efforts toward developing efficient and reliable cultivation techniques. For instance, [7] explored the cultivation of cordyceps using a solid-state fermentation method. They optimized growth conditions, including the choice of substrate, moisture content, temperature, and pH, to enhance cordycepin

DOI: 10.60101/jarst.2023.254104

production. The results demonstrated a significant increase in cordycepin content in the cultivated mushrooms, thereby establishing them as a valuable source of this bioactive compound. Similarly, [8] delved into submerged fermentation of cordyceps, investigating the influence of various fermentation parameters such as carbon and nitrogen sources, pH, and agitation on cordycepin production. Their optimization efforts yielded higher yields of cordycepin, providing valuable insights into the industrial-scale production of this valuable compound. These cultivation studies not only contribute to the understanding of cordyceps biology but also present practical approaches for sustainable production. By optimizing cultivation conditions, it becomes possible to obtain cordyceps with elevated concentrations of the bioactive compound, thus maximizing their potential therapeutic benefits. It is worth noting that mushroom farmers face challenges in cultivating high-quality cordyceps due to low levels of cordycepin and low yields. Consequently, this results in low profits despite high production costs. Typically, the price of cordyceps is determined based on the number of active compounds found per gram and the mushroom size. Particularly, cordyceps exhibiting a high content of cordycepin per gram command higher prices. Environmental conditions, mushroom strains, and cultivation methods influence the quantity of active compounds. One promising approach involves cultivating cordyceps using silkworm substrate. Silkworms produce silk, rich in fatty acid, protein, and nutrients and an ideal medium for cordyceps growth. Several studies have investigated the cultivation of cordyceps using silkworm substrate, providing valuable insights into the techniques and benefits associated with this approach. For instance, [9] studied cultivating *Cordyceps militaris* using silkworm pupae as the substrate. The results demonstrated a significant increase in the production of bioactive compounds, including cordycepin and adenosine. The use of silkworm substrate not only enhanced the growth and yield of cordyceps but also enriched them with essential nutrients. The study highlighted the potential of silkworm pupae residue as a cost-effective and sustainable alternative to traditional substrates. Using this substrate resulted in a higher production of bioactive compounds, increased antioxidant activity, and improved yield of cordyceps.

While cordyceps offer numerous health benefits, it is essential to consider dietary aspects before consuming them. In particular, individuals adhering to vegetarian diets should be aware that cordyceps cannot be classified as vegetarian-friendly. Traditionally, cordyceps grow as parasitic fungi on the larvae of insects, specifically caterpillars. This natural growth process involves the fungus colonizing and eventually replacing the host organism. Consequently, the harvested cordyceps contain remnants of the caterpillar host. Due to this characteristic, cordyceps are not suitable for vegetarian consumption. However, alternative cultivation methods could be developed, such as growing cordyceps on cereal substrates, excluding the involvement of insect hosts. These cultivation methods provide a viable option for vegetarians to enjoy the benefits of cordyceps without compromising their dietary preferences. Cultivating cordyceps presents an opportunity to tap into their medicinal benefits sustainably, and it is important to ensure that their consumption is accessible. However, exploring the use of locally available plant oils in cordyceps cultivation on cereal substrates is an intriguing avenue for improving cordycepin content, developing cost-effective cultivation formulas, and making them accessible to all consumers. Research reports have indicated that adding coconut oil, corn oil, and sunflower oil in appropriate quantities can promote mycelial growth and enhance the production of exo-biopolymer in *C. militaris* [10]. Furthermore, incorporating peanut oil as a secondary carbon source in liquid static cultivation has shown a significant increase in cordycepin content, up to 5.26 grams per liter or approximately 3.17 times higher than the normal method [11]. These reports underscore the limited research on the effects of using plant oils and fatty acids to boost cordycepin content in cordyceps cultivation. Moreover, there is a lack of studies focusing on using locally available plant oils in Thailand to enhance cordycepin production in cordyceps cultivation using cereal substrates, which are widely accessible and hard to shortage. Consequently, investigating the utilization of locally available plant oils to improve cordycepin production efficiency in cordyceps cultivation on cereal substrates of solid-state fermentation holds great interest. Therefore, this study aims to investigate the effect of using locally available plant oils on the growing and cordycepin concentration of cordyceps cultivation using cereal substrates. Such endeavors will contribute to the development of a cost-effective and high-quality cultivation formula with a high cordycepin content, accessible to all consumer groups and beneficial for cordyceps farmers in Thailand.

MATERIALS AND METHODS

Isolation and culture

C. militaris was isolated from a commercial fresh cordyceps product. The cordyceps were cultured on peptone-added potato dextrose agar (PPDA) slants at 25 °C. The culture was allowed to grow for 10 days and then stored at 4 °C for stock purposes.

Liquid spawn preparation

Liquid spawn was prepared using a liquid medium modified from [8] consisting of glucose (20 gL^{-1}), peptone (5 gL^{-1}), beef extract (3 g L^{-1}), and yeast extract (1 gL^{-1}). In a 250 mL flask, 100 mL of the liquid

DOI: 10.60101/jarst.2023.254104

JOURNAL OF APPLIED RESEARCH ON SCIENCE AND TECHNOLOGY

medium was aseptically transferred. A small piece (~0.5 cm^2)of the mycelial slant from the PPDA culture was then inoculated into the flask. The flask was incubated at a temperature of 25 °C with shaking at 120 rpm. The mycelia were allowed to grow for approximately 7 days in the liquid medium. During this period, optimal growth of the mycelia was observed. After 7 days, the spawn culture was diluted by adding four volumes of sterile distilled water. The spores were obtained by observing under a microscope using a hematocytometer to obtain a 10^6 spores/mL concentration before being used to inoculate media for fruit body production.

The optimal growth differences in plant oil concentrations

Cork Borer cut the cutter to a 5-mm disc. Subsequently, the disc was transferred to the central of a fresh Petri dish containing potato dextrose agar (PDA) supplemented with various plant oils, modified from [10] including olive oil, soybean oil, peanut oil, palm oil, sesame oil, coconut oil, and sunflower oil, at different concentrations of 0%, 1%, 3%, and 5% (v/v). The cultures were then incubated at a temperature of 25 °C with a light-dark cycle of 12 hours each, under white fluorescent light with an intensity of 1600 lx. The relative humidity was maintained above 70% throughout the week-long incubation period. The growth of the colonies was assessed by measuring their diameter, allowing for the determination of the growth rate. To ensure reliable results, each experiment was conducted with six replicates.

The fruiting body formation medium with plant oil with solid-state fermentation

The fruiting body formation medium was modified by introducing a plant oil treatment, while the control medium (CM) consisted of a 500 mL glass bottle (17 oz) containing 60 g of brown rice and 80 mL of distilled water. For the positive control cereals and silkworm pupa medium (CSM), a 500 mL glass bottle contained 60 g of brown rice, 20 mL of silkworm pupa spinning juice, and 60 mL of distilled water. In contrast, the modified cereals medium (MCM) included 60 g of brown rice, 2.4 mL of palm oil, and 77.6 mL of distilled water in the same 500 mL glass bottle. Both mixtures were sterilized at 121 °C for 20 minutes. After cooling, 25 mL of liquid inoculum was added to each fruiting medium. The incubation process took place at a temperature of 25 °C with a light-dark cycle of 12 hours each, under white fluorescent light with an intensity of 1600 lx for 60 days and with a relative humidity maintained between 70%. The formation of fruiting bodies was assessed about the grains. Total yields of fruiting body production were calculated as follows:

$$\text{Total yields} = F + S$$

Where, F = mg dry weight of fruiting body part

S = mg dry weight of fruiting body part

Bioactive compound analysis

Fruit bodies obtained from each sample were dried in the oven to a constant weight at 60 °C for 3 days. The dried samples were then pulverized to a particle size smaller than 20-mesh using a hammer mill. To extract adenosine and cordycepin, 0.5 g of the dry powder was suspended in 50 mL of doubly deionized water and sonicated for 3 hours in an ultrasonic bath operating at 50 kHz and 400 W. The resulting supernatant, obtained by centrifuging at 1740 × g for 15 minutes, was filtered through a 0.45 µm membrane filter. High-performance liquid chromatography (HPLC) analysis was conducted using an Agilent 1100 Series HPLC system from Agilent Technologies Inc. in Santa Clara, CA, USA. The method was modified from [1]. The separation and detection conditions for adenosine and cordycepin were as follows: a C18 column (4.6 mm × 150 mm, with a particle size of 5 µm) from Agilent, a mobile phase composed of 10 mmol L^{-1} KH_2PO_4 buffer (pH 6.0) and methanol in a ratio of 85:15 (v/v), a flow rate of 0.8 mL min^{-1}, a column temperature of 30 °C, and detection at a wavelength of 260 nm using a UV-visible detector. The analysis of cordycepic acid from the extracts was carried out at a column temperature of 35 °C and a refractive index detector temperature of 35 °C. The mobile phase for Cordycepic acid analysis consisted of deionized water, with a flow rate of 0.6 mL min^{-1}. The injection volume in the HPLC system was set to 20 µL.

Statistical analysis

Data were analyzed with SPSS Software Package v.18. All variables were tested for normality using the Kolmogorov-Smirnov. Normally distributed data were analyzed using ANOVA. Variance homogeneity was confirmed by Levene's test for variance homogeneity ($P > 0.05$). Significant differences between treatment effects were determined by one-way ANOVA analysis, followed by Duncan's tests, and $p < 0.05$ was considered statistically significant.

RESULTS AND DISCUSSIONS

Growth of C. militaris on different plant oil

In order to explore the potential utilization of these plant oils as components in the solid medium to replace silkworm pupa for cultivating *C. militaris*, the mycelial growth was assessed by cultivating *C. militaris* on PDA mixed with each type of plant oil at various concentrations. The findings revealed that the mycelial growth of *C. militaris* on PDA medium mixed with palm oil at a concentration of 3% exhibited the most favorable outcomes among all the tested. This outcome was statistically significant, as shown in Table 1. Likewise, the mycelial growth on PDA medium mixed with olive oil at a concentration of 3% demonstrated superior

DOI: 10.60101/jarst.2023.254104

performance compared to 1% and 5%, respectively (Table 1 and Figure 1 a-d). Similarly, the mycelial growth on PDA medium mixed with sunflower oil at 1% yielded better results than concentrations of 3% and 5% (Table 1 and Figure 1 e-h). The mycelial growth on PDA medium mixed with soybean oil at a concentration of 1% exhibited better results compared to concentrations of 3% and 5% (Table 1 and Figure 1 i-l). Similarly, the mycelial growth on PDA medium mixed with peanut oil at a concentration of 1% demonstrated better results compared to concentrations of 3% and 5% (Table 1 and Figure 1 m-p). Additionally, the mycelial growth on PDA medium mixed with sesame oil at a concentration of 1% showed better results compared to concentrations of 3% and 5% (Table 1 and Figure 1 q-t). Furthermore, the mycelial growth on PDA medium mixed with palm oil at a concentration of 3% exhibited better results compared to concentrations of 1% and 5% (Table 1 and Figure 1 u-x). Moreover, the mycelial growth on PDA medium mixed with coconut oil at a concentration of 3% demonstrated better results than concentrations of 1% and 5% (Table 1 and Figure 1 aa-ad). These results indicate that palm oil, olive oil, and coconut oil at a concentration of 3% and sunflower oil, peanut, and sesame oil at 1% are the most effective concentrations for promoting the mycelial growth of *C. militaris* in PDA medium. The addition of optimum palm oils significantly promoted the mycelial growth of *C. militaris* in static culture. Oils, in general, can be partially incorporated into the cell membrane, facilitating the immediate uptake of nutrients from the culture medium and stimulating mycelial growth [12]. However, the growth of the fungus was completely inhibited by short-chain fatty acids with a carbon chain length shorter than 10, such as capric acid, caproic acid, propionic acid, and acetic acid [13, 14]. The main components of plant oil, such as corn oil, cottonseed oil, palm oil, and soybean oil, are linoleic acid and palmitic acid, which are believed to benefit mycelial growth [15]. It is worth noting that palm oil contains 45% palmitic acid and 44% linoleic acid, which appear to play a role in stimulating mycelial growth. Additionally, palmitic acid is the most stimulating factor for mycelial growth, resulting in an 18.3-fold increase during a 3-week incubation of *Hericium erinaceum* [16].

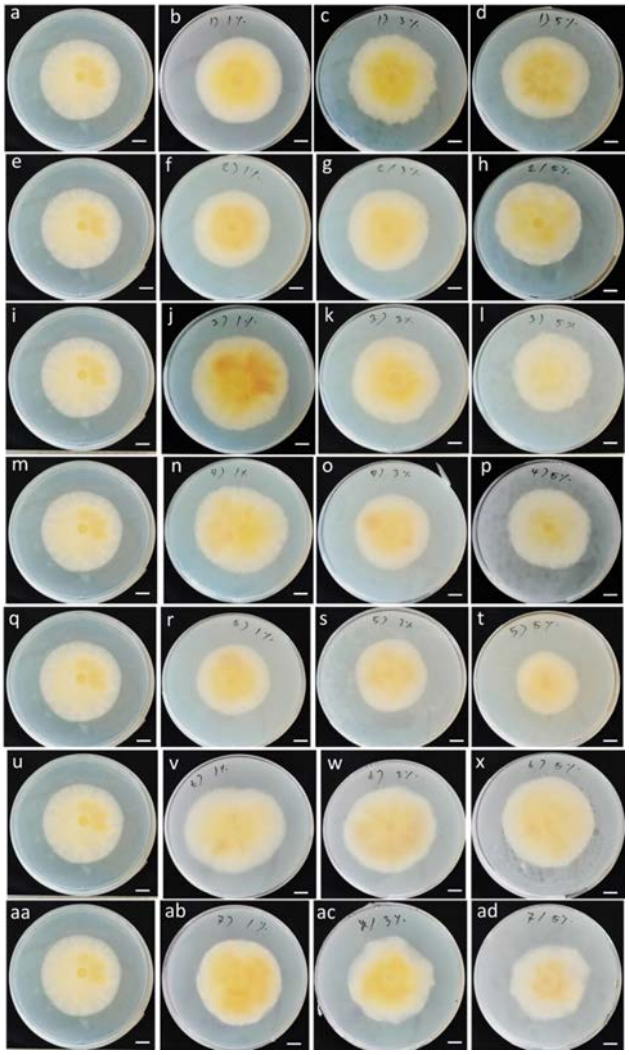

Figure 1 Colony of *C. militaris* on PDA agar medium under 0, 1, 3, 5, (V/V) of each plant oil; olive oil (a-d); sunflower oil (e-h); soybean oil (i-l); peanut oil (m-p); sesame oil (q-t); palm oil (u-x) and coconut oil (aa-ad). - white bar scale reference value = 1 cm.

Table 1 Growth of *C. militaris* on agar medium under 0, 1, 3, and 5% of plant oils.

Treatments	Colony or hyphae diameter (centimeters)			
	Plant oil concentration (%v/v)			
	0 %	1 %	3 %	5 %
PDA (control)	5.43 ^{abcd} ± 0.05	-	-	-
PDA + olive oil	-	5.26 ^{bcde} ± 0.23	5.66 ^{ab} ± 0.09	5.00 ^{cde} ± 0.00
PDA + sunflower oil	-	5.06 ^{bcde} ± 0.23	4.90 ^{de} ± 0.06	5.00 ^{cde} ± 0.12
PDA + soybean oil	-	5.50 ^{abc} ± 0.25	5.46 ^{abcd} ± 0.15	5.16 ^{abcde} ± 0.09
PDA + peanut oil	-	5.66 ^{ab} ± 0.17	5.00 ^{cde} ± 0.29	5.16 ^{abcde} ± 0.17
PDA + sesame oil	-	5.16 ^{abcde} ± 0.33	4.66 ^{e} ± 0.17	4.13 ^{f} ± 0.09
PDA + palm oil	-	5.73 ^{ab} ± 0.15	5.93 ^{a} ± 0.12	5.33 ^{abcd} ± 0.17
PDA + coconut oil	-	5.60 ^{ab} ± 0.10	5.66 ^{ab} ± 0.09	5.23 ^{abcde} ± 0.15
C.V. (%)	0.00	0.05	0.08	0.08

Letters denote significant differences between mean using a post hoc Duncan's multiple comparisons test. ($P < 0.05$) after one-way ANOVA. Values are means (±SEM, n = 6).

DOI: 10.60101/jarst.2023.254104

JOURNAL OF APPLIED RESEARCH ON SCIENCE AND TECHNOLOGY

Fruit body production and bioactive compound of C. militaris on different fruiting body formation medium

Through the experimental use of a 3% mixture of palm oil in the PDA medium, evidence suggests a tendency to enhance the growth of *C.militaris* fruiting body. In order to culture *C. militaris*, MCM was utilized and compared with the CM and CSM over 60 days. The results revealed that the MCM significantly impacted the dry weight of *C. militaris* fruiting bodies, solid-based residues, and total yields, which measured 9.75, 20.67, and 30.42 mg, respectively. These values did not differ significantly from cultivating in the CSM, where the dry weight of *C. militaris* fruiting bodies, solid-based residues, and total yields were 9.88, 20.74, and 30.58 mg, respectively.

Table 2 Fruiting body production of *C. militaris* on fruiting body formation medium.

Fruiting body formation medium	Fruiting body production of *C. militaris*		
	Fruiting body (mg dry weight)	Solid-based residues (mg dry weight)	Total yields (mg dry weight)
Cereals (CM)	3.23 ^{b} ±0.87	17.65 ^{b} ±1.75	20.88 ^{b} ±1.25
Cereals and silkworm pupa (CSM)	9.83 ^{a} ±1.19	20.74 ^{a} ±1.94	30.58 ^{a} ±1.57
Modified fruiting body (MCM)	9.75 ^{a} ±0.81	20.67 ^{a} ±2.55	30.42 ^{a} ±1.88
C.V. (%)	0.40	0.07	0.16

Letters denote significant differences between mean using a *post hoc* Duncan's multiple comparisons test (P< 0.05) after one-way ANOVA. Values are means (±SEM, n=3).

Figure 2 Fruiting body of *C. militaris* on fruiting body formation medium; a: CM; b: CSM and c: MCM.

Table 3 Bioactive compound of *C. militaris* extracted from different fruiting body formation medium.

Fruiting body formation medium	Bioactive compound (mg/g)		Bioactive compound (ug) per Total yields or Production	
	Adenosine	Cordycepin	Adenosine	Cordycepin
Cereals (CM)	0.17 ^{ns} ±0.00	0.74 ^{ns} ±0.00	3.55 ^{b} ±0.21	16.07 ^{c} ±0.92
Cereals and silkworm pupa (CSM)	0.22 ^{ns} ±0.00	1.03 ^{ns} ±0.00	6.72 ^{a} ±0.34	31.49 ^{a} ±1.67
Modified fruiting body (MCM)	0.20 ^{ns} ±0.00	0.81 ^{ns} ±0.00	6.08 ^{a} ±0.37	24.64 ^{b} ±1.56
C.V. (%)	0.15	0.12	0.27	0.26

Letters denote significant differences between mean using a *post hoc* Duncan's multiple comparisons test (P< 0.05) after one-way ANOVA. Values are means (±SEM, n=3). ns = non-significant

However, MCM and CSM mediums exhibited notable differences when cultivating with CM, yielding statistically significant results. The dry weight of the fruiting bodies, solid-based residues, and total yields were 3.23, 17.65, and 20.88, respectively (Table 2). The culture of *C. militaris* on different fruiting body formation mediums at 60 days is shown in figure 2.

For the examination of bioactive compounds of *C. militaris* extraction from different fruiting body formation medium, the chromatograms obtained from the analysis of each sample of *C. militaris* extraction solution using HPLC technique were compared with the chromatograms of standard solutions containing cordycepin and adenosine. It was found that in the chromatograms of CM, CSM, and MCM, there were peaks at retention times matching those of the peaks found in the standard solutions (figure 3). This indicates the ability of *C. militaris* to produce adenosine and cordycepin in each fruiting body formation medium. By calculating the area under the peaks on the chromatogram, the quantities of important substances in *C.militaris* were determined (Table 3). It was found that the highest amounts of adenosine and cordycepin were present in *C. militaris* obtained from CSM, with quantities of 0.22 mg/g and 1.03 mg/g, respectively. The next highest amounts were found in *C. militaris* from MCM, with 0.20 mg/g and 0.81 mg/g, respectively. The lowest amounts of adenosine and cordycepin

DOI: 10.60101/jarst.2023.254104

were found in *C. militaris* obtained from CM, with 0.20 mg/g and 0.81 mg/g, respectively. The data presented in Tables 2 and 3 demonstrate that utilizing MCM and CSM in a 500 mL glass bottle (17 oz) resulted in significantly higher yields from one crop of *C. militaris* than CM. The crop produced approximately 1.45 and 1.46 times more bioactive compounds, with adenosine levels about 1.8 and 1.7 times higher and cordycepin levels about 1.95 and 1.53 times higher, respectively. These findings indicate the potential benefits of using MCM and CSM for enhanced production of bioactive compounds in *C. militaris*. In terms of fruit body production and the production of bioactive compounds of *C. militaris*, the common use of glucose as a carbon and energy source for microorganisms generates growth and secondary metabolites [17].

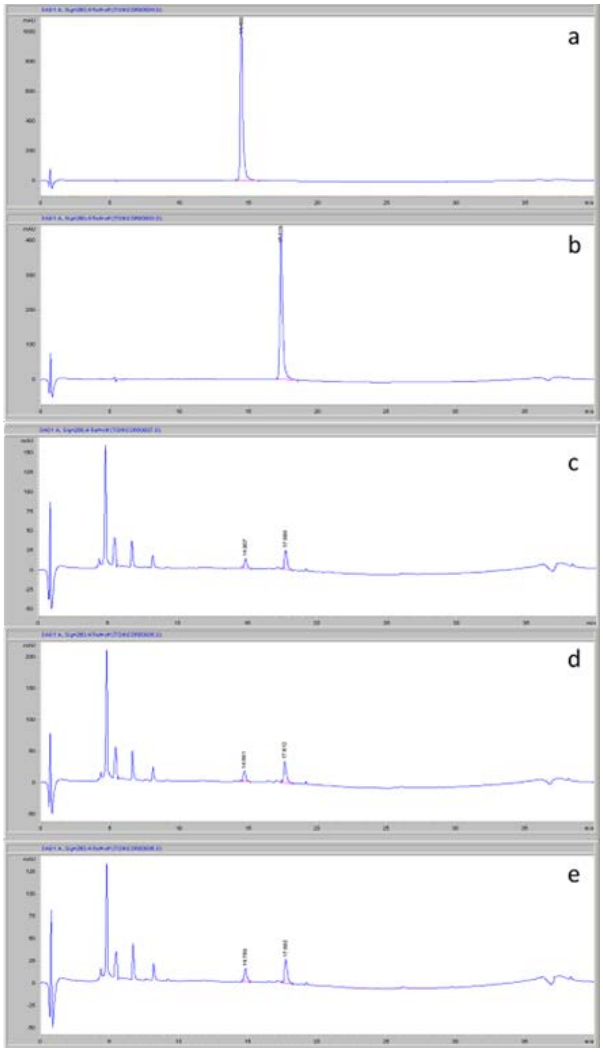

Figure 3 HPLC Chromatogram of bioactive ingredients. Peaks are indicated as follows: (a) Standard adenosine (RT=14.48), (b) Standard cordycepin (RT=17.82), (c) Cereals, (d), Cereals and silkworm pupa, and (e) Modified fruiting body.

However, the rapid breakdown of glucose can reduce the biosynthesis rate of various secondary metabolites [18] and hinder the utilization of alternative carbon sources [19, 20]. Vegetable oils have been introduced as carbon sources to counter carbon catabolite repression due to their low solubility in the culture medium [21]. Additionally, vegetable oils, commonly employed as defoamers in submerged fermentation [22], have demonstrated their ability to stimulate mycelial growth in several medicinal mushrooms, thereby augmenting the production of bioactive metabolites [23, 24]. The incorporation of plant oils, fatty acids, and other carbon sources has been observed to induce the accumulation of exo-polysaccharides and facilitate cell differentiation in various mushrooms, including *Grifola frondosa* [25], *Inonotus obliquus* [26], *C. militaris* [10], and *Ganoderma lucidum* [27]. Notably, [28] reported that oil in the medium promotes the elongation of filamentous fungi. It has been postulated that oils or fatty acids can modify the cell membrane, thereby increasing permeability and stimulating the production of biopolymers [29]. Furthermore, [11] observed positive effects on the up-regulation of the glyoxylate, pentose phosphate, and cordycepin biosynthesis pathways upon adding peanut oil to *C. militaris* culture. Experimental evidence suggests that cordycepin precursor can derive from two sources: adenosine from the purine biosynthesis pathway and 2′,3′-cyclic monophosphate (2′,3′-cAMP) from mRNA degradation. Both compounds can be converted to adenosine-3′-monophosphate (3′-AMP). Subsequently, 3′-AMP is dephosphorylated to 2′-carbonyl-3′-deoxyadenosine (2′-C-3′-dA) by Cns2, ultimately leading to cordycepin through the oxidoreductase Cns1 [30]. Combining plant oil and glucose as dual carbon sources seems to be a promising strategy for enhancing intracellular carbon accumulation and cordycepin production in static culture.

CONCLUSION

In conclusion, the study investigated two aspects related to the cultivation of *C. militaris*. Firstly, in terms of the growth of *C. militaris* on different plant oils, it was found that palm oil at a concentration of 3%, olive oil at a concentration of 3%, sunflower oil at a concentration of 1%, peanut oil at a concentration of 1%, sesame oil at a concentration of 1%, and coconut oil at a concentration of 3% were the most effective concentrations for promoting the mycelial growth of *C. militaris* on PDA medium. Secondly, regarding the fruit body production of *C. militaris* on different fruiting body formation mediums, the use of MCM and CSM resulted in similar outcomes concerning the dry weight of the fruiting bodies, solid-based residues, and total yields, which were comparable to cultivating in the CSM medium. However, both MCM and CSM mediums significantly differed from cultivating with CM, indicating the importance of choosing a fruiting body formation medium for optimal results. These findings suggest that palm oil, olive oil, sunflower oil,

DOI: 10.60101/jarst.2023.254104

peanut oil, sesame oil, and coconut oil can be considered potential components in the solid medium for cultivating *C. militaris*, and that MCM and CSM are effective mediums for fruit body production.

Further research and optimization of these mediums can contribute to the efficient cultivation and production of *C. militaris* for vegetarian consumption, which has potential applications in bioactive compound production and health-related industries.

ACKNOWLEDGEMENT

This research was supported by the Faculty of Science and Technology, Rajamangala University of Technology Tawan-ok.

REFERENCES

1. Chaicharoenaudomrung N, Jaroonwitchawan T, Noisa P. Cordycepin induces apoptotic cell death of human brain cancer through the modulation of autophagy. In Vitro Toxicol. 2018;46:113-21.
2. Ashraf SA, Elkhalifa AEO, Siddiqui AJ, Patel M, Awadelkareem AM, Snoussi M, et al. Cordycepin for health and wellbeing: a potent bioactive metabolite of an entomopathogenic medicinal fungus Cordyceps with its nutraceutical and therapeutic potential. Molecules. 2020;25(12):2735.
3. Das G, Shin HS, Leyva-Gómez G, Prado-Audelo MLD, Cortes H, Singh YD, et al. *Cordyceps* spp.: A review on its immune-stimulatory and other biological potentials. Front Pharmacol. 2021;11: 2250.
4. Elkhateeb WA, Daba G. Cordyceps more than edible mushroom a rich source of diverse bioactive metabolites with huge medicinal benefits. Res J Environ Sci. 2022;3(5):566-74.
5. Kanlayavattanakul M, Lourith N. *Cordyceps militaris* polysaccharides: preparation and topical product application. Fungal Biol Biotechnol. 2023;10(1): 1-6.
6. Lee HH, Park H, Sung GH, Lee K, Lee T, Lee I, et al. Anti-influenza effect of *Cordyceps militaris* through immunomodulation in a DBA/2 mouse model. J Microbiol. 2014;52:696-701.
7. Adnan M, Ashraf SA, Khan S, Alshammari E, Awadelkareem AM. Effect of pH, temperature and incubation time on cordycepin production from *Cordyceps militaris* using solid-state fermentation on various substrates. CYTA - J Food. 2017;15(4): 617-21.
8. Xie CY, Gu ZX, Fan GJ, Gu FR, Han YB, Chen ZG. Production of cordycepin and mycelia by submerged fermentation of *Cordyceps militaris* in mixture natural culture. Appl Biochem Biotechnol. 2009; 158:483-92.
9. Jiaojiao Z, Fen W, Kuanbo L, Qing L, Ying Y, Caihong D. Heat and light stresses affect metabolite production in the fruit body of the medicinal mushroom *Cordyceps militaris*. Appl Microbiol Biotechnol. 2018;102:4523-33.
10. Park JP, Kim SW, Hwang HJ, Cho YJ, Yun JW. Stimulatory effect of plant oils and fatty acids on the exo-biopolymer production in *Cordyceps militaris*. Enzyme Microb Technol. 2002;31(3): 250-5.
11. Tang J, Qian Z, Wu H. Enhancing cordycepin production in liquid static cultivation of *Cordyceps militaris* by adding vegetable oils as the secondary carbon source. Bioresour Technol. 2018;268:60-7.
12. Melhuish Jr JH, Hacskaylo E, Bean GA. Fatty acid composition of ectomycorrhizal fungi in vitro. Mycol. 1975;67(5):952-60.
13. Martynova J, Kokina A, Kibilds J, Liepins J, Scerbaka R, Vigants A. Effects of acetate on Kluyveromyces marxianus DSM 5422 growth and metabolism. Appl Microbiol Biotechnol. 2016;100:4585-94.
14. Melin P, Stratford M, Plumridge A, Archer DB. Auxotrophy for uridine increases the sensitivity of *Aspergillus niger* to weak-acid preservatives. Microbiology. 2008;154(4):1251-7.
15. Andrikopoulos NK. Triglyceride species compositions of common edible vegetable oils and methods used for their identification and quantification. Food Rev Int. 2002;18(1):71-102.
16. Kang H, Hwang S, Lee H, Park W. Effects of high concentrations of plant oils and fatty acids for mycelial growth and pinhead formation of *Hericium erinaceum*. Trans ASABE. 2002;45(1):257.
17. Ruiz B, Chávez A, Forero A, García-Huante Y, Romero A, Sánchez M, et al. Production of microbial secondary metabolites: Regulation by the carbon source. Crit Rev Microbiol. 2010;36(2):146-67.
18. Park YS, Momose I, Tsunoda K, Okabe M. Enhancement of cephamycin C production using soybean oil as the sole carbon source. Appl Microbiol Biotechnol. 1994;40:773-9.
19. Lane S, Xu H, Oh EJ, Kim H, Lesmana A, Jeong D, et al. Glucose repression can be alleviated by reducing glucose phosphorylation rate in *Saccharomyces cerevisiae*. Sci Rep. 2018;8(1):1-12.
20. Unrean P, Khajeeram S. Model-based optimization of *Scheffersomyces stipitis* and *Saccharomyces cerevisiae* co-culture for efficient lignocellulosic ethanol production. Bioresour Bioprocess. 2015;2: 1-11.

DOI: 10.60101/jarst.2023.254104

21. Choi DB, Park SS, Ahn BK, Lim DH, Lee YW, Moon JH, et al. Studies on production of gentamicin from Micromonosporas purpurea using crude vegetable oils. Process Biochem. 2008;43(8): 835-41.
22. Kougias P, Boe K, Tsapekos P, Angelidaki I. Foam suppression in overloaded manure-based biogas reactors using antifoaming agents. Bioresour Technol. 2014;153:198-205.
23. Conti E, Stredansky M, Stredanska S, Zanetti F. γ-Linolenic acid production by solid-state fermentation of Mucorales strains on cereals. Bioresour Technol. 2001;76(3):283-6.
24. Kagliwal L, Survase S, Singhal R. A novel medium for the production of cephamycin C by *Nocardia lactamdurans* using solid-state fermentation. Bioresour Technol. 2009;100(9):2600-6.
25. Hsieh C, Wang HL, Chen CC, Hsu TH, Tseng MH. Effect of plant oil and surfactant on the production of mycelial biomass and polysaccharides in submerged culture of *Grifola frondosa*. Biochem Eng J. 2008;38(2):198-205.
26. Xu X, Quan L, Shen M. Effect of chemicals on production, composition and antioxidant activity of polysaccharides of *Inonotus obliquus*. Int J Biol Macromol. 2015;77:143-50.
27. Yang FC, Ke YF, Kuo SS. Effect of fatty acids on the mycelial growth and polysaccharide formation by *Ganoderma lucidum* in shake flask cultures. Enzyme Microb Technol. 2000;27(3-5):295-301.
28. Kendrick A, Ratledge C. Cessation of polyunsaturated fatty acid formation in four selected filamentous fungi when grown on plant oils. JAOCS. 1996;73: 431-5.
29. Stasinopoulos S, Seviour R. Stimulation of exopolysaccharide production in the fungus *Acremonium persicinum* with fatty acids. Biotechnol Bioeng. 1990;36(8):778-82.
30. Xia Y, Luo F, Shang Y, Chen P, Lu Y, Wang C. Fungal cordycepin biosynthesis is coupled with the production of the safeguard molecule pentostatin. Cell Chem Biol. 2017;24(12):1479-89.e4.

DOI: 10.60101/jarst.2023.254104

Received: September 19, 2023 | Revised: November 17, 2023 | Accepted: November 20, 2023

JOURNAL OF APPLIED RESEARCH ON SCIENCE AND TECHNOLOGY
JARST
INSTITUTE OF RESEARCH AND DEVELOPMENT
RAJAMANGALA UNIVERSITY OF TECHNOLOGY THANYABURI
ISSN ONLINE: 2773-9473
https://ph01.tci-thaijo.org/index.php/rmutt-journal

Optimization of ballistic vest for protective atrocity and stabbing

Montien O-thongkham[1] and Sujira Khorjitmate[2*]

[1]Division of Textile Technology, Faculty of Textile Industry, Rajamangala University of Technology Krungthep, Bangkok 10120, THAILAND

[2]Division of Textile Innovation Engineering, Faculty of Engineering, Rajamangala University of Technology Thanyaburi, Pathum Thani 12110, THAILAND

[*]Corresponding author: sujira@rmutt.ac.th

ABSTRACT

In the optimization of the ballistic vest to prevent atrocity and stabbing, two fabrics were utilized: a ballistic plate made of synthetic fiber Endumax® Shield XF 33 and Twaron® SRM 509. Test the thickness and weight of the fabric before being tested for atrocity and stabbing protection. Finally, test the ammunition protection. The results were as follows: (1) The thickness of Twaron® and Endumax® fabrics. The average was 0.44300 and 0.22000 mm., and the standard deviation and variance were low. (2) The weight of Twaron® and Endumax® fabrics. The average was 1.99300 and 1.45100 g., and the standard deviation and variance were low. (3) Protective atrocity P1/B at the L2, E1 level, the average energy is 33.176 joules. The average blade depth is 0 mm., within the specified standard. Protective atrocity P1/B at the L2 and E2 levels has an energy average of 50.52 joules. The average blade depth is 1 mm., which is also within the specified standard criteria. (4) Protective stabbing SP/B at the L2 and E1 levels, the energy average is 33.54 joules. The average blade depth is 0 mm., within the specified standard. Protective stabbing SP/B at the L2 and E2 levels, the average energy is 49.894 joules. The average blade depth is 7.6 mm., which is also within the specified standard criteria. (5) Ballistic vest plate test with 0.44 MAG SJHP ammunition 240 g. The average bullet velocity was 437.78 m/s. The collapse footprint is 19.6 mm., within the specified standard. Tested with 9 mm. FMJ ammunition 124 g. The average bullet velocity was 438.15 m/s. The collapse footprint is 18 mm., which is also within the specified standard criteria. From various test results, it can be concluded that the ballistic vest provides excellent protection according to military standards and is suitable for security officials' work.

Keywords: Ballistic vest, Atrocity and stabbing, Ammunition, Blades, Sharp materials

INTRODUCTION

The situation of violence in Thailand is not only in the southern border provinces alone [1, 2] but also expanding to other provinces, including in the major urban areas of various regions, all of which have more severe problems. Reducing losses in addition to the aforementioned measures for operators to perform the use of special equipment and equipment for the body protection of operators [3] to prevent the danger of gunshots or various types of weapons with bad intentions [4], such as ballistic vests, shields, and personal weapons.

The ballistic vest in use today is primarily used to protect short-barreled handgun shells for soft armor and long-barreled bullets for hard armor [5-7]. Nevertheless, in some cases, ballistic vests are worn by officers in urban or community areas to prevent and suppress riots, rallies, and protests. In order to prevent potential harm and reduce staff losses and injuries from past events, it is the duty of officers to prevent and suppress various incidents. Officers were frequently injured in clashes and the use of weapons by the group.

For the above reasons, the researcher, therefore, has an idea to develop the currently used ballistic vests to be more effective. In addition to protecting against bullets at the desired level. For officers to wear to work in urban areas or communities. In the case of preventing or suppressing non-violent events without using guns. However, other dangerous weapons are used instead, such as pointed weapons or sharp objects. For protection against atrocity and stabbing from sharp objects. By adding another layer of protection against atrocity and sharp objects to the front of the ballistic vest in addition to the general vest. If not in use, this atrocity and stabbing resistant insert can be removed from the ballistic vest.

MATERIALS AND METHODS

By adopting the fabric that has ballistic properties and the addition of the front armor plate

DOI: 10.60101/jarst.2023.254151

that has the ability to protect against sharp and pointed objects. To enhance the effectiveness of the ballistic vest, it should have two types of protection in 1 body [8].

In carrying out this research, we designed experimented with and selected fabrics to determine the patterns by stacking the 2 types of fabrics on top of each other, fabric type 1 was laminated fiber with an average weight of 0.108 grams per square inch. Fabric type 2 was coated woven fabric with an average weight of 0.294 grams per square inch, divided into three patterns. To try the best protection and suitability: (1) Endumax® Shield XF 33 quantity 26 layers + Twaron® SRM 509 quantity 2 layers (2) Endumax® Shield XF 33 quantity 32 layers + Twaron® SRM 509 quantity 3 layers and (3) Endumax® Shield XF 33 quantity 36 floors + Twaron® SRM 509 quantity 3 layers. The number of layers of the three types was determined to determine the best protection and overall weight of the suit to meet military standards.

Table 1 Fabric types and layer.

Fabric	Layer
Endumax® + Twaron®	26 + 2 (28)
Endumax® + Twaron®	32 + 3 (35)
Endumax® + Twaron®	33 + 3 (36)

Production process

Begin by gathering information about the fabric. Manufacturing and testing processes are used in research to optimize ballistic vests for protection against atrocity and stabbing (Figure 1). Then, test the properties of Twaron® SRM 509 and Endumax® Shield XF 33 fabric as follows: the fabric thickness test using the ASTM D 1777-96 standard and the weight of the fabric test using the ASTM D 77-96 standard.

Figure 1 Fabric for ballistic vest according to the pattern.

Production of ballistic plate with a prototype for protective atrocity and stabbing from Twaron SRM® 509 synthetic fiber and Endumax® Shield XF 33 fabric. According to the details of the pattern of two types of fabric and the size of the ballistic vest specified.

Production of the ballistic vest with a prototype for protective atrocity and stabbing (Figure 2). Sizes can be set as a standard for easy sewing, such as sizes S, M, L and XL or may be customized according to the user's body size. Use of Teijin conex (Xfire) flame retardant fabrics that can prevent fire or splashes. And a ballistic vest is designed to be worn over the inside for the operation of conditions outside of war or general terrorism. Cotton fabric has lightweight properties. Easy to maintain, suitable for the climate in Thailand or Southeast Asia.

Figure 2 Sewing the body of ballistic vest.

Wear a ballistic plate with a waterproof shielded atrocity and stabbing protection plate inside. Both the front and rear ballistic vests then buttoned the shirt's front (Figure 3).

Figure 3 Ballistic vest for protective atrocity and stabbing.

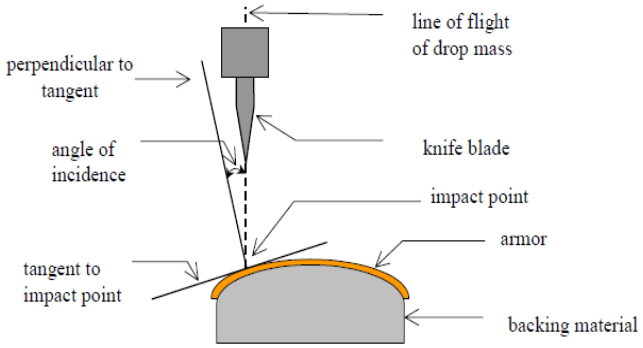

Figure 4 Atrocity and stabbing test kit.

Atrocity and stabbing test procedure

Tested for atrocity and stabbing according to HOSDB Body Armor Standards for UK Police (2007) (Figure 4) at least five times per sample [9, 10]. The test chamber has a temperature of 21 ± 6 °C (70 ± 10 °F) and a relative humidity of 50 ± 20%.

DOI: 10.60101/jarst.2023.254151

JOURNAL OF APPLIED RESEARCH ON SCIENCE AND TECHNOLOGY

Prepare a test plate on a support stand and set a distance of 25 ± 2 millimeters from the blade or pointed material. Then, determine the power level used in the test. Which is divided into three levels (Figure 5):

Level 1: The lowest energy value is 24 ± 0.50 joules, and the energy value above level 1 is 36 ± 0.60 joules.

Level 2: The lowest energy value is 33 ± 0.60 joules, and the energy value above level 1 is 55 ± 0.70 joules.

Level 3: The lowest energy value is 43 ± 0.60 joules, and the energy value above level 1 is 65 ± 0.80 joules.

Put four layers of sponge plate on top, the middle layer is 1 layer of foam plate, and the bottom layer is 2 layers of rubber plate. Then, test according to the required standards. The falling speed of the test blade was ± 0.05 m/s. (± 0.16 ft/s).

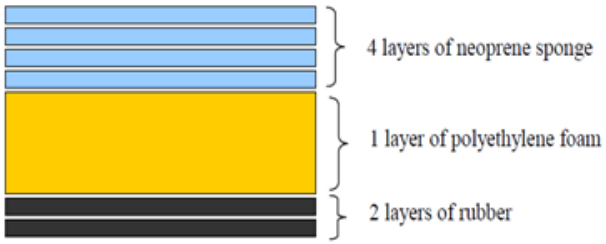

Figure 5 Test support plate.

Ballistic vest armor test procedure

Tested at level IIIA according to NIJ. STANDARD-0101.04 [11]. Utilize two types of ammunition in the test are 9 mm. FMJ, 124 grams. And 0.44 MAG SJHP, 240 grams, shown in table 2. Ensure that the laboratory shall be an enclosed (Figure 6), controlled environment, or protected field. Able to prevent hazards during standardized testing.

Table 2 Bullet type and speed.

Bullet	Speed
9 mm. FMJ (124 gr.)	1430 ± 30 ft/s (436 ± 9.1 m/s)
0.44 MAG SJHP (240 gr.)	1430 ± 30 ft/s (436 ± 9.1 m/s)

Figure 6 Laboratory.

Test processing equipment includes computer-processing bullets, guns, and ammunition velocity measurement devices.

Determine the point of fire on the ballistic vest. There are two types of test point determination, which are 6-point assignment and 12-point assignment, depending on each level of testing according to the NIJ. STANDARD-0101.04 standard (Figure 7) [12].

The test firing points of 6 points are divided into 4 test shots at an angle of 0 degrees, namely positions 1, 2, 3 and 6. In contrast, at an angle of 30 degrees, the number of 2 points is 4 and 5 at least 2 inches apart and at least 3 inches from the edge of the ballistic vest.

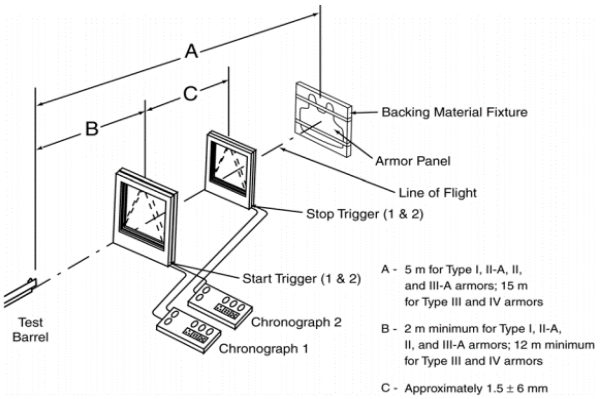

Figure 7 Placement of tools and testing equipment.

Test to determine the collapse distance of the backing material (Figure 8). Using a spherical steel pendulum released at a height of 2 meters 5 times freely, the values were taken five times to find the mean.

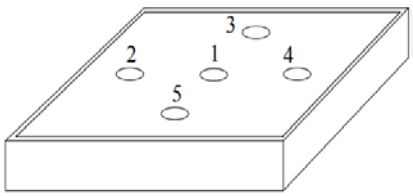

Figure 8 The position of the test steel pendulum.

Fire a test shot with a shotgun at the specified location. with different caliber projectiles at 0-degree angles and 30-degree angles (Figure 9).

Figure 9 Test setup.

DOI: 10.60101/jarst.2023.254151

Fire a test and check the bullet's penetrating effect. Measure the collapse distance of the backing material (Figure 10).

Figure 10 Determination of the collapse distance.

RESULTS AND DISCUSSIONS

According to research studies and tests according to the HOSDB Body Armor Standards for UK Police (2007) [13], the results are as follows:

Results test fabric properties

Test results of thickness weight and density of fabric according to table 3.

Results test atrocity and stabbing armor

Test results of atrocity and stabbing armor, which are divided into three types above, were tested in this armor plate test, 26 layers of plates with Endumax® Shield XF 33 + 2 layers of Twaron® SRM 509 were tested, and the results are shown in table 4 and table 5.

Results ballistic vest armor

The results of testing the properties of the fabric for ballistic vest protection were a atrocity and stabbing resistant armor plate containing 32 layers of Endumax® Shield XF 33 + 3 layers of Twaron® SRM 509, fire tested with 0.44 MAG SJHP, 240 grams ammunition, and an atrocity and stabbing resistant armor plate with 36 layers of Endumax® Shield XF 33 + 3 layers of Twaron® SRM 509. Fire tested with 9 mm. FMJ, 124 grams. ammunition. Test results are shown in table 5 and table 6.

Table 3 Test result of thickness weight and density fabric.

Fabric	**Twaron® SRM 509**			**Endumax® Shield XF 33**		
Item	Thickness (mm.)	Weight (g.)	Density (g.m^2)	Thickness (mm.)	Weight (g.)	Density (g.m^2)
1	0.44	1.98	198	0.22	1.46	146
2	0.45	2.00	200	0.23	1.45	145
3	0.44	1.99	199	0.22	1.45	145
4	0.44	2.00	200	0.21	1.45	145
5	0.45	1.99	199	0.22	1.44	144
6	0.44	2.00	200	0.22	1.45	145
7	0.45	1.99	199	0.22	1.46	146
8	0.44	1.99	199	0.23	1.44	144
9	0.44	2.01	201	0.22	1.45	145
10	0.44	1.98	198	0.21	1.46	146
Average	0.443	1.984	199.3	0.22	1.451	145.1
SD.	0.00483	0.03098	0.94868	0.00667	0.00738	0.73786
variance	0.00002	0.000098	0.90000	0.00004	0.00005	0.54444

Table 4 Test result of P1/B test at levels L2, E1 and L2, E2 with SP/B at levels L2, E1

NO.	**Sample Description**	**Blade (P1, S1, Spike)**	**Angle (deg.)**	**Desired Energy**	**Drop Height**			**Blade Mass (g)**	**HRC**	**Time (ms)**	**Velocity 1 (m/s)**	**Impact Energy (J)**	**Penet. (mm)**	**Footnotes**
				Level	**J**	**(ft.)**	**(in.)**							
1	GF-BV-RT-A220-01	P1/B	0	L2, E1	33	5	10	19.04	- 104	5.1463	6	33.11	0	
2	GF-BV-RT-A220-01	P1/B	0	L2, E1	33	5	10	18.92	- 125	5.1229	6	33.42	0	
3	GF-BV-RT-A220-01	P1/B	0	L2, E1	33	5	10	19.09	- 148	5.1415	6	33.18	0	
4	GF-BV-RT-A220-01	P1/B	0	L2, E1	33	5	10	19.06	- 145	5.1515	6	33.05	0	
5	GF-BV-RT-A220-01	P1/B	0	L2, E1	33	5	10	19.03	- 146	5.1458	6	33.12	0	
6	GF-BV-RT-A220-01	P1/B	0	L2, E2	50	8	11.5	19.08	- 136	4.1536	7	50.44	1	
7	GF-BV-RT-A220-01	P1/B	0	L2, E2	50	8	11.5	18.99	- 141	4.1448	7	50.65	1	
8	GF-BV-RT-A220-01	P1/B	0	L2, E2	50	8	11.5	18.95	- 104	4.1477	7	50.58	1	
9	GF-BV-RT-A220-01	P1/B	0	L2, E2	50	8	11.5	19.06	- 109	4.1524	7	50.47	0	
10	GF-BV-RT-A220-01	P1/B	0	L2, E2	50	8	11.5	19.08	- 117	4.1527	7	50.46	1	
11	GF-BV-RT-A220-01	SP/B	0	L2, E1	33	5	10	7.83	- 112	5.1495	6	33.04	0	

DOI: 10.60101/jarst.2023.254151

JOURNAL OF APPLIED RESEARCH ON SCIENCE AND TECHNOLOGY

NO.	Sample Description	Blade (P1, S1, Spike)	Angle (deg.)	Desired Energy	Drop Height		Blade Mass (g)	HRC	Time (ms)	Velocity 1 (m/s)	Impact Energy (J)	Penet. (mm)	Footnotes
				Level	J	(ft.) (in.)							
12	GF-BV-RT-A220-01	SP/B	0	L2, E1	33	5 10	7.92	- 103	5.1444	6	33.10	0	
13	GF-BV-RT-A220-01	SP/B	0	L2, E1	33	5 10	7.81	- 110	5.1618	6	32.88	0	
14	GF-BV-RT-A220-01	SP/B	0	L2, E1	33	5 10	7.85	- 124	5.1577	6	32.93	0	
15	GF-BV-RT-A220-01	SP/B	0	L2, E1	33	5 10	7.92	- 145	5.13	6	33.32	0	

Remarks:
1. Sabot Mass includes the average weight of dampers
2. Holder Mass includes the average weight of blades/spikes
3. Height is for reference only and may vary to meet energy requirements
4. D Time Base is the distance between velocity sensors
5. Standoff Distance is measured from blade tip to armor surface when drop mass is at 0 position (just breaking bottom velocity sensor beam)
6. Impact energy is estimated based on calculated energy and efficiency
7. For energy level E1, a max penetration of 7mm is allowed
8. For energy level E2, a max penetration of 20mm is allowed

Footnotes :
a = Excessive energy (above tol)
b = insufficient energy (below tol)
c = Too close (< 2 in) to armor edge
d = Too close (< 2 in) to backing matl edge
e = Too close (< 2 in) to prior impact
f = Reliable measurement not possible
g = impact on seam
h = Threat instrument bent
i = Threat instrument broke
j = Unfair double strike (bounce)
k = Other (See remarks)

Table 5 Test result of SP/B at level L2, E2

NO.	Sample Description	Blade (P1, S1, Spike)	Angle (deg.)	Desired Energy	Drop Height		Blade Mass (g)	HRC	Time (ms)	Velocity 1 (m/s)	Impact Energy (J)	Penet. (mm)	Footnotes
				Level	J	(ft.) (in.)							
1	GF-BV-RT-A220-01	SP/B	0	L2, E2	50	8 11.5	7.95	- 108	4.1807	7	49.73	3	
2	GF-BV-RT-A220-01	SP/B	0	L2, E2	50	8 11.5	7.83	- 114	4.1812	7	49.72	6	
3	GF-BV-RT-A220-01	SP/B	0	L2, E2	50	8 11.5	7.83	- 134	4.1752	7	49.86	8	
4	GF-BV-RT-A220-01	SP/B	0	L2, E2	50	8 11.5	7.89	- 148	4.1658	7	50.09	17	
5	GF-BV-RT-A220-01	SP/B	0	L2, E2	50	8 11.5	7.84	- 126	4.1666	7	50.07	4	

Remarks:
1. Sabot Mass includes the average weight of dampers
2. Holder Mass includes the average weight of blades/spikes
3. Height is for reference only and may vary to meet energy requirements
4. D Time Base is the distance between velocity sensors
5. Standoff Distance is measured from blade tip to armor surface when drop mass is at 0 position (just breaking bottom velocity sensor beam)
6. Impact energy is estimated based on calculated energy and efficiency
7. For energy level E1, a max penetration of 7mm is allowed
8. For energy level E2, a max penetration of 20mm is allowed

Footnotes :
a = Excessive energy (above tol)
b = insufficient energy (below tol)
c = Too close (< 2 in) to armor edge
d = Too close (< 2 in) to backing matl edge
e = Too close (< 2 in) to prior impact
f = Reliable measurement not possible
g = impact on seam
h = Threat instrument bent
i = Threat instrument broke
j = Unfair double strike (bounce)
k = Other (See remarks)

Table 6 Test result of firing with 0.44 MAG SJHP ammunition, 240 gr.

Shot No.	Ammo.	Time 1 (usec)	Velocity 1 (m/s)	Time 2 (usec)	Velocity 2 (m/s)	Avg.Vel. (m/s)	Penetration	Footnotes
1	1	3472	438.9	3467	439.6	439.3	None	DEF. 10mm
2	1	3485	437.3	3480	437.9	437.6	None	
3	1	3476	438.4	3485	437.3	437.9	None	DEF. 13mm
4	1	3489	436.8	3512	433.9	435.4	None	(a)
5	1	3478	438.2	3487	437.1	437.6	None	(a)
6	1	3487	437.1	3498	435.8	436.4	None	

REMARKS :
REQUIRED BLP: 436 m/s.

FOOTNOTES :
(a) SHOT IMPACTED AT A 30° ANGLE.

DOI: 10.60101/jarst.2023.254151

Table 7 Test result of firing with 9 mm. FMJ, 124 gr.

Shot No.	Ammo.	Time 1 (usec)	Velocity 1 (m/s)	Time 2 (usec)	Velocity 2 (m/s)	Avg.Vel. (m/s)	Penetration	Footnotes
1	1	3525	432.3	3534	431.2	431.8	None	DEF. 1mm
2	1	3553	428.9	3563	427.7	428.3	None	
3	1	3449	441.9	3459	440.6	441.2	None	DEF. 4mm
4	1	3451	441.6	3461	440.3	441.0	None	(a)
5	1	3422	445.4	3432	444.1	444.7	None	(a)
6	1	3473	438.8	3483	437.6	438.2	None	

REMARKS :
REQUIRED BLP: 436 m/s.

FOOTNOTES :
(a) SHOT IMPACTED AT A 30° ANGLE.

CONCLUSION

From the research results, the results can be summarized as follows:

The results of the 10-time Twaron® SRM 509 fabric thickness and weight tests. It can be concluded that both types of fabrics have good uniform weight and thickness for the production of cut and stab- resistant armor plates, including ammunition protection.

The result of the test result of the atrocity P1/B at L2, E1 5 times and at L2, E2 5 times, which is within the specified standard, is the blade depth of not more than 25 mm. This means that the fabric has the same standard to prevent cuts from weapons being sharp at a good level.

The results of the test of stabbing armor plate SP/B at level L2, E1 5 times and at level L2, E2 5 times are within the specified standard, i.e., the depth of the blade passing through the armor plate does not exceed 25 mm and that the fabric qualified for stabilization of pointed weapons at a reasonable level in both benchmarks.

The results of the atrocity and stabbing armor plates were tested with 0.44 MAG SJHP, 240 grams, and 9 mm. FMJ, 124 grams ammunition. It showed that the atrocity and stabbing armor plates tested with both types of ammunition showed good protection as standard.

In summary, the results of the research were the results of the fabric test in terms of thickness, weight, atrocity protection, stabbing protection, ammunition protection, power and capability of preventing atrocity and stabbing, and ammunition according to the objectives and assumptions set by the standards. The HOSDB Body Armor Standards for UK Police (2007) and the NIJ. STANDARD-0101.04 atrocity and stabbing protection tests are tested. By H.P. WHITE LABORATORY, INC., USA.

ACKNOWLEDGEMENT

This research was supported by Faculty of Textile Industry, Rajamangala University of Technology Krungthep (RMUTK) and Glofab Co., Ltd.

REFERENCE

1. Khojitmate S. Research and development of bulletproof vests. National Defense College. (NDC); 2011.
2. Khojitmate S. Research and manufacture of lightweight bulletproof vests, class III (NIJ). Defense Science and Technology Department. (DSTD); 2017.
3. Chailak C. A Study of the Influence of Compressive Strength on Nylon Woven Fabrics on Bullet Penetration. Rajamangala University of Technology Thanyaburi. (RMUTT); 2009.
4. Ankaew S. Feasibility study of bonding nylon 66 fibers by compression process as a bulletproof component in automobiles. Rajamangala University of Technology Thanyaburi. (RMUTT); 2008.
5. Putsri C. A Study of the Properties of Woven Fabrics on the Penetration of Bullets. Rajamangala University of Technology Thanyaburi. (RMUTT); 2011.
6. Siripokanan T. Development of bulletproof vest using aluminum 5083. Rajamangala University of Technology Lanna. (RMUTL); 2011.
7. Rajchit S. A study of the properties of AISI 316l stainless steel bulletproof vest. Rajamangala University of Technology Lanna. (RMUTL); 2014.
8. Gresczcuk LB. Response of Isotropic and Composite Materials to Particle Impact, Foreign Object Impact Damage to Composites, ASTM STP 568: American Society for Testing and Materials; 1975.
9. Croft J, Longhurst D. HOSDB Body Armour Standards for UK Police. Part 1: General Requirements. Publication No. 39/07/A: Scientific Development Branch; 2007.
10. Croft J, Longhurst D. HOSDB Body Armour Standards for UK Police. Part 2: Ballistic Resistance.

DOI: 10.60101/jarst.2023.254151

JOURNAL OF APPLIED RESEARCH ON SCIENCE AND TECHNOLOGY

Publication No. 39/07/B: Scientific Development Branch; 2007.

11. National Institute of Justice. NIJ Standard 0101.04, Ballistic Resistance of Personal Body Armor: U.S. Department of Justice; 2000.
12. National Institute of Justice. NIJ Standard 0101.06, Ballistic Resistance of Body Armor: U.S. Department of Justice; 2008.
13. National Institute of Justice. NIJ Standard 0108.04, Ballistic Resistance of Protective Materials: U.S. Department of Justice; 2003.

DOI: 10.60101/jarst.2023.254151

Received: October 24, 2023 | Revised: November 27, 2023 | Accepted: November 28, 2023

JOURNAL OF APPLIED RESEARCH ON SCIENCE AND TECHNOLOGY
JARST
INSTITUTE OF RESEARCH AND DEVELOPMENT
RAJAMANGALA UNIVERSITY OF TECHNOLOGY THANYABURI
ISSN ONLINE: 2773-9473
https://ph01.tci-thaijo.org/index.php/rmutt-journal

2-Keto-gluconate production and purification by thermotolerant acetic acid bacterium *Nguyenibacter vanlangensis* KKS-R1

Phongsupha Chanthachaiyaphum[1], Somporn Moonmangmee[2] and Duangtip Moonmangmee[1*]

[1]Department of Microbiology, Faculty of Science, King Mongkut's University of Technology Thonburi, Bangkok 10140, THAILAND
[2]Biodiversity Research Center, Thailand Institute of Scientific and Technological Research, Pathumthani 12120, THAILAND
[*]Corresponding author: duangtip.moo@kmutt.ac.th

ABSTRACT

2-Keto-gluconic acid (2-KGA) is a pivotal intermediate in the production process of ascorbic acid, commonly known as vitamin C. The bacterium *Nguyenibacter vanlangensis* KKS-R1 is an acetic acid bacterium (AAB) that has been selectively screened for its ability to produce 2-KGA among twenty-five bacterial isolates at high temperatures up to 40°C. This thermotolerant property makes it advantageous for various industries. Therefore, it has garnered interest for its potential application in the production of 2-KGA and purification of the 2-KGA product. This study evaluated the production of 2-KGA by N. vanlangensis KKS-R1 using 1% gluconate as the substrate. The 2-KGA was determined by thin-layer chromatography, Lanning and Cohen's method, and high-performance liquid chromatography. After fermentation in a minimal liquid medium for 24 hours, the bacterium showcased its prowess by producing 2-KGA concentrations of 7.5 g/L. However, the purity of the 2-KGA production is paramount for industrial applications. In addressing this, a rigorous chromatographic purification regimen was employed. This involved two sequential stages of ion exchange chromatography, DEAE-Sephacel and DOWEX 1X4, followed by Superdex™ S-200 column chromatography. The collective efficacy of these methodologies yielded a product with an impressive purity index of 71.02%. The 2-KGA product was then subjected to a decolorization process using activated carbon and freeze-dried. This results in the compound being a pure white powder. This investigation indicates that *N. vanlangensis* KKS-R1 shows good potential as a 2-KGA producer at high temperatures. Under proper purification techniques. These findings contribute to developing purified processes and producing 2-KGA for industrial efficiency.

Keywords: Acetic acid bacteria (AAB), Thermotolerant, 2-Ketogluconate (2-KGA), Column chromatography

INTRODUCTION

Acetic acid bacteria (AAB) are gram-negative bacteria characterized by their ellipsoidal or rod-shaped cells. They are aerobic bacteria, requiring oxygen for growth [1]. Depending on the genus, their flagella may be peritrichous or polar. Acetic acid bacteria belong to the family Acetobacteraceae within the class Alphaproteobacteria. Originally, this classification comprised two genera: *Acetobacter* and *Gluconobacter*. However, with advancements in genetic molecular techniques, which have significantly improved the classification process, 19 distinct genera of acetic acid bacteria have been identified: *Acetobacter*, *Acidomonas, Ameyamaea, Asaia, Bombella, Commensalibacter, Endobacter, Gluconacetobacter, Gluconobacter, Granulibacter, Komagataeibacter, Kozakia, Neoasaia, Neokomagataea, Nguyenibacter, Saccharibacter, Swaminathania, Swingsia,* and *Tanticharoenia* [2]. Mesophilic strains thrive optimally at temperatures between 25-30°C, while thermotolerant strains can grow in the broader temperature range, with their optimal metabolic activity occurring at 37-40°C. The optimal pH for growth is between 5.0-6.5, but these bacteria can also grow at slightly lower pH values [3, 4]. Acetic acid bacteria possess a mechanism to oxidize starting substances like alcohols, sugars, sugar alcohols, and sugar acids in an "oxidative fermentation" process. En enzymes on the cell membrane's outer surface facing the periplasm oxidize these substrates. The oxidation products are expelled outside the cell and accumulate in the culture medium [5, 6]. These properties make AAB suitable for producing various products since it allows for easy separation of the product from the bacterial cells, rapid fermentation processes, and high yields. 2-Ketogluconate (2-KGA) is an essential organic acid used in producing erythorbic acid, also known as D-isoascorbic acid. It's a stereoisomer of ascorbic acid (vitamin C) and is widely used as an antioxidant in food processing, adhering to Good Manufacturing Practice (GMP) standards. It plays a crucial role in preventing food oxidation, retaining the color, taste, and aroma of foods, and inhibiting the

DOI: 10.60101/jarst.2023.254506

JOURNAL OF APPLIED RESEARCH ON SCIENCE AND TECHNOLOGY

formation of carcinogenic ammonium nitrite during food processing [7-9]. In addition, it has been certified as a Generally Recognized As Safe (GRAS) compound by the U.S. Food and Drug Administration (FDA). The synthesis of 2-KGA is achieved using microorganisms through the oxidative fermentation process of D-glucose sugar. This occurs in the periplasmic space, anchoring related enzymes to the cell membrane's outer surface. The D-glucose is oxidized into D-glucono-δ-lactone, which can then be converted into D-gluconic acid. This transformation might be due to the instability of the molecule or possibly be catalyzed by the enzyme gluconolactonase [10]. Subsequently, D-gluconic acid is further oxidized by enzymes on the cell membrane, specifically by the enzyme D-gluconate dehydrogenase [11, 12], which has a cofactor known as flavin adenine dinucleotide, referred to as FAD-GADH, and the enzyme glycerol dehydrogenase [13], which has a cofactor known as PQQ and is referred to as PQQ-GLDH. FAD-GADH catalyzes the reaction to produce 2-KGA, while PQQ-GLDH catalyzes the reaction to produce 5-keto-D-gluconic acid (5KGA). Both reactions occur competitively. Either 2-KGA or 5-KGA is excreted outside the cell until the glucose is completely oxidized. However, in some strains, it has been observed that 2-KGA is further oxidized to 2,5-diketo-D-gluconic acid (2,5 DKGA) by the enzyme 2-KGA dehydrogenase. This enzyme is membrane-bound and has FAD as its cofactor [14]. Almost all industrial-scale production of 2-KGA is achieved through microbial fermentation, as chemical and enzymatic methods yield low volumetric productivity, and the catalysts or enzymes are expensive. Moreover, the products from the oxidative fermentation process of acetic acid bacteria can be utilized without cell lysis, which involves separating the cells and subsequently purifying the desired compounds using various methods based on their chemical and physical properties. Consequently, researchers have been selecting strains of acetic acid bacteria capable of producing 2-KGA at elevated temperatures and studying the purification process of 2-KGA at the laboratory scale, aiming for further development at an industrial scale.

MATERIALS AND METHODS

Microorganisms

The 25 tested strains are bacteria obtained by isolating the roots of rice plants. It can fix nitrogen and effectively dissolve phosphorus and zinc, identified using 16S rRNA gene sequence analysis [15] (Table 1).

Table 1 Bacterial isolates were identified using 16S rRNA gene sequence analysis [15] for screening of 2-KGA production.

Code Isolate	Isolate gene similarity in NCBI database	% of identify	Code Isolate	Isolate gene similarity in NCBI database	% of identify
TBRC4639	*N. vanlangensis* TBRC4639 ^{T}	100.00	TBRC 479	*G. azotrocaptans* TBRC 479 ^{T}	100.00
KKS-R4	*N. vanlangensis* TN01LGI	100.00	AR-R1	*G. diazotrophicus* LMG 7603	99.96
KKS-RZ1	*N. vanlangensis* TN01LGI	96.67	PS-RZ1	*A. methanolica* NBRC 104435	99.92
NKS-RZ1	*N. vanlangensis* TN01LGI	99.57	AR-R2	*A. methanolica* NBRC 104435	96.51
AR-R3	*N. vanlangensis* TN01LGI	99.86	NKS-R1	*A. methanolica* NBRC 104435	99.92
KKS-R1	*N. vanlangensis* TN01LGI	99.85	NKS-RZ4	*A. methanolica* NBRC 104435	100.00
NKS-RZ3	*N. vanlangensis* TN01LGI	99.85	PS-RZ2	*A. methanolica* NBRC 104435	99.92
AR-RZ1	*N. vanlangensis* TN01LGI	99.93	KKS-RZ2	*A. methanolica* NBRC 104435	99.92
KKS-RZ4	*N. vanlangensis* TN01LGI	99.92	TBRC 15	*A. nitrogenifigens* TBRC 15 ^{T}	100.00
KKS-R3	*N. vanlangensis* TN01LGI	100.00	146AE	*B. cepacian* ATCC 25416	*
KKS-RZ3	*N. vanlangensis* TN01LGI	99.78	KKS-S1	*B. cepacian* ATCC 25416	98.91
TBRC 478	*G. sacchari* TBRC 478 ^{T}	100.00	KKS-R2	*B. cepacian* ATCC 25416	99.65
TBRC 480	*G. johannae* TBRC 480 ^{T}	100.00			

*: no identify by 16S rRNA
^{T}: Type strain

Primary screening

The cultures were grown in a Glucose-Yeast Extract-Peptone (GYP) medium (2% glucose (w/v), 1% peptone (w/v), 0.5% yeast extract (w/v). They were incubated at 30°C with shaking at 200 rpm for 24 h. Afterward, the concentration of the cultures was adjusted to 1 McFarland standard (Densitometer Densimat 99234, BIOMERIEUX ITALIA S.P.A., Italy), then they were grown again in the GYP medium, incubated at 30°C with shaking at 200 rpm for another 24 hours. Following this, the reactions were centrifuged

DOI: 10.60101/jarst.2023.254506

at 8,000 rpm for 5 min. The clear portion (supernatant) was then analyzed using Thin Layer Chromatography (TLC).

Selection of thermotolerant AAB for 2-KGA production

The test strains were cultured in a liquid minimal medium using 1% sodium gluconate (w/v) as a substrate and were incubated at temperatures of 30 °C, 37 °C, and 40°C, shaking at 200 rpm for 24 hours. At the end of the incubation period, the cells were harvested by centrifugation at 8,000 rpm for 15 minutes. The quantity of fermentation products the acetic acid bacteria produced.

2-KGA production

The selected acetic bacteria are cultivated with sodium gluconate in a liquid minimal medium. This is because of the metabolic pathway that can directly lead to the production of 2-KGA. An initial concentration of 1% sodium gluconate (w/v) is used, and the fermentation is performed at a temperature of 40°C with agitation at 200 rpm for 24 hours., scaled up to a volume of 1 L. After fermentation, the reaction mixture is centrifuged at 8,000 rpm for 5 minutes, and the supernatant is collected for further analysis.

Determinations of 2-KGA

1. Thin layer chromatography (TLC)

The culture supernatant was spotted onto a TLC plate (Silica gel 60, Merck Co., Germany) with a volume of 10 µL of sample. The standard solutions of 2-KGA, 5-KGA, and glucose were compared. The plate was then immersed in a solvent system composed of ethyl acetate, acetic acid: methanol: distilled water in the ratios 6 : 1.5 : 1.5 : 1, respectively. After allowing it to dry, the plate was sprayed with a TTC solution (2% 2,3,5-triphenyl tetrazolium chloride (w/v) in a 0.5 M potassium hydroxide solution) or a freshly prepared color-developing reagent of aniline-diphenylamine phosphoric acid reagent (2% aniline (v/v), 2% diphenylamine (w/v) and 15% phosphoric acid (v/v) in acetone). The plate was then baked at a temperature of 120°C for 10-20 minutes. The intensity of the colors was compared with the standard solutions afterward.

2. Lanning and Cohen's method [16]

The product quantity was analyzed using Lanning and Cohen's method, which employs the o-Phenylenediamine dihydrochloride reagent (1.5% o-Phenylenediamine dihydrochloride (w/v) in 0.375 N HCl). When o-Phenylenediamine dihydrochloride reacts with 2-keto acids, it forms 2-hydroxyquinoxalines, forming a reddish-brown to green color. Subsequently, the absorbance was measured at 330 nm.

3. High-Performance Liquid Chromatography (HPLC)

Analysis was conducted to confirm the experimental results using HPLC with the HPLC Water e2695 Separations Module (Water Corporation 2013, USA). An Aminex® HPX-87H column, 300 mm x 7.8 mm (I.D. x Length), Bio-Rad) was utilized, and 5.0 mM Sulfuric Acid (H_2SO_4) was used as the mobile phase at a flow rate of 0.60 mL/min. The column temperature was maintained at 65°C. Detection was carried out using a Water 2998 Photodiode Array (PDA) Detector set at a wavelength of 210 nm. Results were interpreted by comparing them with the standard compounds of 2-KGA under the instrument conditions presented in Table 2.

Table 2 Analysis conditions for 2-KGA by HPLC.

Parameter	Optimized condition
Chromatograph:	HPLC Waters e2695 Separations Module
Column:	Aminex® HPX-87H (Bio-Rad)
Column Size:	300 mm x 7.8 mm (I.D. x Length)
Mobile phase:	5.0 mM Sulfuric Acid (H_2SO_4)
Flow rate:	0.60 mL /min
Detector:	Water 2998 Photodiode Array (PDA); 210nm
Column temp.:	65°C
Injection volume:	10 µL

Purification of 2-KGA via column chromatography

1. Ion-Exchange Chromatography

DEAE-Sephacel column chromatography: The 2-KGA obtained from acetic bacteria was purified using modified methods [17]. The initial step involves passing the sample through DEAE Sephacel column chromatography to eliminate undesired proteins and other impurities. The DEAE Sephacel gel was first activated for effective chromatography. This involved thoroughly rinseing with copious amounts of distilled water to remove 20% ethanol. Subsequently, the gel was immersed in 0.1 N NaOH for 30 minutes and then rinsed with large volumes of water until a neutral pH (7.0) was achieved. The gel was soaked in 0.1 N HCl for another 30 minutes and rinsed extensively to reach a neutral pH. Once ready, the gel was packed into a chromatography column. The column was then equilibrated by introducing twice the gel volume of 25 mM Tris-HCl (pH 8.0). The eluent was allowed to pass through the column until a pH of 8.0 was consistent in the effluent. The column was then connected to a fraction collector to separate the compounds. With a set flow rate of 1 mL/min, fractions were collected every 10 mL. A 450 mL sample was introduced into the column and washed with 2 column volumes of 25 mM Tris-HCl (pH 8.0). Once the entire sample had passed through the column, elution was carried out using 1 M NaCl, at three times the column volume. The protein profile of each fraction was monitored by measuring its absorbance at 280 nm, and compared against spots on filter paper sprayed with TTC. Fractions containing 2-KGA were pooled together and analyzed for the cumulative content of 2-KGA and proteins using Lanning

DOI: 10.60101/jarst.2023.254506

JOURNAL OF APPLIED RESEARCH ON SCIENCE AND TECHNOLOGY

and Cohen's method [16] and Lowry's method [18], respectively.

DOWEX 1X4 column chromatography: The sample from section DEAE-Sephacel column underwent further purification through DOWEX 1X4 column chromatography. The DOWEX 1X4 column was initially activated by neutralizing it with 0.1 N NaOH, followed by extensive washing with water until a neutral pH (7.0) was achieved. The gel was then equilibrated to the chloride form using 1 M $CaCl_2$. Subsequent steps involved the removal of Ca^{2+} ions by rinsing with copious amounts of water until no precipitation occurred upon adding the eluent to 0.5 M sodium bicarbonate. The gel was then packed into a chromatography column.100 mL of sample volume was loaded onto the column, followed by a wash with DI water at twice the volume of the column. After allowing all compounds to pass through the column, elution was conducted using 0.8 M and 1.0 M NaCl solutions at three times the column volume. Each fraction was monitored by spotting on filter paper and spraying with TTC, and further compared against reactions with o-Phenylenediamine dihydrochloride reagent [16]. Absorbance measurements were taken at a wavelength of 330 nm. Fractions containing 2-KGA were pooled together and subsequently analyzed for the total content of 2-KGA and proteins using Lanning and Cohen's [16] and Lowry's [18], respectively.

2. Gel Filtration Chromatography

Concentration of 2-KGA Solution: The clear fraction of the culture supernatant that has passed through the DOWEX 1X4 column was concentrated using rotary evaporation under conditions of low pressure at 35 mbar, a rotation speed of 50 rpm, and a temperature of 40°C until the sample volume was reduced tenfold (10x concentration).

Superdex™ S-200 Column Chromatography: The Superdex™ S-200 gel, which was stored in a 20% ethanol solution, was decanted. The gel was then washed with distilled water, stirred to ensure homogeneity, and allowed to settle. The clear supernatant was discarded. This washing procedure was repeated 2-3 times. The gel was then packed into an XK column (XK 16/100; I.D./Length, mm) following the instructions provided for Superdex™ S-200. The gel in the column was equilibrated with a 0.1 N NaCl solution at a flow rate of 60 mL per hour for 3 hours.

Loading sample: The concentrated 2-KGA solution, 0.5 mL, was loaded onto the Superdex™ S-200 column chromatography (as described in 2.) at a flow rate of 60 mL/h. This was followed by elution with a 0.1 N NaCl solution, collecting 1.5 mL/fractions. Each fraction's profile was monitored by spotting onto filter paper, spraying with TTC, and reacting with o-Phenylenediamine dihydrochloride before measuring the absorbance at a wavelength of 330 nm. Subsequently, fractions containing 2-KGA were pooled together to analyze 2-KGA and total protein using Lanning and Cohen's [16] and Lowry's [18]. The absorbance values were then measured at 330 and 490 nm wavelengths, respectively.

Color removal and precipitate removal

At a concentration of 1% (w/v), activated carbon powder was utilized to absorb the color from the 2-KGA product. The mixture was left undisturbed for at least 4 hours. to allow the charcoal powder to adsorb the color fully. Afterward, it was centrifuged to separate the charcoal powder sediment. The concentration of the product post-color adsorption was determined using Lanning and Cohen's method [16]. Subsequently, the sample was stored at a temperature of -80°C before being lyophilized with a freeze-dryer.

Total protein quantification [18]

The sample solution, with a volume of 0.4 mL, was added to a test tube. Lowry's solution A and Lowry's solution B were mixed in a ratio of 50 : 1 (A : B), and 2 mL of this mixture was added to the test tube. The contents were mixed thoroughly, and then incubated at 35°C for 10 min. Subsequently, 0.2 mL of 1 N Folin's reagent was added. Immediate mixing was done using a vortex mixer and then incubated at 35°C for 30 minutes. The absorbance of the solution was measured at 750 nm, and the results were compared against a BSA standard curve to determine the protein concentration in the sample.

RESULTS AND DISCUSSIONS

Primary screening of 2-KGA producer

The TLC technique was used to analyze the type of 2-KGA product derived from the 24-hour fermentation of 25 bacterial strains listed in Table 1. The experimental results revealed: 13 isolates, specifically AR-R2, TBRC478, TBRC479, NKS-RZ1, AR-R3, KKS-R1, TBRC480, NKS-RZ2, AR-RZ1, KKS-RZ4, TBRC4639, KKS-R3, and KKS-RZ3, could produce 2-KGA. This was evident as red spots emerged at positions consistent with the standard 2-KGA sugar solution on the culture medium. The isolated TBRC15 produced 5-KGA, indicated by the presence of an orange-red spot on the TLC plate that matched the position of the 5-KGA standard solution. Conversely, the substances produced by the isolates PS-RZ1, KKS-R4, KKS-RZ1, NKS-R1, NKS-RZ3, PS-RZ2, KKS-S1, 146AE, KKS-R2, KKS-RZ2, and AR-R1 in the culture medium were not the desired keto-sugars. They were found to be glucose, an aldose sugar group that did not produce a red spot when treated with TTC, as shown in Figure 1B. When sprayed with the color-developing reagent, aniline-diphenylamine phosphoric acid reagent, however, blue spots corresponding to the standard glucose solution appeared, alongside greenish-brown spots matching the 2-KGA standard and gray spots aligning with the 5-KGA standard, as shown in Figure 1A. When utilizing glucose, acetic acid bacteria's

DOI: 10.60101/jarst.2023.254506

metabolic pathway involves the oxidation of D-glucose into D-gluconic acid. Subsequently, D-gluconic acid can be converted into either 2-KGA or 5-KGA through competitive reactions. Both 2-KGA and 5-KGA are then secreted out of the cell until the glucose is fully oxidized. Interestingly, certain strains of *Gluconobacter* are found to further oxidize 2-KGA into 2,5-DKGA via the enzyme 2-KGA dehydrogenase. This enzyme is membrane-bound and employs FAD as a cofactor [14]. Therefore, the results indicate that the isolates AR-R2, TBRC478, TBRC479, NKS-RZ1, AR-R3, KKS-R1, TBRC480, NKS-RZ2, AR-RZ1, KKS-RZ4, TBRC4639, KKS-R3, and KKS-RZ3 are of particular interest for further investigation into their ability to produce 2-KGA. These selected isolates were chosen for subsequent studies.

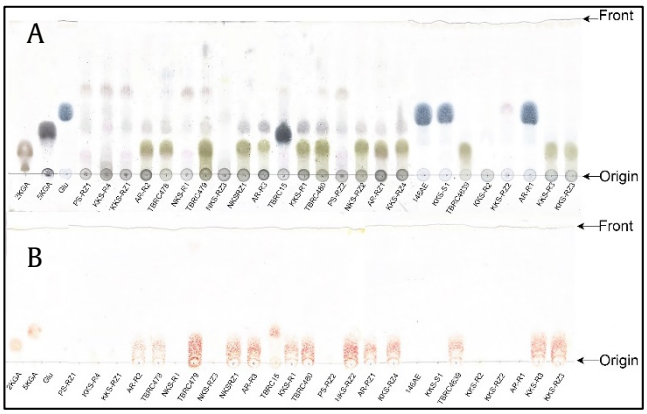

Figure 1 The oxidative products of 25bacterial strains after culture in 1% glucose (w/v) medium and detection by TLC technique using (A) aniline-diphenylamine phosphoric acid reagent and (B) TTC reagent.

Selection of thermotolerant AAB for 2-KGA production

Upon testing the growth of the 13 strains that could produce 2-KGA from the previous experiments, they were cultivated in a minimal liquid medium at temperatures of 30, 37, and 40°C to select strains that could grow at higher temperatures. The results showed that increasing temperatures had varying effects on the growth of the test organisms. All 13 isolates were found to grow well at 30°C. However, at 37°C, only 7 isolates, namely AR-R2, TBRC478, AR-R3, KKS-R1, AR-RZ1, KKS-R3, and KKS-RZ3, were able to grow effectively. Furthermore, at 40°C, only the isolates AR-R2, AR-R3, KKS-R1, AR-RZ1, KKS-R3, and KKS-RZ3 were found to grow in sequence. When analyzing the quantity of 2-KGA products using the chemical method by Lanning and Cohen [16]. The results revealed that at 30°C, all 13 isolates could produce 2-KGA. Among them, isolated TBRC479 displayed the highest production capacity, followed in order by isolates KKS-RZ3, AR-RZ1, KKS-R1, KKS-RZ3, NKS-RZ2, AR-R2, AR-R3, TBRC480, TBRC478, TBRC4639, KKS-RZ4, and NKS-RZ1. At 37°C, only the isolates KKS-R1, AR-RZ1, TBRC4639, AR-R3, AR-R2, KKS-R3, KKS-RZ3, TBRC478, and NKS-RZ2 were found to produce 2- KGA in that order. Meanwhile, at 40°C, only the isolates KKS-R1, AR-RZ1, AR-R3, KKS-RZ3, and AR-R2 showed 2-KGA production capabilities, with KKS-R 1distinctly showing robust consistency across all three tested temperatures, as represented in Figure 2. This evidence indicates that this group of AAB is thermotolerant. Typically, an increase in temperature can influence the enzymatic activity pivotal for converting substrates into products and impair the metabolic pathways of the microorganisms. Mesophilic acetic acid bacteria tend to thrive best between 25-30°C. In contrast, thermophilic strains can maintain good growth and metabolic activity at elevated temperatures, largely because the enzymes in these heat-resistant microorganisms naturally possess inherent thermostability [19]. Therefore, there has been an effort to select strains of AAB that can thrive at elevated temperatures, aiming to maximize utility while minimizing temperature-related limitations. This allows for broader applications in various industries that operate at higher temperatures. Consequently, the researcher is keen on further exploiting the *N. vanlangensis* KKS-R1 strain for enhanced 2-KGA production because it is most stable in production at higher temperature ranges.

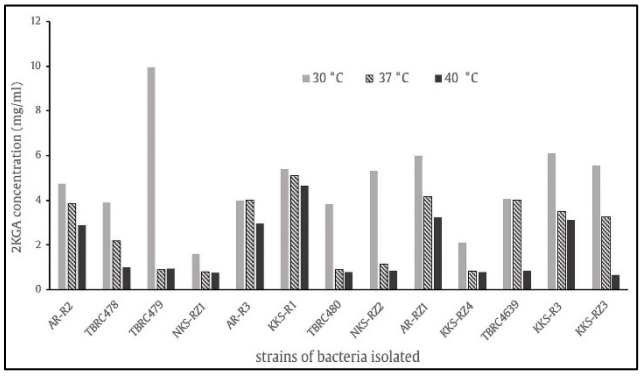

Figure 2 Production of 2-KGA from thirteen selection bacterial strains at 30, 37, and 40°C.

2-KGA production

From the experiment of producing 2-KGA using the *N. vanlangensis* KKS-R1 strain in a minimal liquid medium, with 1% gluconate (w/v) serving as the carbon source in a 1 L volume, and under shaking conditions at a rate of 200 rpm at a cultivation temperature of 37°C for 1 day, the total production amounted to 7.476 g/L.

Purification of 2-KGA

The culture supernatant (crude 2-KGA) was subjected to DEAE Sephacel column chromatography, characterized by its anionic properties. Each fraction was monitored by measuring the absorbance at a wavelength of 280 nm, a standard method for quantifying general protein levels. The results revealed two distinct peaks: peak 1 was located within the fraction range of 22-110, while peak 2 was identified in the fraction

DOI: 10.60101/jarst.2023.254506

JOURNAL OF APPLIED RESEARCH ON SCIENCE AND TECHNOLOGY

range of 111-142, as illustrated in Figure 3. These outcomes aligned with tracking via TTC, indicating the emergence of red spots solely within peak 1, fraction 22-100 (pool I), as demonstrated in (•). Conversely, peak 2, fraction 102-142 (pool II), showed an absence of these red spots. The fractions (pool I) with these evident red spots were then pooled together before undergoing 2-KGA quantification analysis using Lanning and Cohen's method [16]. Compared to the sample before column chromatography, the total 2-KGA yield was found to be 3.40±0.01 g, while the quantity prior to column passage was 3.74±0.04 g. Moreover, when the total protein quantity both before and after column passage was analyzed using Lowry's method [18], it was observed that pool I contained only 0.38±0.46 g of protein. This starkly contrasts the total protein measured before column chromatography, which was as high as 0.94±0.63 g. Some of the protein content was lost, with a significant 90.96 % of the desired compound eluted from the DEAE Sephacel column, as depicted in Table 3. This suggests that some proteins carrying positive charges were retained by the DEAE Sephacel column chromatography, which possesses anionic properties. These proteins were only eluted when washed with 1 M NaCl. In this phase, some of the proteins were separated, resulting in a purer desired compound.

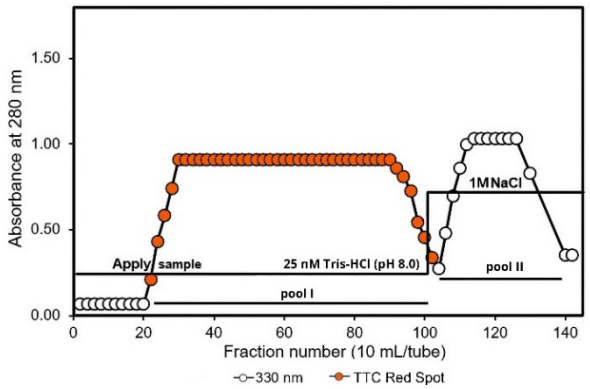

Figure 3 Chromatography of 2-KGA of *N. vanlangensis* KKS-R1 on DEAE Sephacel column. Culture supernatant was applied onto a DEAE Sephacel column previously equilibrated with 25 mM Tris-HCl buffer (pH 8.0). The elution of 2-KGA was made by 25 mM Tris-HCl buffer (pH 8.0) and eluted with 1 M NaCl.

After 2-KGA fractions from DEAE Sephacel column chromatography were pooled, they were loaded onto a DOWEX 1X4 column and adjusted to their chloride form, which binds to positively charged compounds. Tracking the 2-KGA profile by spotting on filter paper and spraying with TTC reagent showed slight red spots in fractions 12-26 (pool I) during the sample loading and wash phases (fractions 1-58), as red spots indicated (•). As the elution phase (fractions 59-98) using 8.0 M NaCl three times the volume began, red spots appeared from fractions 60-96 (pool II) as red spots indicated (•), with no color observed in other fractions. Pooling and analyzing these fractions showed peaks consistent with the TTC test results. The wash phase peak might arise from neutrally charged compounds having weak column binding, resulting in some desired compound release after water wash. All compounds were completely eluted during the elution step, presenting as the second peak, with no substances observed post-elution with 1 M NaCl, as depicted in Figure 4. Upon analyzing the total 2-KGA quantity in comparison to pre-DOWEX 1X4 column values, the post-column product amounted to 3.40±0.01 g, and the pre-column content was 3.74±0.04 g. This signifies that purification using the DOWEX 1X4 column post. protein separation via DEAE Sephacel column chromatography improved purity, yielding up to 75% of the desired compound. However, protein analysis revealed a residual protein content of 0.06±0.002 mg/mL in the product, as shown in Table 3. Consequently, this product would undergo further purification stages.

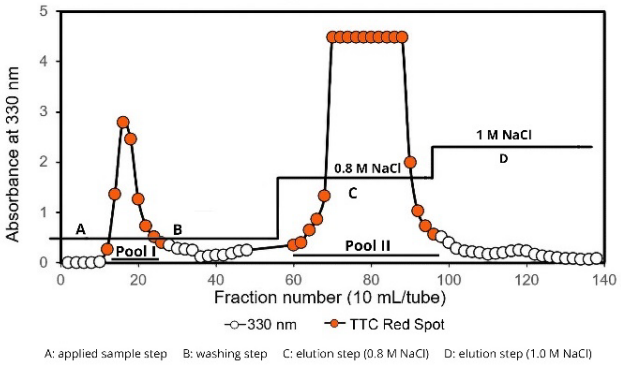

Figure 4 Elution profile of 2-KGA from pooled I of DEAE Sephacel column applied onto DOWEX 1X4 column chromatography previously equilibrated with 1 M $CaCl_2$ under the conditions described in Materials and Methods. Elution was done with a stepwise of 0.8 M NaCl and 1 M NaCl as indicated. (A: applied sample step, B: washing step, C: elution step (0.8 M NaCl) and D: elution step (1.0 M NaCl)).

The 2-KGA sample (pool II), primarily obtained from purification via the DOWEX 1X4 column, was purified using the Superdex™ S-200 column chromatography. The profile of the eluted components was monitored using Lanning and Cohen's method [16]. Experimental results showed that the profile of substances eluted from the column had only one peak, spanning fractions 94 to 108 (pool I). This result correlates with the TTC test, where red spot appeared, as indicated in (•). Furthermore, when monitoring the protein content in each fraction by measuring the absorbance at a wavelength of 280 nm, a protein peak was observed in fractions 18 to 86. No peaks were evident in fractions 94 to 108, suggesting that the Superdex™ S-200 column chromatography effectively eliminated the proteins. Consequently, when pooling the fractions from 94 to

DOI: 10.60101/jarst.2023.254506

108, the overall yield of 2-KGA was determined to be 2.654 g, resulting in a yield of 71.02%. Meanwhile, Lowry's method reduced the overall protein concentration to undetectable levels [18] (Table 3).

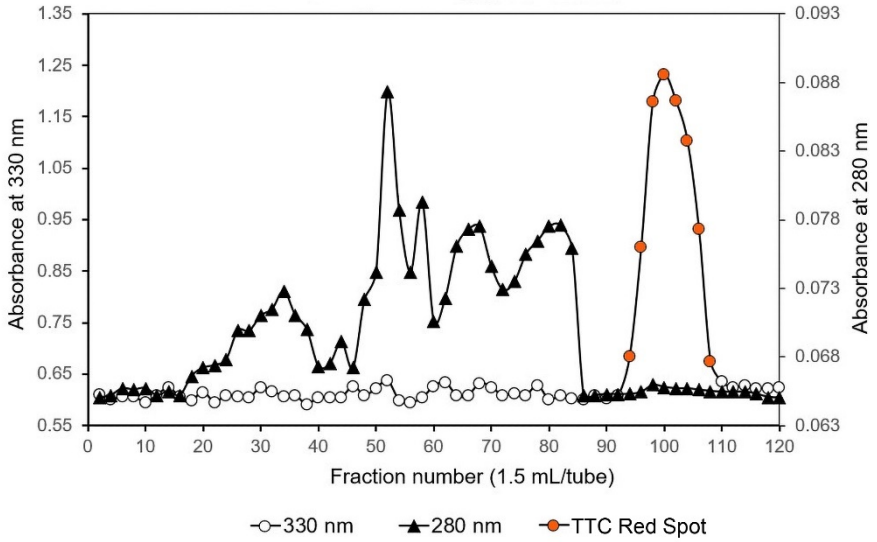

Figure 5 Gel filtration profile of 2-KGA from *N. vanlangensis* KKS-R1. The 2-KGA was obtained from pooled II of DOWEX 1X4 column chromatography was loaded onto Superdex™ column chromatography (Ø1.6 cm x 90 cm) equilibrated with 0.1 N NaCl and eluted at a flow rate of 22 mL/h. Absorbance is at 330 nm (open circles) and 280 nm (closed triangles).

Table 3 Purification summary of 2-KGA from *N. vanlangensis* KKS-R1.

Step of Purification	Total Volume (mL)	2-KGA Content (mg/mL)	Total 2-KGA (g)	Protein content (mg/mL)	Total Protein (g)	%yield of 2-KGA
Crude 2-KGA	500.00	7.47±0.04	3.74±0.04	1.88± 0.07	0.94± 0.63	100.00
DEAE Sephacel	630.00	5.40±0.01	3.40±0.01	0.60±0.01	0.38±0.46	90.96
DOWEX 1X4 (Pool I)	62.00	0.27±0.01	0.17±0.04	0.08±0.002	0.01±0.004	4.90
DOWEX 1X4 (Pool II)	350.00	8.08±0.02	2.96±0.33	0.06±0.002	0.02±0.73	75.00
Superdex S-200	35.00	75.84±0.016	2.654±0.18	ND*	ND*	71.02

*ND: Not detected

Figure 6 The Characteristics of 2-KGA powder after activated carbon adsorption and crystallization by freeze-drying.

Decolorization and precipitation

The decolorization of the 2-KGA product obtained from the experiment was performed using activated charcoal, known for its decolorizing properties. The mechanism behind this decolorization process involves weakly binding through van der Waals forces between organic compounds and the external surface of the charcoal [20]. When the charcoal was added to the pale yellow 2-KGA solution and allowed to settle for 4 hours, the solution's color became clearer. Before undergoing freeze-drying, the decolorized solution turned into a white powder, as shown in Figure 6.

Analysis of purity of the 2-KGA product using HPLC and TLC

After subjecting the powder solution of the purified 2-KGA product, obtained from the separation through the three types of columns, to analysis using High-Performance Liquid Chromatography (HPLC), it was observed that two distinct peaks emerged. The main peak exhibited a retention Time value of 9.857 minutes, corresponding to the retention time of the standard 2-KGA solution (data not shown). The secondary peak displayed a Retention Time value of 7.529 minutes, aligning with the Retention Time of the standard NaCl solution (data not shown). This is illustrated in Figure 7A. Furthermore, when tested using Thin-Layer Chromatography (TLC) and sprayed with 2,3,5-Triphenyltetrazolium chloride (TTC), only a single spot corresponding to the standard 2-KGA solution was observed, as depicted in Figure 7B.

DOI: 10.60101/jarst.2023.254506

JOURNAL OF APPLIED RESEARCH ON SCIENCE AND TECHNOLOGY

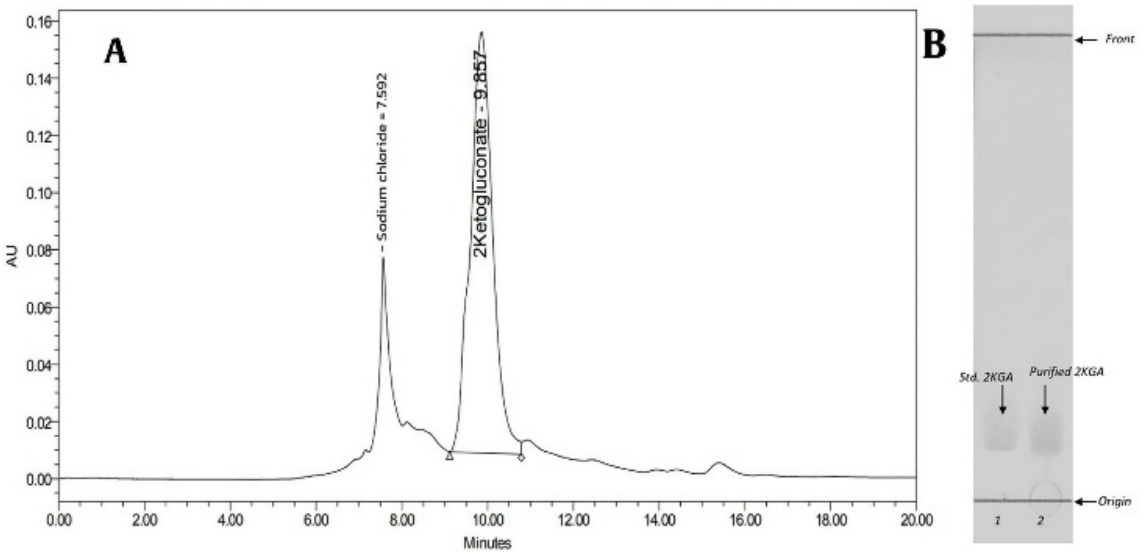

Figure 7 Purity analysis of 2-KGA product obtained from *N. vanlangensis* KKS-R1 by HPLC (A) and TLC (B).

CONCLUSION

The acetic acid bacterium *Nguyenibacter vanlangensis* KKS-R1 has been identified as exceptionally capable of producing 2-KGA at high temperatures up to 40°C, utilizing a minimal liquid medium with sodium gluconate as the carbon source. When the produced 2-KGA is further purified through ion exchange chromatography, two types of columns, a DEAE Sephacel column chromatography, which functions as an anion, and a DOWEX 1X4 column in its chloride form, before being subjected to gel filtration chromatography for increased purity, this efficient process allows the isolation of highly pure 2-KGA with a concentration of 81.90±0.03 mg/mL, constituting 71.02% of the total yield. Subsequently, the 2-KGA product undergoes a decolorization process using activated carbon and is then freeze-dried, resulting in a pure white powder. This study suggests that these processes are viable for industrial application and can be further optimized to enhance production efficiency.

ACKNOWLEDGEMENT

Authors thank, Department of Microbiology Faculty of Science King Mongkut's University of Technology Thonburi and the Thailand Institute of Scientific and Technological Research for the use of experimental equipment and scientific instruments and to facilitate research laboratories used for studies and experiments to complete this research.

REFERENCES

1. Sievers M, Ludwig W, Teuber M. Phylogenetic positioning of *Acetobacter*, *Gluconobacter*, *Rhodopila* and *Acidiphilium* species as a branch of acidophilic bacteria in the α-subclass of Proteobacteria based on 16S ribosomal DNA sequences. Syst Appl Microbiol. 1994;17(2):189-96.
2. Trček J, Mira NP, Jarboe LR. Adaptation and tolerance of bacteria against acetic acid. Appl Microbiol Biotechnol. 2015;99(15):6215-29.
3. Sengun I, Karabiyikli S. Importance of acetic acid bacteria in the food industry. Food Control. 2011; 22:647-56.
4. Wang B, Shao Y, Chen F. Overview on mechanisms of acetic acid resistance in acetic acid bacteria. World J Microbiol Biotechnol. 2015;31.
5. Matsushita K, Toyama H, Adachi O. Respiratory chains and bioenergetics of acetic acid bacteria. In Rose AH, Tempest DW, editors. Advanced in Microbial Physiology. 36: Academic Press; 1994. p. 247-301.
6. Adachi O, Ano Y, Toyama H, Matsushita K. Biooxidation with PQQ-and FAD-dependent dehydrogenases. In Schmid RD, Urlacher V, editors. Modern Biooxidation: Enzyme, Reactions and Application. Wiley; 2007. p. 1-41.
7. Sun L, Wang DM, Sun WJ, Cui FJ, Gong JS, Zhang XM, et al. Two-stage semi-continuous 2-keto-gluconic acid (2KGA) production by *Pseudomonas plecoglossicida* JUIM01 from rice starch hydrolyzate. Front Bioeng Biotechnol. 2020;8:120.
8. Walker R. Erythorbic acid and its sodium salt. Joint FAO/WHO expert committee on food additives (JEFCA), Toxicological evaluation of certain food additives and contaminants Geneva: World Health Organization. 1991:27-60.
9. Wei Z, Yu S, Sun W, Zhou Q, Li Z. Research progress on fermentation production of 2-keto-D-gluconic acid. Food Sci. 2008;29:636-9.

DOI: 10.60101/jarst.2023.254506

10. Shinagawa E, Ano Y, Yakushi T, Adachi O, Matsushita K. Solubilization, purification, and properties of membrane-bound D-glucono-delta-lactone hydrolase from *Gluconobacter oxydans.* Biosci Biotechnol Biochem. 2009;73(1):241-4.
11. Matsushita K, Shinagawa E, Ameyama M. D-Gluconate dehydrogenase from bacteria, 2-keto-D-gluconate-yielding, membrane-bound. Methods Enzymol. 89: Academic Press; 1982. p. 187-93.
12. Shinagawa E, Matsushita K, Adachi O, Ameyama M. D-Gluconate dehydrogenase, 2-keto-D-gluconate yielding, from *Gluconobacter dioxyacetonicus*: purification and characterization. Agric Biol Chem. 1984;48(6):1517-22.
13. Matsushita K, Fujii Y, Ano Y, Toyama H, Shinjoh M, Tomiyama N, et al. 5-keto-D-gluconate production is catalyzed by a quinoprotein glycerol dehydrogenase, major polyol dehydrogenase, in *Gluconobacter* species. Appl Environ Microbiol. 2003;69(4): 1959-66.
14. Shinagawa E, Matsushita K, Adachi O, Ameyama M. Purification and characterization of 2-keto-D-gluconate dehydrogenase from *Gluconobacter melanogenus*. Agric Biol Chem. 1981;45(5):1079-85.
15. Ubonrat J, Somporn M, Nongpanga K, Duangtip M. Isolation and screening of plant growth promoting bacteria (PGPB) from rice (*Oryza sativa*) and rhizosphere soil. Prog Appl Sci Technol. 2018; 8(2):190-204.
16. DeMoss RD. Preparation and determination of gluconic, 2-ketogluconic, and 5-ketogluconic acids. Methods in Enzymology. 3: Academic Press; 1957. p. 232-238.
17. Juechan S, Lorliam W, Sukontasing S, Moonmangmee S, Moonmangmee D. A novel exopolysaccharides from nitrogen fixing acetic acid bacterium, *Nguyenibacter vanlangensis* AR-R3. J Appl Res Sci Technol. 2022;21(2):1-13.
18. Dulley JR, Grieve PA. A simple technique for eliminating interference by detergents in the Lowry method of protein determination. Anal Biochem. 1975;64(1):136-41.
19. Perumpuli PABN, Watanabe T, Toyama H. Pellicle of thermotolerant *Acetobacter pasteurianus* strains: characterization of the polysaccharides and of the induction patterns. J Biosci Bioeng. 2014;118(2):134-8.
20. Purkait MK, Gusain DS, DasGupta S, De S. Adsorption behavior of chrysoidine dye on activated charcoal and its regeneration characteristics by using different surfactants. Separation Sci Technol. 2005;39(10): 2419-40.

DOI: 10.60101/jarst.2023.254506

Received: September 12, 2023 | Revised: November 25, 2023 | Accepted: November 27, 2023

JOURNAL OF APPLIED RESEARCH ON SCIENCE AND TECHNOLOGY
JARST
INSTITUTE OF RESEARCH AND DEVELOPMENT
RAJAMANGALA UNIVERSITY OF TECHNOLOGY THANYABURI
ISSN ONLINE: 2773-9473
https://ph01.tci-thaijo.org/index.php/rmutt-journal

The effect of maltodextrin on properties of salted egg yolk

Sansanee Thimthong[1], Nanoln Dangsungwal[1] and Supuksorn Masavang[2*]

[1]Department Food Service Industry, Faculty of Home Economics Technology, Rajamangala University of Technology Phra Nakhon, Bangkok 10300, THAILAND

[2]Department Food Technology, Faculty of Home Economics Technology, Rajamangala University of Technology Phra Nakhon, Bangkok 10300, THAILAND

[*]Corresponding author: supuksorn.m@rmutp.ac.th

ABSTRACT

Salted eggs are mainly produced through salting treatments that taste salty. However, high sodium intake is part of the pathophysiology of hypertension. Thus, this study aimed to develop low-sodium egg yolks with salting treatment using sodium chloride (NaCl) and maltodextrin to reduce salt content in the salting process. Salted egg yolks were produced using methods in the salting process using maltodextrin (10% and 20% supplement) and were compared to salted eggs brined with 20 and 26% sodium chloride (NaCl) solutions. The moisture content, salt content, color, and texture properties of salted egg yolks during salting for up to 35 days were determined. Nevertheless, salted egg yolks produced with the salting solution using maltodextrin supplement had a significant salt content (0.21-3.30 mg/g) that was lower than the amount discovered in commercial salted yolks (2.84-4.15 mg/g). The results revealed that the maltodextrin substitution affected the salted yolks' properties. The salt contents of all salted egg yolk samples gradually increased during the salting process, along with slight decreases in moisture content as salting time and salt solution concentration increased. The lightness (L*) and the yellowness (b*) decreased while the redness (a*) increased. The hardness, adhesiveness, cohesiveness, gumminess, and chewiness of salted egg yolks increased rapidly over the time of salting, while springiness decreased during the initial stages of salting and reached almost constant levels at the end of salting. As the salting time increased to 35 days, the salted yolk gradually became dark reddish. The maximum denaturation temperature (T_{max}) and denaturation enthalpy (ΔH) of egg proteins increased with increasing salting time. These effects were most pronounced due to the high maltodextrin content of the salting solution. This study suggests that this approach with maltodextrin substitution using the shell egg salting protocol can produce low-sodium salted eggs.

Keywords: Salted egg, Salting method, Egg yolk, Maltodextrin, Sodium chloride

INTRODUCTION

Factors that are physical, chemical, or microbial can harm eggs. Turning eggs into salted egg products is a popular one that is quick, inexpensive, straightforward, and capable of maintaining the nutritional content of eggs [1]. Salted eggs are egg preservation products that contain high levels of unsaturated fatty acids, fat, protein, and minerals and lower phospholipid and cholesterol levels than fresh eggs. All ages can consume them [2, 3]. Making salted eggs mainly involves soaking the eggs in a sodium chloride solution, which imparts a salty flavor and acts as a preservative. However, consuming more salt is a pathophysiologic component of hypertension. Consumption of salt was positively linked with the prevalence of hypertension and the risk of stroke [4]. Many research teams have attempted to produce low-salt salted egg yolks by using a variety of osmotic agents, including maltodextrin, glucose, potassium chloride, sodium chloride, and sucrose [5-7]. In order to lower the salted eggs' sodium content, [1] manufactured salted eggs using a salt paste containing potassium chloride (KCl) as a salt substitute. Although the salted eggs lacked interior sensory properties, their antioxidant potency was equivalent to those without KCl replacement. Using separated chicken egg yolks, [6] also employed osmotic agents to salt egg yolks with a combination of sodium chloride, potassium chloride, and sucrose. Nonetheless, salted egg yolks had a significant salt content close to the highest amount discovered in commercial salted yolks (about 2.84-4.15 mg/g). They resulted from the fact that sugar diffusion through the yolks was significantly slower than that of salt due to sugar's higher molecular weight and the fact that the majority of the sugar remained on the yolk surface [6]. Maltodextrin is a high molecular weight solute. Khin MM, et al. [8] reported that maltodextrin was used as the coating material before osmotic dehydration in fresh apples to control solute uptake. The maltodextrin coating provided an excellent barrier

DOI: 10.60101/jarst.2023.254045

to mass transfers during osmotic dehydration. The results showed that both solute uptake and moisture loss were reduced. A few studies have attempted to add maltodextrin to the osmotic solution to control the incorporation of low molecular weight solutes, such as in the fruit tissues for pickled fruits, with the osmotic dehydration process. This idea was suggested by Azuara E, et al. [5] as a way to lower the amount of salt in salted yolks [7]. This work used the maltodextrin-salt OD system for separating salted duck egg yolk to demonstrate a novel concept of salted yolk processing. The egg yolk became watery and did not develop the desired features, even though this procedure reduced the salting period from 4 weeks to 4 days with salted content, which is equivalent to the result seen using the conventional method employing NaCl.

To address these concerns, salted egg yolks created using the traditional salting method with 20 and 26% sodium chloride solutions and fresh duck eggs made using the shell-salting procedure with a mixture solution of 20% sodium chloride and 10-20% maltodextrin were compared. A thorough understanding of the product's qualities, which has not been publicized, should also be examined. This study aimed to make low-sodium salted egg yolks with salt and maltodextrin, examine their physicochemical properties, and compare low-sodium salted yolks to standard salted yolks.

MATERIALS AND METHODS

The study was conducted at the Department of Food Science and Technology laboratory, Faculty of Home Economics Technology, Rajamangala University of Technology Phra Nakhon, located in Bangkok, Thailand. The research used a completely randomized design (CRD) with three replicates. Fresh duck eggs were acquired at a local market in Bangkok's Dusit district.

1. Chemicals

Sodium chloride (NaCl) was obtained from a local supermarket. Maltodextrin (DE 10-20) was purchased from Zhucheng Dongxiao Biotechnology Co., Ltd. (Shandong, China). Ammonium ferric sulfate ($NH_4Fe(SO_4)_2{\cdot}12H_2O$), Potassium thiocyanate (KSCN), silver nitrate ($AgNO_3$), and nitric acid (HNO_3) were obtained from were supplied by Sigma-Aldrich (Sigma-Aldrich, Co., Ltd., USA). Petroleum ether was purchased from Lab-scan (Bangkok, Thailand). Unless indicated otherwise, the chemicals were analytical grade. To compare the effect of different salting processes. The salting solution consisting of 20% NaCl, saturated NaCl solution (26% NaCl), and 20% NaCl with 10% and 20% maltodextrin were prepared.

2. Salted egg preparation

Duck eggs weighing 65-75 g and an age of less than three days were procured at a local marketplace in the Dusit district of Bangkok, Thailand. Before immersion in salting solutions consisting of 26% salt (mass fraction) and 20% NaCl, supplemented with 10% and 20% maltodextrin, the eggs underwent a cleansing process using running tap water. A thorough inspection was conducted to identify any potential fractures in the eggshell. This treatment regimen was carried out at room temperature and repeated every week for up to 35 days as part of the pickling process. A salt solution was prepared with a weight-to-weight ratio of around 1:3 concerning eggs. A total of six eggs were selected every week for salting. The egg whites and yolks were effectively segregated. A total of ten raw egg yolks were manually isolated and combined to form composite samples for each treatment. The samples were evaluated and analyzed at 7, 14, 21, 28, and 35 days after the salting process. Before instrumental identification, the samples were stored at a temperature of 4 °C in a refrigerator and packed with preservative film.

3. Determination of moisture and NaCl contents of salted egg yolks

The moisture and sodium chloride contents of salted duck egg yolk samples were analyzed using the AOAC (2000) methodology. To assess the moisture content, egg yolk samples weighing between 2.5 and 3.0 grams were evenly dispersed into weighing vials measuring 30 mm x 50 mm. These samples were then dried in a drying oven at a temperature of 105 °C until a constant weight was achieved. The following is the methodology for determining the presence of sodium chloride (NaCl): A total of 5 grams of egg yolk samples were subjected to a solution containing 20 milliliters of silver nitrate ($AgNO_3$) with a concentration of 0.1 moles per liter, along with 10 milliliters of nitric acid (HNO_3) with a concentration of 30 milliliters per 100 milliliters. Except for $AgCl_2$, the mixtures were heated slowly on a hot plate until all solids were dissolved entirely. Subsequently, a volume of 5 mL of a solution containing 5 g of $FeNH_4(SO_4)2{\cdot}12H_2O$ per 100 g of solution was introduced into the mixture when it had reached a temperature of around 24-26 °C. Once the solution exhibited a consistent light brown color, the mixtures were titrated using a standardized KSCN solution with a concentration of 0.1 mol/L. The equation employed for the calculation of the sodium chloride (NaCl) % in the given samples was as follows:

$$\text{NaCl content}\,(\%) = \frac{5.8\times[(V_1\times N_1)-(V_2\times N_2)]}{W} \quad (1)$$

Where;
V_1 = Volume of $AgNO_3$ solution (mL)
N_1 = Concentration of $AgNO_3$ solution (mol/L)
V_2 = Consumed volume of KSCN solution (mL)
N_2 = Concentration of KSCN solution (mol/L)
W = Weight of the salted egg yolk sample

DOI: 10.60101/jarst.2023.254045

JOURNAL OF APPLIED RESEARCH ON SCIENCE AND TECHNOLOGY

4. Determination of Fat contents of salted egg yolks

The Soxhlet extraction technique was employed to determine the lipid content of salted egg yolks. The experiment utilized a SoxtecTM 2055 extraction device manufactured by FOSS Analytical Solutions Pty Ltd. in Victoria, Australia. A total of 2.0 g of salted yolk samples were subjected to extraction for 60 minutes. This extraction process was conducted in individual weighing extraction flasks containing 85 mL of petroleum ether (FOSS 2055). In order to ensure complete removal of any residual solvent, the residue was subjected to an additional 20-minute period of evaporation, followed by heating at 105 °C in a hot air oven for 30 minutes. The determination of crude fat content was performed by applying equation (2) and, after that, expressing it as a percentage of the initial weight of the fresh (wet) sample, considering the variation in sample weight before and after the extraction process.

$$\text{Fat content}\,(\%) = \frac{(F\text{-}T)}{S} \times 100 \qquad (2)$$

Where;
F = Weight of extraction flasks and fat residues (g)
T = Weight of empty extraction flasks (g)
S = Test portion weight (g)

5. Color of salted egg yolk

According to the operation manual, the Chroma Mater CR-400 (Konica Minolta Sensing, Inc., Tokyo, Japan) analyzed the color of raw salted egg yolks nearby. All measurements were recorded six times at room temperature, and the values of lightness (L^*), redness (a^*), and yellowness (b^*) were obtained [9].

6. Determination of texture profile analysis (TPA) of salted egg yolk

The TPA procedure was conducted using a TA-XT Plus texture analyzer manufactured by Stable MicroSystems in Surrey, England, following the methodology outlined in the reference [10]. The salted egg yolks were sliced into pieces measuring 2.0x2.0x2.0 mm. The prepared samples underwent two rounds of compression at a strain of 50% using a cylindrical aluminum probe with a diameter of 50.0 mm. The speeds recorded for the pre-test, test, and post-test were 5.0 mm/s, 1.0 mm/s, and 5.0 mm/s, respectively. The interval between two compression cycles was established as 5.0 seconds. The force-distance deformation curves were measured at a cross-head speed of 5.0 mm/s. Various parameters were obtained: hardness, adhesiveness, springiness, cohesiveness, gumminess, and chewiness. The texture analysis for each treatment was repeated five times.

7. Differential scanning calorimetry analysis

Differential scanning calorimetry (DSC) TA instrument model Q20 was used to determine what happened to the proteins in salted egg yolk when the temperature changed. 5-10 mg of the sample was placed in the DSC hermetic pans. An empty hermetic pan was used as a reference sample. The samples were scanned at 10 °C per minute over the 20–120 °C temperature range. The denaturation temperature (T_{max}) was measured, and the denaturation enthalpy (ΔH) was estimated by measuring the area under the DSC transitions curve using TA analysis software.

8. Statistical analysis

The data were presented as the mean ± standard deviation of triplicate determinations. A one-way analysis of variance (ANOVA) was done, and Duncan's multiple-range tests were used to compare the means. The statistical tool (SPSS 26.0 for Windows, SPSS Inc., Chicago, IL, USA) was used to measure the statistical analyses. The significance of differences was defined at $p \leq 0.05$. The differences among treatments were verified by their least significant difference.

RESULTS AND DISCUSSIONS

1. Changes in moisture and NaCl contents of salted egg yolks

Because the inside and outside of an egg have different amounts of sodium ions (Na^+) and osmotic pressures, the Na^+ slowly goes from the eggshell to the egg white and then to the egg yolk during the salting process. The water molecules in the yolk move through the membrane into the egg white, and the water molecules in the egg white move through the membrane of the eggshell into the salting solution [11]. Figure 1 shows the changes in the amount of water and NaCl. The amount of water in egg yolks decreased as salting time and salt concentration increased. Figure 1A showed that salted egg yolks with maltodextrin salt replacement had less water than those without salt replacement ($p \leq 0.05$). Because egg white and egg yolk have different amounts of osmotic pressure, pickling made the food less liquid. The water moved from the egg yolk to the egg white and from the egg shell into the surroundings. When maltodextrin was used to replace salt in salted yolks, the water went down more than when maltodextrin was not used. Also, osmotic dehydration was higher when the amount of maltodextrin was higher. In addition, Shinde B, et al. [12] suggested that the sucrose and maltodextrin 10DE solution produced higher moisture loss than sucrose, which is composed of a comparatively lower molecular solute. A similar finding was found by Wang TH [7], who observed that when maltodextrin was added to the salting solution, the moisture in a salted yolk sample went down faster.

DOI: 10.60101/jarst.2023.254045

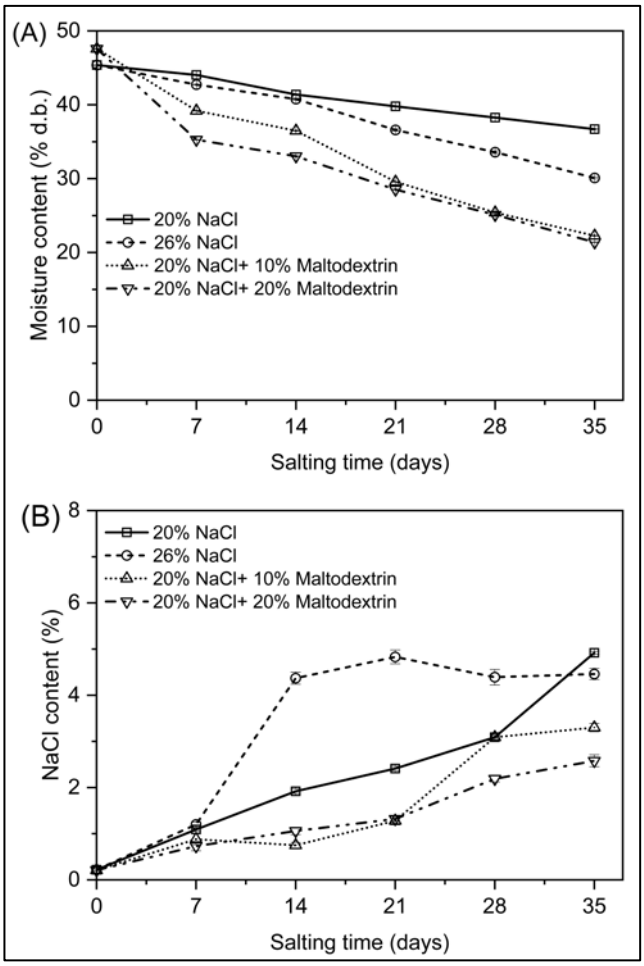

Figure 1 Change in moisture content (A) and NaCl content (B) of salted egg yolks with different salting solutions during 35 days of salting Bars represent the standard deviation from a triplicate determination.

NaCl moved from the salt solution through the eggshell in the white egg during salting. This was because the egg white's osmotic pressure increased, making it easier for the salt to keep penetrating into the egg yolk. At the same time, both the egg white and the egg yolk lost water. Both the absorption of NaCl and the loss of water would cause the yolk to harden [13, 14]. Figure 1B shows that the amount of salt in egg yolks went up significantly ($p \leq 0.05$) as the salting time (7-35 days) and the amount of salt in the salting solution went up. The salt content went up as the salting time went on, but the growth rate slowed as the salting time went on. The salt content of the salted yolks brined in a 26% NaCl solution kept rising and hitting its highest point after 21 days. This shows that the salt content of the yolks salted with maltodextrin substitution changed less quickly than that of the yolks salted in the NaCl solution. Wang TH [7], Ai MM, et al. [10], Xu L, et al. [15] and Xu L [16], have all reported results that are similar to this one. NaCl moves quickly into the egg at the beginning of salting because there is a big difference in osmotic pressure between the salting solution and the egg. Over time, the solidification of the upper yolk during the pickling process will stop some NaCl from moving into the yolk [17]. This behavior can also be explained by the combination of low molecular weight solute and high molecular weight maltodextrin, which can create a solid barrier at the surface, preventing solid gain and ultimately increasing the osmotic potential and water transfer coefficient. This also makes solids mass transfer more difficult [5, 18].

Also, yolk has a lot of oil, and the barrier of the yolk membrane can slow the movement of NaCl into the yolk. This keeps the amount of NaCl in the yolk almost the same at the end of the salting process [19]. Azuara E, et al. [5] said that the maltodextrin molecules were too big to get through the membrane. This made the salt move through the membrane more slowly. Because of this, the amount of salt in salted yolks with maltodextrin replacement went up slowly, while the amount in salted yolks in salt solution went up quickly.

In addition, yolk has a high oil content, and the barrier of the yolk membrane can slow the movement of NaCl into the yolk. This keeps the amount of NaCl in the yolk almost the same at the end of the salting process [20]. Wang TH [7] said that the maltodextrin molecules were too big to get through the membrane. This made the salt move through the membrane more slowly. Because of this, the amount of salt in salted yolks with maltodextrin replacement went up slowly, while the amount in salted yolks in salt solution went up rapidly.

2. Change in fat content of salted egg yolks

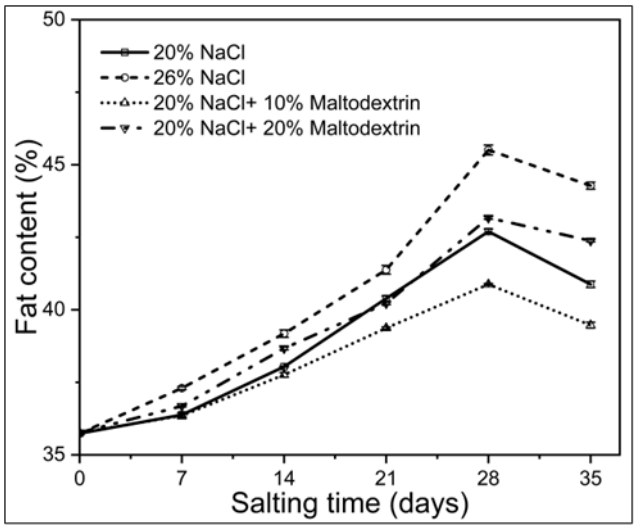

Figure 2 Change in fat content of salted egg yolks with different salting solutions during 35 days of salting. Bars represent the standard deviation from triplicate determination.

Egg yolk is rich in protein and contains a high content of lipids. The fat concentration in eggs was found to be mostly located in the yolk, reaching up to 35% [21]. During seven consecutive days, the

DOI: 10.60101/jarst.2023.254045

JOURNAL OF APPLIED RESEARCH ON SCIENCE AND TECHNOLOGY

yolk's exterior underwent a solidification process, but the interior retained its liquid state. Salting egg yolks primarily results in the hardening of the yolks due to reduced moisture content. The lipid content of salted egg yolks exhibited a modest increase with prolonged salting duration, primarily attributed to osmotic dehydration inside the yolk. This process led to the development of a rigid layer. According to the findings of Suretno N, et al. [22], fat extraction from egg yolk rose upon water removal.

The salting procedure induces a chemical reaction between low-density lipoprotein (LDL), the primary lipid component found in the yolk, and the salting solution. As a result of structural modifications induced by dehydration and exposure to a hypertonic environment, low-density lipoprotein (LDL) micelles undergo the release of their lipid constituents. According to previous research, it was found that the lipid content in the yolk increased from 8.5% to 16.5% over up to 14 days during the salting process [23]. According to Figure 2, the fat content of salted yolks, created using a combination of 20% NaCl and 20% maltodextrin, exhibits the greatest value, reaching 42.38% after the salting process. This finding suggests that the dehydrating effects of NaCl and maltodextrin contribute to the loss of water in the yolk, leading to an increase in oil extraction and free lipids release. These effects are mostly attributed to the structural modifications in low-density lipoproteins (LDL) during salting [15].

3. Change in color of salted egg yolks

The color data about egg yolks, as presented in Table 1, indicated a slight increase in both lightness (L^*) and yellowness (b^*) across all samples throughout a pickling period of 35 days in 20% and 26% NaCl, whereas steady decline trends of L^* and b^* for salted yolks salting in a mixture of 20% NaCl and 10-20% maltodextrin was observed. The observed alteration in color could be attributed to the desiccation experienced by the egg yolks throughout the pickling procedure.

The yellow color of egg yolks is influenced by the concentration of pigments, specifically xanthophyll and zeaxanthin [17, 24] and has been influenced by the concentration of pigments. The study of Wang X, et al. [9] suggested that the observed rise in redness could be attributed to the release of lutein and zeaxanthin, which are contained inside lipids [23]. The egg yolk subjected to prolonged storage under low moisture exhibited a noticeable deepening in its golden color.

Table 1 Color measurements of salted egg yolks during salting.

Salting solution	Salting time (days)	Color		
		L^*	A^*	B^*
20% NaCl	7	30.77^{ghij}±1.13	9.87^{h}±1.72	5.75^{fgh}±1.82
	14	29.05^{j}±0.91	12.24^{efg}±1.92	7.08^{efg}±1.46
	21	30.53^{gij}±1.91	15.17^{bc}±2.67	7.24^{efg}±1.85
	28	33.42^{def}±1.89	14.31^{bcd}±1.41	9.97^{abcd}±1.14
	35	37.20^{bc}±2.63	13.20^{cdefg}±1.98	9.0^{bcd}±1.79
26% NaCl	7	26.77^{k}±0.42	10.92^{gh}±0.66	6.09^{fg}±1.00
	14	29.49^{ij}±0.64	12.48^{defg}±1.32	7.12^{efgh}±1.14
	21	31.54^{fghi}±1.41	15.68^{b}±1.68	7.59^{ef}±1.09
	28	35.26^{bcd}±2.36	14.88^{bcde}±1.87	11.15^{b}±1.77
	35	39.95^{a}±1.81	14.74^{bcd}±1.82	10.65^{bc}±1.59
20% NaCl + 10% maltodextrin	7	41.56^{a}±0.92	18.81^{a}±0.61	25.56^{a}±1.64
	14	32.76^{efg}±2.17	10.81^{gh}±1.92	5.94^{efgh}±1.50
	21	30.30^{hij}±1.72	13.61^{bcdef}±1.56	7.82^{de}±2.14
	28	37.48^{b}±2.18	14.26^{h}±1.07	8.48^{i}±1.74
	35	33.24^{def}±2.07	14.13^{bcde}±1.53	10.25^{bc}±1.34
20% NaCl + 20% maltodextrin	7	42.12^{a}±0.80	19.09^{a}±0.61	26.31^{a}±1.43
	14	32.12^{fgh}±2.31	11.09^{gh}±1.78	3.97^{hi}±1.60
	21	30.45^{ghij}±2.07	12.94^{cdefg}±1.49	7.31^{efg}±1.66
	28	36.16±2.19^{bc}	13.32^{fgh}±1.10	7.15^{ghi}±1.40
	35	34.92^{cde}±1.90	13.76^{bcde}±1.02	8.67^{cde}±1.56

Measurements were made six times for each sampling group.
Different lower-case letters (a-g) in the same column indicate significant differences ($p \leq 0.05$).

DOI: 10.60101/jarst.2023.254045

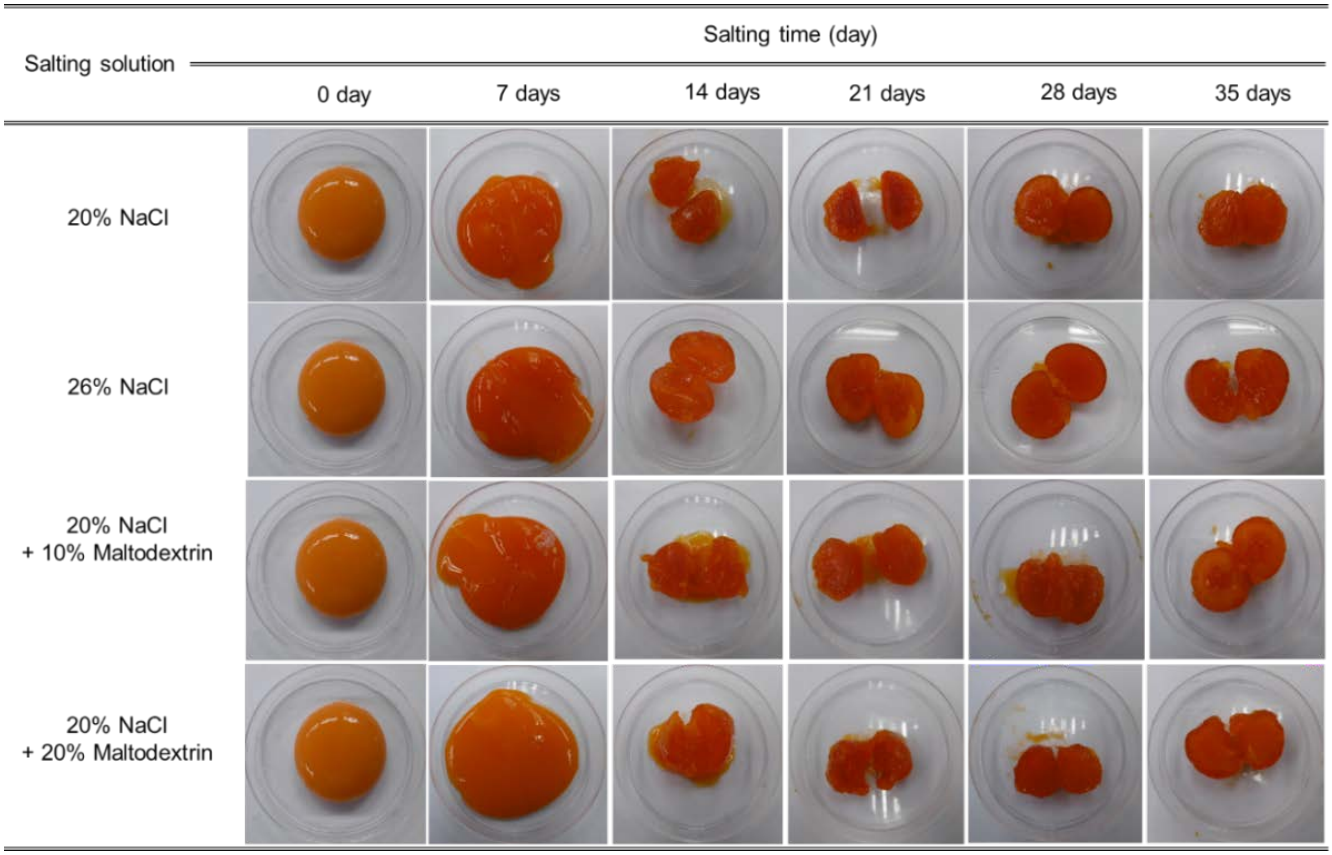

Figure 3 Appearance of salted eggs with different salting solutions during 35 days of salting.

The observed phenomenon can be attributed to the extraction of moisture, disruption of the emulsion of salted egg yolk, and the release of oil [23], which was mitigated to a lesser extent by incorporating maltodextrin. The findings are presented in reference [17]. This observation implies that the orange hue of salted egg yolk could be attributed to the heightened concentration of pigments.Consequently, the desiccation of egg yolks in the course of the salting procedure exerted an influence on both the consistency and pigmentation of the salted yolk derivative.

Figure 3 illustrates the impact of salting solutions and salting time on the visual characteristics of salted egg yolk. Throughout the 5-week salting period, the salted egg yolk acquired a progressively reddish hue across all salting solutions. After 35 days of salting, the yolks subjected to various solutions exhibited a firm and dehydrated center, accompanied by a more intense pigmentation. The alteration in hue observed in salted egg yolks during the salting process may be attributed to the reduction in moisture content, which leads to a higher concentration of pigments and free lipids within the yolks [25].

4. Change in the texture of salted egg

As shown in Figure 4B, the springiness gradually decreased throughout salting. Extremely alkaline conditions lead to the yolk proteins cross-linking and may cause a tighter connection. During 28-35 days of salting, the egg yolk gel network structure is extensively formed by electrostatic interaction forces and dehydration to a constant degree, which may contribute to the stability of springiness [3].

The adhesiveness of the salted yolk increased continuously and reached its maximum at 21 days of salting (Figure 4C). Yolks salted with maltodextrin substitution at 21-35 days exhibited higher adhesiveness than those salted with NaCl only ($p \leq 0.05$). The potential connection may also involve the liberation of unbound lipids from the lipoprotein, which contributes to the increased adhesiveness of the yolk and the reinforcement of a gel-like network during the process of yolk solidification [15].

Salted egg yolks became more cohesive from 1 to 5 weeks of salting (Figure 4D). Because the proteins in egg yolks are highly charged, they may experience unfolding at high pH levels.The intramolecular repulsions and intermolecular interactions caused by those proteins would increase noticeably [3]. Moreover, salt might help such unfolded proteins interact [26, 27]. The mechanism of salt-induced aggregation of yolk proteins with NaCl addition was disclosed by Kaewmanee T, et al. [28]. When salt is added to egg suspensions, it affects the hydrophilic groups in the protein backbone and encourages protein aggregation, which could create a gel-like network due to an increase in hydrophobicity [29]. The gumminess and chewiness of salted yolks increased with longer salting times in both the NaCl salting

DOI: 10.60101/jarst.2023.254045

JOURNAL OF APPLIED RESEARCH ON SCIENCE AND TECHNOLOGY

and maltodextrin substitution processes ($p \leq 0.05$). The yolks salted with a maltodextrin substitution solution for 35 days exhibited increased levels of gumminess and chewiness compared to those only salted with a NaCl solution, as depicted in Figures 4D and 4E. The increased gumminess and chewiness observed in the yolks may be attributed to using maltodextrin as a substitute for salting, as it promotes dehydration. Furthermore, it has been claimed by Kaewmanee T, et al. [13] and Xu L, et al. [15] that there was an increase in the concentration of proteins or lipoproteins, leading to enhanced interactions among them.

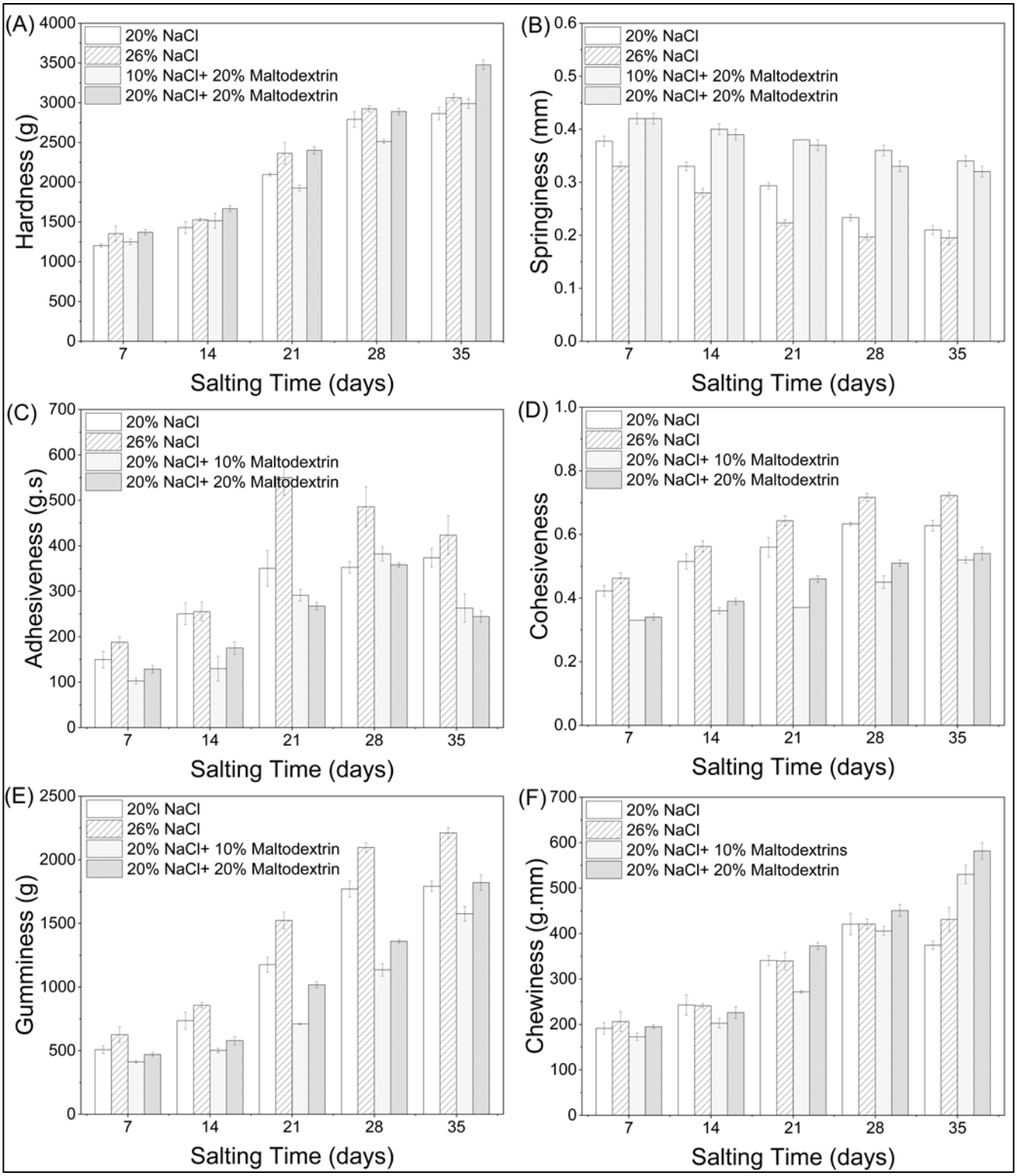

Figure 4 Texture profile analysis (hardness (A), springiness (B), adhesiveness (C), cohesiveness (D), gumminess (E), and chewiness (F) of salted egg yolks with different salting solutions during 35 days of salting Bars represent the standard deviation from six measurements.

DOI: 10.60101/jarst.2023.254045

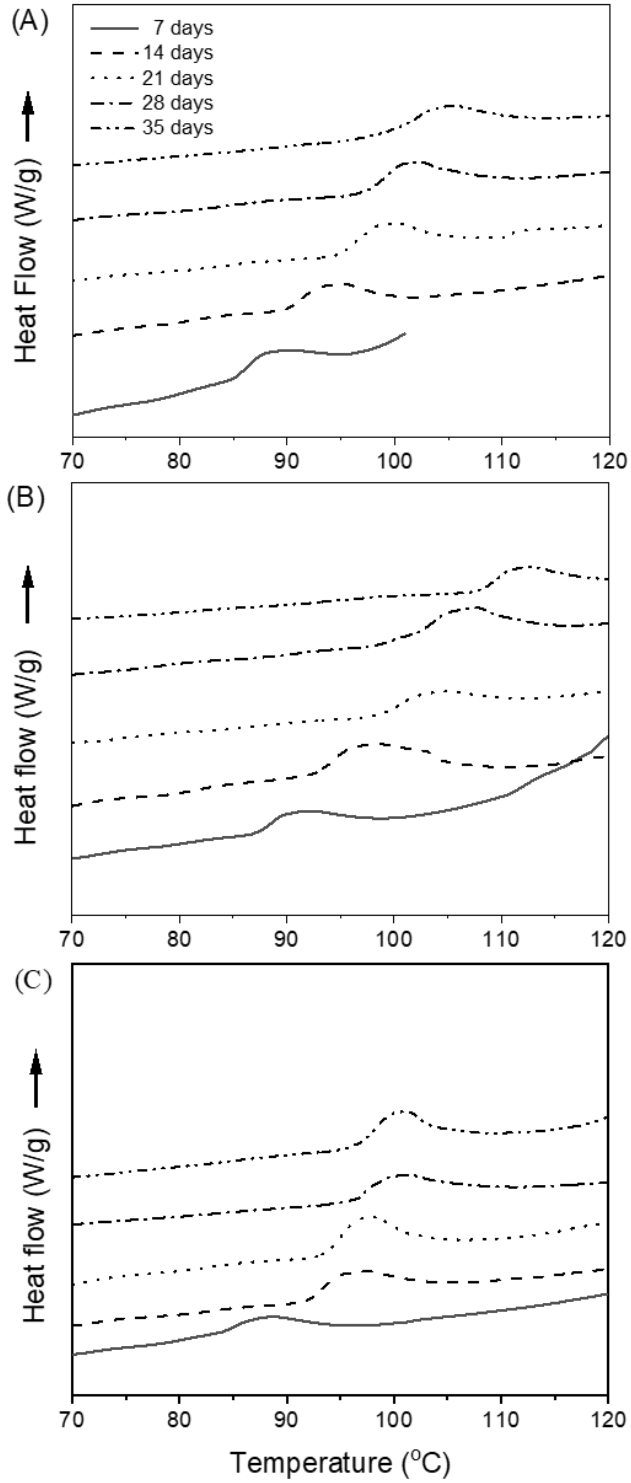

Figure 5 DSC analysis of salted egg yolk proteins during salting for 7-35 days in different salting solutions. A: 20% NaCl; B: 26% NaCl; C: a mixture of 20% NaCl and 20% maltodextrin.

5. DSC analysis of salted egg yolk proteins during the salting process

Figure 5 displayed the DSC thermogram curves, while Table 2 presented the maximum transition temperature and denaturation enthalpy of salted egg yolks. These measurements were obtained from three different samples: 20% NaCl, 26% NaCl, and a mixture of 20% NaCl and 20% maltodextrin. The salting process lasted for 7-35 days, and the DSC technique was employed to monitor the changes in the salted egg yolk proteins.

The relationship between the change in denaturation temperature and enthalpy can be attributed to the alterations in composition and conformation resulting from the salting processes [9, 20]. An endothermic peak was observed for salted yolk salting with T_{max} values of 88.07-103.85 °C for yolks salting 20% NaCl, 90.46-102.72 °C for yolks salting 26% NaCl and 88.55-100.70 °C for yolks salting the mixture of 20% NaCl and 20% maltodextrin. The thermograms of samples showed that the characteristic peak showed a significant increase with the increasing salting time. Higher T_{max} of salted yolk tended to be found with salting in 26% NaCl, particularly with longer salting durations. The observed change in denaturation temperatures aligns with the concurrent rise in salted egg yolk surface hydrophobicity during the salting process. According to the study conducted by Xu L, et al. [2], an increased presence of hydrophobic groups or proteins with a more compact structure leads to an elevated denaturation temperature. The observed phenomenon might likely be attributed to the elevated concentration of salt, which leads to a more robust network architecture and the aggregation of yolk protein under thermal conditions. A comparable pattern was documented by the study conducted by Kaewmanee T, et al. [20].

According to the data presented in Table 2 and Figure 5, including maltodextrin resulted in a modest decrease in the denaturation temperature of salted egg yolks. This decrease was observed when eggs were salted using a solution of 20% NaCl and 20% maltodextrin, compared to a solution containing only salt. According to prior research [6], it has been seen that the rate at which sugar diffuses into the yolk is comparatively slower than that of salt. This disparity can be attributed to the higher molecular weight of sugar. Additionally, it has been noted that a portion of the sugar tends to persist on the egg yolk's surface, potentially impeding salt migration into the yolk. Based on the provided explanation, maltodextrin, similar to sugar, is a solute with a high molecular weight that can impede salt absorption. Reducing salt consumption may lead to an increased prevalence of hydrophobic moieties or proteins with enhanced structural stability and a marginal decrease in denaturation temperatures. The values of denaturation enthalpy exhibited variation in response to different salting procedures and durations. The results of all treatments exhibited a positive correlation between the duration of salting and the observed rise in enthalpy.

DOI: 10.60101/jarst.2023.254045

JOURNAL OF APPLIED RESEARCH ON SCIENCE AND TECHNOLOGY

Table 2 The denaturation temperature (T_{max}) and enthalpy (ΔH) of salted egg yolk proteins during 35 days of salting.

Sample	Salting time (day)	T_{max} (°C)	ΔH (J.g^{-1})
20% NaCl	7	88.07^{g}±0.07	1.09^{f}±0.33
	14	94.31^{f}±1.09	1.27^{ef}±0.04
	21	99.71^{cd}±0.16	1.84^{bcd}±0.10
	28	102.29^{ab}±0.72	2.29^{ab}±0.17
	35	103.85^{a}±1.78	2.37^{a}±0.06
26% NaCl	7	90.46±1.44^{f}	1.24^{ef}±0.17
	14	97.52^{de}±0.89	1.56^{def}±0.26
	21	100.59^{bc}±1.03	2.11^{abc}±0.32
	28	101.14^{bc}±0.39	2.22^{ab}±0.01
	35	102.72^{ab}±0.25	2.37^{a}±0.01
20% NaCl + 20% maltodextrin	7	88.55^{fg}±0.49	1.34^{ef}±0.02
	14	96.64^{e}±0.04	1.67^{cde}±0.01
	21	98.84^{cde}±0.36	1.83^{bcd}±0.03
	28	100.87^{bc}±0.09	2.00^{abcd}±0.04
	35	100.70^{bc}±0.57	2.22^{ab}±0.19

Mean±S.D. from duplicate measurements.
Different lower-case letters (a-g) in the same column indicate significant differences ($p \leq 0.05$).

The salted egg yolks exhibited greater enthalpy when subjected to a combination containing 20% NaCl and 20% maltodextrin solution. The primary factor contributing to the enthalpy of protein denaturation primarily stems from the presence of alternate secondary and tertiary protein structures. Protein secondary structure is primarily influenced by hydrogen bonding, hydrophobic interactions, and ionic strength [2, 30]. On the other hand, the tertiary structure of proteins involves the aggregation of proteins and peptides in egg yolk following a salting process lasting 7-35 days. This process leads to a modification in the endothermic properties of the salted egg yolk [31]. Similar trends were reported by Kaewmanee T, et al. [20] and [2].

CONCLUSION

Characteristics of salted egg yolks were affected by salting solutions and salting time. Salted yolks obtained with the different salting solutions showed different oil content, color, transition temperature, and textural properties. The sodium level of salted egg yolks prepared using the immersing method with maltodextrin salt substitution was intended to be comparable to that of salted eggs prepared without maltodextrin substitution. Maltodextrin was used as a salt suppressant and dewatering agent. A salting solution containing 20% NaCl and 20% maltodextrin prevents over-salting of the salted yolk and produces salted egg yolks with a lower sodium content than traditional salted yolks. The physicochemical evaluation of salted egg yolks with maltodextrin substitution revealed that their overall qualities were the same as those produced with only sodium chloride treatment. This information is very useful for developing low-sodium salted eggs that hypertension patients can consume, but more bioavailability research is required to provide more comprehensive information about the health benefits of low-sodium salted eggs.

ACKNOWLEDGEMENT

The authors would like to thank the Department of Food Technology, Faculty of Home Economics Technology, and Rajamangala University of Technology Pha Nakhon for providing research facilities for this study. Additionally, the authors would like to acknowledge the research fund under the project to promote invention and innovation for the new generation in 2021.

REFERENCES

1. Ariviani S, Fitriasih NH, Ishartini DI. Development of low sodium salted eggs and its antioxidant potential. Indonesian Journal of Nutrition and Dietetics. 2017;5(2):51-9.
2. Xu L, Zhao Y, Xu M, Yao Y, Nie X, Du H, et al. Changes in aggregation behavior of raw and cooked salted egg yolks during pickling. Food Hydrocolloids. 2018;80:68-77.
3. Yang Y, Zhao Y, Xu M, Wu N, Yao Y, Du H, et al. Changes in physico-chemical properties, microstructure and intermolecular force of preserved egg yolk gels during pickling. Food Hydrocolloids. 2019;89:131-42.
4. Adrogué HJ, Madias NE. Sodium and potassium in the pathogenesis of hypertension. N Engl J Med. 2007;356(19):1966-78.

DOI: 10.60101/jarst.2023.254045

5. Azuara E, Beristain CI, GutiÉRrez GF. Osmotic dehydration of apples by immersion in concentrated sucrose/maltodextrin solutions. J Food Process Pres. 2002;26(4):295-306.
6. Saeaung W, Laoharatanahiran A, Boonyaprapasorn A, Thipayarat A. Novel processing of salted yolk production using separated yolk brining methodology. Food Innovation Asia Conference: Indigenous Food Research and Development to Global Market, June 17-18, BITEC, Bangkok, Thailand. 2010.
7. Wang TH. Salting yolks directly using fresh duck eggy yolks with salt and maltodextrin. Japan Poulty Science Associations. 2017;54(1):97-102.
8. Khin MM, Zhou W, Yeo SY. Mass transfer in the osmotic dehydration of coated apple cubes by using maltodextrin as the coating material and their textural properties. J Food Eng. 2007;81 (3):514-22.
9. Wang X, Huang Y, Zhou B, Xu W, Xiang X, Huang Q, et al. Improvement of quality and flavor of salted egg yolks by ultrasonic assisted cooking. Ultrason Sonochem. 2021;75:105579.
10. Ai MM, Guo SG, Zhou Q, Wu WL, Jiang AM. The investigation of the changes in physicochemical, texture and rheological characteristics of salted duck egg yolk during salting. LWT. 2018;88:119-25.
11. Bao Z, Kang D, Li C, Zhang F, Lin S. Effect of salting on the water migration, physicochemical and textural characteristics, and microstructure of quail eggs. LWT. 2020;132:109847.
12. Shinde B, Ramaswamy HS. Kinetic modeling of microwave osmotic dehydration of mangoes under continuous flow medium spray conditions using sucrose and maltodextrin (10-18 DE) solute mixtures. Dry Technol. 2021;39(6):713-25.
13. Kaewmanee T, Benjakul S, Visessanguan W. Changes in chemical composition, physical properties and microstructure of duck egg as influenced by salting. Food Chem. 2009;112(3): 560-9.
14. Lai KM, Chung WH, Jao CL, Hsu KC. Oil exudation and histological structures of duck egg yolks during brining. Poultry Sci. 2010;89(4):738-44.
15. Xu L, Zhao Y, Xu M, Yao Y, Nie X, Du H, et al. Effects of salting treatment on the physicochemical properties, textural properties, and microstructures of duck eggs. Plos One. 2017;12(8):e0182912.
16. Xu L, Zhao Y, Xu M, Yao Y, Wu N, Du H, et al. Changes in physico-chemical properties, microstructure, protein structures and intermolecular force of egg yolk, plasma and granule gels during salting. Food Chem. 2019; 275:600-9.
17. Chi SP, Tseng KH. Physicochemical properties of salted pickled yolks from duck and chicken eggs. J Food Sci. 1998;63(1):27-30.
18. Dermesonlouoglou EK, Pourgouri S, Taoukis PS. Kinetic study of the effect of the osmotic dehydration pre-treatment to the shelf life of frozen cucumber. Innov Food Sci Emerg. 2008; 9(4):542-9.
19. Anton M. Egg yolk: structures, functionalities and processes. J Sci Food Agr. 2013;93(12):2871-80.
20. Kaewmanee T, Benjakul S, Visessanguan W. Effect of salting processes on chemical composition, textural properties and microstructure of duck egg. J Sci Food Agr. 2009;89:625-33.
21. Schultz JR, Snyder HE, Forsythe RH. Co-dried carbohydrates effect on the performance of egg yolk solids. J Food Sci. 1968;33(5):507-13.
22. Suretno N, Novitasari E, Rivaie A. The fat content and the preferences of salted duck egg enriched with black and white pepper. IOP Conference Series: Earth and Environmental Science. 2021; 653:012086.
23. Lai KM, Chi SP, Ko WC. Changes in yolk states of duck egg during long-term brining. J Agr Food Chem. 1999;47(2):733-6.
24. Karunajeewa H. The performance of cross-bred hens given free choice feeding of whole grains and a concentrate mixture and the influence of source of xanthophylls on yolk colour. Brit Poultry Sci. 1978;19(6):699-708.
25. Kaewmanee T, Benjakul S, Visessanguan W. Effects of salting processes and time on the chemical composition, textural properties, and microstructure of cooked duck egg. J Food Sci. 2011;76(2):S139-47.
26. Ganasen P, Benjakul S. Physical properties and microstructure of pidan yolk as affected by different divalent and monovalent cations. LWT - Food Science and Technology. 2010;43(1):77-85.
27. Wang W, Nema S, Teagarden D. Protein aggregation—Pathways and influencing factors. Int J Pharm. 2010;390(2):89-99.
28. Kaewmanee T, Benjakul S, Visessanguan W, Gamonpilas C. Effect of sodium chloride and osmotic dehydration on viscoelastic properties

DOI: 10.60101/jarst.2023.254045

JOURNAL OF APPLIED RESEARCH ON SCIENCE AND TECHNOLOGY

and thermal-induced transitions of duck egg yolk. Food Bioprocess Tech. 2013;6(2):367-76.

29. Yang SC, Baldwin RE. Functional Properties of Eggs in Foods. In: Stadelman WJ, Cotterill OJ, editors. Egg science and technology. 4th ed. Binghamton: Food Products Press; Haworth Press; 1995. p. 405-63.

30. Arntfield SD, Murray ED. The Influence of Processing Parameters on Food Protein Functionality I. Differential Scanning Calorimetry as an Indicator of Protein Denaturation. Can Inst F Sci Tec J. 1981;14(4):289-94.

31. Jaekel T, Ternes W. Changes in rheological behaviour and functional properties of hen·s egg yolk induced by processing and fermentation with phospholipases. Int J Food Sci Tech. 2009;44(3):567-73.

DOI: 10.60101/jarst.2023.254045

Received: September 6, 2023 | Revised: December 9, 2023 | Accepted: December 12, 2023

Fabrication of PS-TiO_2 hybrid via mini-emulsion polymerization: Study the effect of crosslink on the photocatalytic properties of the hybrid

Thanapong Phetsombun[1], Tanapak Metanawin[1] and Siripan Metanawin[2,3*]

[1]Department of Materials and Production Technology Engineering, Faculty of Engineering, King Mongkut's University of Technology North Bangkok, Bangkok 10800, THAILAND

[2]Department of Textile Engineering, Faculty of Engineering, Rajamangala University of Technology Thanyaburi, Pathum Thani 12110, THAILAND

[3]Materials Design and Development (AMDD) Research Unit, Faculty of Engineering, Rajamangala University of Technology Thanyaburi, Pathum Thani 12110, THAILAND

[*]Corresponding author: siripan.m@en.rmutt.ac.th

ABSTRACT

In this study, a polystyrene (PS)/nano-TiO_2 hybrid was prepared by a mini-emulsion polymerization process to improve the photocatalytic properties when the crosslinking agent was added. *N, N'*-methylenebis (acrylamide) (MbA) was used as a crosslinking agent. The effect of a crosslinking agent on the photocatalytic properties was studied. The diameter, morphology, and photocatalytic properties of the samples were characterized and discussed. The methylene blue discoloration was monitored at 660 nm by a spectrophotometer. The result showed that the L* value from the Hunter color scale for 7 wt% TiO_2-PS/0.25 wt% MbA was highest at 73.73. It was noticed that the 7 wt% TiO_2 - PS/0.25 wt% MbA hybrid gave the highest photocatalytic properties. The FE-SEM confirmed the well-defined structure with a spherical shape and network formation to improve the photocatalytic properties. The diameter and morphology of the PS/TiO_2 hybrid were in the range of 76 nm to 95 nm by using a field emission scanning electron microscope (FE-SEM). The particle size of the 1 wt% TiO_2 - PS/0.25 wt% MbA was 76 nm, which was smaller than that of the pristine PS of 88 nm. The particle size of the 7 wt% TiO_2 – PS/0.25 wt% MbA hybrid was increased by 25%. The HR-TEM image of the PS/TiO_2 hybrid was studied to confirm the encapsulation of TiO_2 particles in the hybrid. The FFT image of PS/MbA/TiO_2 7 wt% demonstrated the crystalline structure of TiO_2 (dot) and the amorphous structure of PS (ring). FT-IR spectroscopy confirmed the presence of the Ti-O functional group in the PS hybrid spectra. It was noticed that the TiO_2 particles were successfully encapsulated in the PS/TiO_2 hybrid.

Keywords: Mini-emulsion polymerization, Hybrid, Crosslinking agents, Photocatalytic properties

INTRODUCTION

Inorganic-organic nanocomposites in which inorganic (metal oxide) fillers are uniformly dispersed in a polymer matrix have developed strength, toughness, processability, dimensional stability, and wear properties [1-4]. The properties of polymer nanocomposites are affected by the type, size, shape, and concentration of incorporated particles, as well as their interaction with the polymer [5-7].

Polymer hybrids are versatile materials in inorganic-organic nanocomposites. It was the combination of two types of polymers and inorganic nanoparticles to generate advanced materials with possessing properties [8-11]. Therefore, hybrids have been successfully used for various stable inorganic colloids free from aggregation, such as titanium oxide, zinc oxide, magnetic and metal nanoparticles. Mini-emulsion polymerization is one of the common methods for preparing polymer hybrids in colloid systems [12-17].

Titanium dioxide is a widely studied material due to its unique optical, electrical, and chemical properties. It is well-known for its photovoltaic and photocatalytic properties, along with its applications in the paint, paper, and food industries as pigment, filler, or whitener [18-20]. In order to improve the photocatalytic behavior, it is necessary to modify the surface of TiO_2 nanoparticles [21]. This work aimed to synthesize and characterize a novel hybrid material based on TiO_2 nanoparticles. The TiO_2 particles were modified through a mini-emulsion polymerization process in order to improve the surface area and photocatalytic behavior.

MATERIALS AND METHODS

Materials

Styrene monomer (99%, Sigma-Aldrich) was purified by passing through aluminum oxide before

DOI: 10.60101/jarst.2023.253757

JOURNAL OF APPLIED RESEARCH ON SCIENCE AND TECHNOLOGY

being used. Titanium dioxide (TiO_2 99%, US Research Nanomaterials), aluminum oxide basic (Al_2O_3, Sigma-Aldrich), hexadecane (HD, 99%, Sigma-Aldrich), sodium dodecyl sulfate (SDS, 99%, Sigma-Aldrich), potassium persulfate (KPS, 99%, Sigma-Aldrich), and *N, N'*-methylenebis (acrylamide) (MbA, 99%, Sigma-Aldrich) were used as received. Deionized water (DI water) was purified by a Micra™ water purifier from ELGA LabWater.

Preparation of polystyrene hybrids

The mini-emulsion polymerization of the polystyrene hybrid was synthesized as follows: 5.00 g of styrene monomer and 0.20 g of hexadecane were mixed in the presence/absence of 0.25 g of MbA. 0.06 g of SDS was dispersed in 20.0 cm^3 of water. Then, the dispersion was mixed with the monomer mixture in the flask and stirred under nitrogen gas for 15 minutes. The flask was sonicated (130 W and 60 % amplitude) in an ice bath for 15 minutes. After raising the mini-emulsion temperature to 70 °C, 0.083 g of KPS was injected into the flask. The reaction time was carried out for 4 hours. The mini-emulsion was achieved by cooling in an ice bath. The experimental details for the syntheses of PS and PS/MbA/TiO_2 are given in Table 1.

Table 1 The experimental details of the syntheses of PS and PS/MbA/TiO_2.

Sample name	MbA (% wt)	TiO_2 (% wt)
PS	-	-
PS/TiO_2 10%	-	10
PS/MbA	0.25	-
PS/MbA/TiO_2 1%	0.25	1
PS/MbA/TiO_2 3%	0.25	3
PS/MbA/TiO_2 7%	0.25	7
Neat TiO_2	-	10

Characterization

1. Fourier-transform infrared spectroscopy (FT-IR)

The functional and bonding structures of the PS hybrid were analyzed using a PerkinElmer Frontier spectrometer from the USA. The samples were performed in the range of 4000-400 cm^{-1}.

2. Field Emission Scanning electron microscope (FE-SEM)

The morphology of the PS hybrid was observed on a Jeol JSM-7600F from Japan. The particle size distribution was measured using ImageJ software.

3. High-resolution Transmission electron microscope (HR-TEM)

The morphology and crystalline structure of the PS hybrid were determined on a Jeol JEM-3100F from Japan.

Photocatalytic behavior

The photocatalytic activity of the PS hybrid was examined by observing the discoloration of MB under UV-A (365 nm) TL-K 40W/10-R light from the Netherlands. 1 mL of PS hybrids was prepared in 10 ppm of the MB solution. The samples were tested without purification. The UV light intensity was 6.0 mW/cm^2. The MB discoloration was monitored at 660 nm using an UltraScan Pro Color spectrophotometer with a 512-element diode array (from HunterLab, USA).

RESULTS AND DISCUSSION

FT-IR spectroscopy was employed to analyze the functional group and bonding of the PS hybrid. Figure 1 presents the FT-IR spectra of PS, PS/MbA/TiO_2 with various 1, 3, and 7 wt% of TiO_2 contents. It was found that the broad peak at 3423 cm^{-1} corresponds to the stretching of the surface hydroxyl or absorbed water [22, 23]. The main absorption bands of PS over the 2800-3100 cm^{-1} range were attributed to C-H stretching vibrations in the main chain and aromatic rings [23]. The absorption bands at 3025, 3063, 3084, 1600, and 1492 cm^{-1} were assigned to aromatic ring vibrations. The absorption bands at 2921, 2848, and 1451 cm^{-1} were ascribed to the aliphatic backbone of the polystyrene macromolecule. The characteristic absorption bands of Ti-O particles were observed at 692 cm^{-1} [22]. It was shown that the absorption bands of the PS matrix were not affected by the encapsulated TiO_2 particles. It concluded that the TiO_2 was presented in PS hybrids.

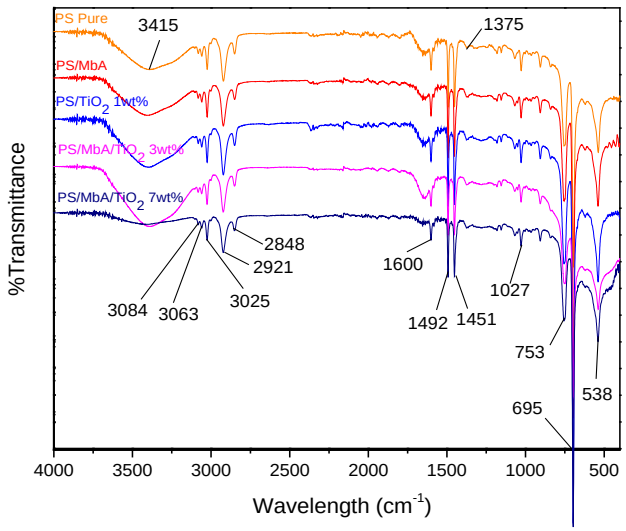

Figure 1 FT-IR spectra of PS, PS/MbA/TiO_2 with various 1-7 wt% TiO_2 contents.

FE-SEM was employed to observe the morphology of the PS hybrids. Figure 2 demonstrates the SEM images of PS hybrid TiO_2 1, 3, and 7 wt% and their particle size distribution. The result shows that the particle diameter of the PS/MbA was 76 nm, as presented in Figure 2a. Moreover, the PS/MbA/TiO_2 1 and 3 wt% were similar at 88 nm, as shown in Figures 2c and 2e. For 7 wt% TiO_2 in Figure 2g, the particle diameter of PS/MbA/TiO_2 was increased to 95 nm, which increased by 25%. The particle size distribution of the PS and PS hybrids demonstrated

DOI: 10.60101/jarst.2023.253757

a narrow size distribution, as seen in Figures 2b, 2d, and 2f. It concludes that the encapsulation of TiO_2 in the PS mini-emulsion caused an increase in the final particle size of the hybrid. This was due to an increase in the amount of TiO_2 in the PS hybrid [24].

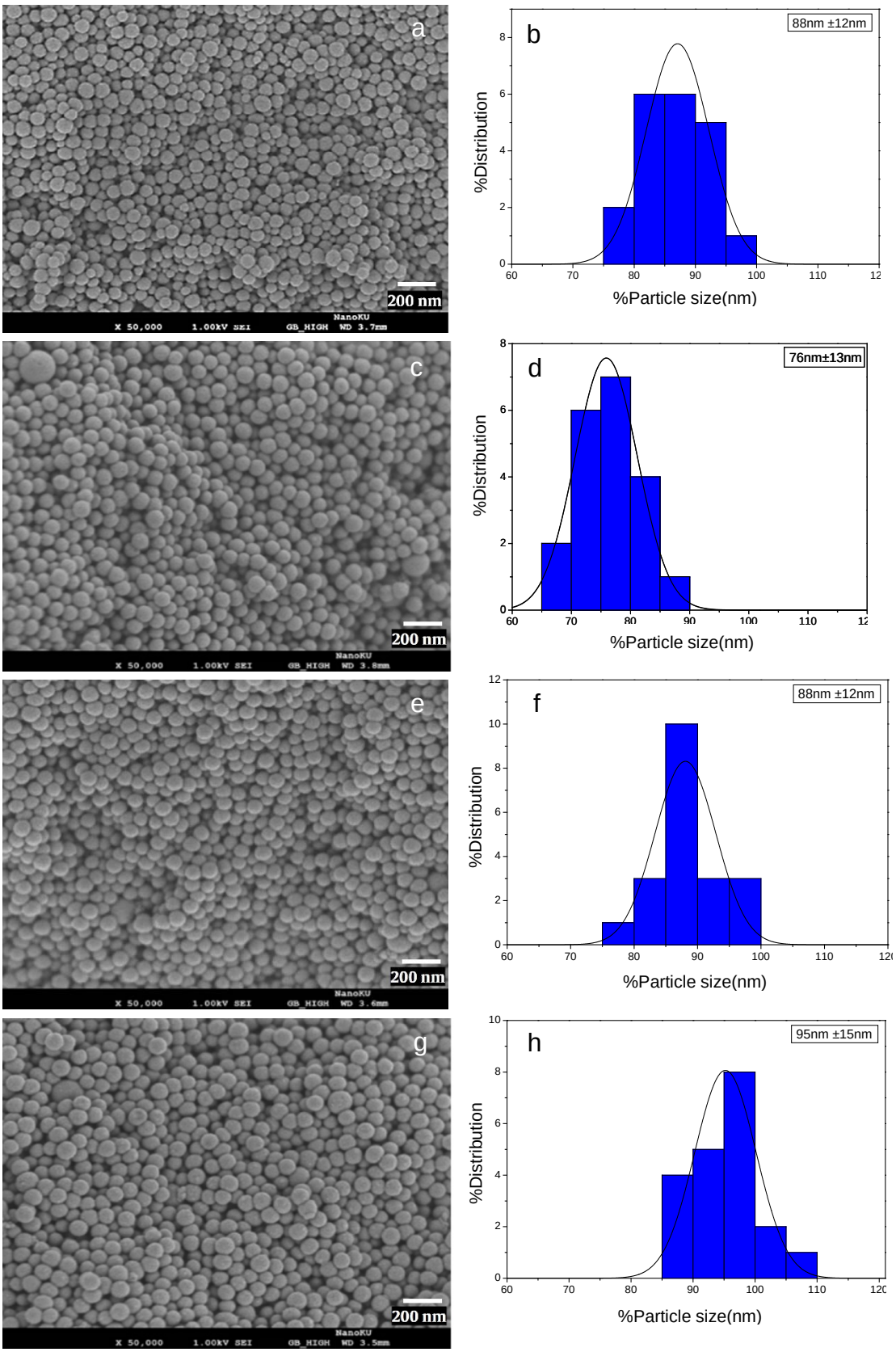

Figure 2 SEM images of PS hybrids and their particle size distribution of (a-b) PS, (c-d) PS/MbA/TiO_2 1 wt%, (e-f) PS/MbA/TiO_2 3 wt%, and (g-h) PS/MbA/TiO_2 7 wt%. The scale bar was 100 nm.

DOI: 10.60101/jarst.2023.253757

The HR-TEM was employed to demonstrate the morphology and crystalline structure of the PS hybrids. The sphere shape of the PS matrix was found with a few large particles due to the free radical polymerization, as seen in Figure 3a. Some TiO_2, moreover, was encapsulated in the PS hybrid. Figure 3b presents the Fast Fourier Transform (FFT) image of PS/MbA/TiO_2 7 wt% at magnification 500,000 which demonstrates the crystalline structure of TiO_2 (dot) and the amorphous structure of PS (ring).

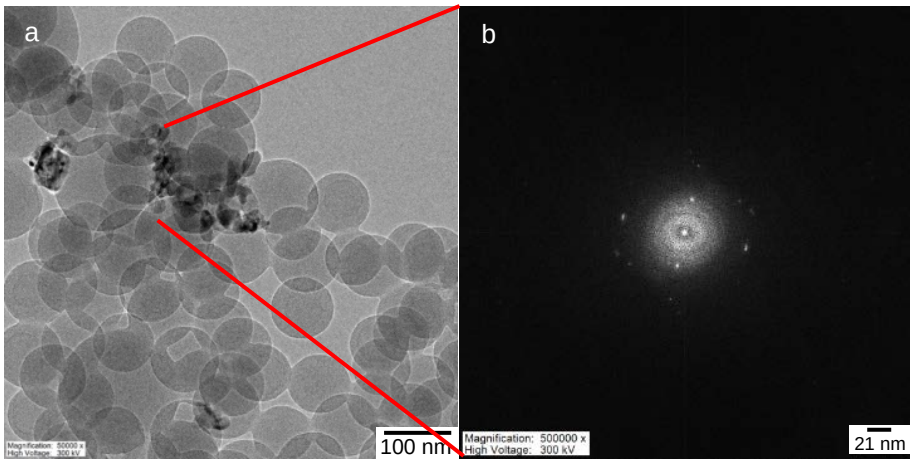

Figure 3 (a) HR-TEM image of PS/MbA/TiO_2 7 wt%, (b) Fast Fourier Transform (FFT) of PS/MbA/TiO_2 7 wt%.

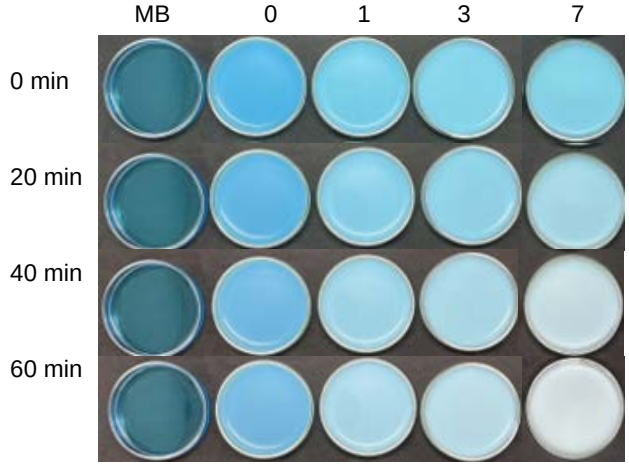

Figure 4 The discoloration of MB under UV light of PS/MbA/TiO_2 0-7 wt% in 1 h.

Table 2 The Hunter L*, a*, b* color scale for PS/MbA/TiO_2 0-7 wt% at 1 h.

PS/MbA/TiO_2 0 wt%	**L***	**a***	**B***
0min	53.59	-10.89	-25.78
60min	54.15	-10.26	-23.87
PS/MbA/TiO_2 1 wt%	**L***	**a***	**B***
0min	65.64	-15.38	-21.85
60min	65.51	-13.94	-19.67
PS/MbA/TiO_2 3 wt%	**L***	**a***	**B***
0min	69.89	-15.72	-19.00
60min	73.73	-11.24	-12.49
PS/MbA/TiO_2 7 wt%	**L***	**a***	**B***
0min	73.52	-14.88	-15.67
60min	73.73	-11.24	-12.49

The photocatalytic activity of PS/MbA/TiO_2 1-7 wt% was investigated by observing the discoloration of MB under UV light by measuring the Hunter L*, a*, b* color scales; for the "L*" scale a low number (0-50) presents dark and a high number (51-100) presents light. For the "a*" scale a positive number presents red and a negative number presents green. For the "b*" scale a positive number presents yellow and a negative number presents blue. Figure 4 demonstrates the discoloration of MB of PS/MbA/TiO_2 (0-7 wt%) for 1 h. It was found that the color of MB for PS/MbA was not changed due to the absence of a catalyze. For 1 wt% and 3 wt% of TiO_2 in PS hybrid, the MB color was slightly decreased, as seen in Figure 4. Table 2 shows the Hunter L*, a*, b* color scales for PS hybrids at 60 minutes. The result shows that in all the samples at 0 minute the L* was different due to the various amounts of white TiO_2. The negative b* scale was focused on due to the indicated blue color of MB. The b* value of the PS/MbA/TiO_2 7 wt% was higher than PS/MbA due to the photocatalytic activity of the TiO_2 hybrid, as shown in Table 2. Moreover, the a* value is presented as less negative than increasing the photocatalytic degradation. An increased amount of TiO_2 improved the photocatalytic efficiency. It concludes that the TiO_2 was successfully integrated with PS nanoparticles via mini-emulsion and showed photocatalytic properties.

CONCLUSION

A Polystyrene (PS)/nano-TiO_2 hybrid was successfully investigated by the mini-emulsion process. To study the effect of crosslinking agents on the photocatalytic properties of the hybrid, *N, N'*-methylenebis (acrylamide) (MbA) was added to the colloid system. The diameter, morphology, and photocatalytic properties of the samples were characterized and discussed. It was noticed that the 7 wt% TiO_2-PS/0.25 wt% MbA hybrid gives the highest photocatalytic properties. The FE-SEM confirmed the well-defined structure with a spherical shape and

DOI: 10.60101/jarst.2023.253757

network formation to improve the photocatalytic properties. The diameter and morphology of the PS/TiO_2 hybrid were in the range of 76 nm to 95 nm. In addition, the encapsulation of TiO_2 in the PS hybrid may result in an increase in the particle size of the hybrid. FT-IR spectroscopy was employed to analyze the functional group and bonding of the PS hybrid. The results showed that the absorption bands of the PS matrix were not affected by the encapsulated TiO_2 particles. It could be confirmed that the TiO_2 was encapsulated in PS hybrids. HR-TEM image of the PS/TiO_2 hybrid was studied to confirm the encapsulation of TiO_2 particles in the hybrid. It was noticed that the TiO_2 particles were successfully encapsulated in the PS/TiO_2 hybrid.

ACKNOWLEDGEMENT

This research was supported by The Science, Research and Innovation Promotion Funding (TSRI) (Grant no. FRB650070/0168). This research block grant was managed under Rajamangala University of Technology Thanyaburi (FRB65E0703E.1).

REFERENCES

1. Selvin TP, Kuruvilla J, Sabu T. Mechanical properties of titanium dioxide-filled polystyrene microcomposites. Mater Lett. 2004;58(3):281-9.
2. Sanchez C, Julián B, Belleville P, Popall M. Applications of hybrid organic-inorganic nanocomposites. J Mater Chem. 2005;15(3536): 3559-92.
3. Lebeau B, Sanchez C. Sol-gel derived hybrid inorganic-organic nanocomposites for optics. Curr Opin Solid State Mater Sci. 1999;4(1):11-23.
4. Kim TW, Yang Y, Li F, Kwan WL. Electrical memory devices based on inorganic/organic nanocomposites. NPG Asia Mater. 2012;4(6):e18-e.
5. Jordan J, Jacob KI, Tannenbaum R, Sharaf M, Jasiuk I. Experimental trends in polymer nanocomposites - a review. Mater Sci Eng. 2009;393:1-11.
6. Amin KF, Asrafuzzaman, Nahin AM, Hoque ME. 10 - Polymer nanocomposites for adhesives and coatings. In: Hoque ME, Ramar K, Sharif A, editors. Advanced Polymer Nanocomposites: Woodhead Publishing; 2022. p. 235-65.
7. Alam MR, Islam T, Repon MR, Hoque ME. 16 - Carbon-based polymer nanocomposites for electronic textiles (e-textiles). In: Hoque ME, Ramar K, Sharif A, editors. Advanced Polymer Nanocomposites: Woodhead Publishing; 2022. p. 443-82.
8. Wang X, Wang X, Meng A, Li Z, Xing J. Rapid, continuous, large-scale synthesis of ZnO/Ag hybrid nanoparticles via one-step impinging stream route for efficient photocatalytic and anti-algal applications. Mater Today Commun. 2022;30:103121.
9. Ferreira Soares DC, Domingues SC, Viana DB, Tebaldi ML. Polymer-hybrid nanoparticles: Current advances in biomedical applications. Biomed Pharmacother. 2020;131:110695.
10. Shetty A, Chandra S. Inorganic hybrid nanoparticles in cancer theranostics: understanding their combinations for better clinical translation. Mater Today Chem. 2020;18:100381.
11. Fitriani F, Bilad MR, Aprilia S, Arahman N. Biodegradable Hybrid Polymer Film for Packaging: A review. J Nat Fibers. 2023;20(1):2159606.
12. Lan Y, Lu Y, Ren Z. Mini review on photocatalysis of titanium dioxide nanoparticles and their solar applications. Nano Energy. 2013;2(5):1031-45.
13. Metanawin S, Metanawin T. Fabrication of hybrid polystyrene-titanium dioxide with enhanced dye degradation and antimicrobial properties: investigation of the effect of triethylene glycol dimethacrylate on photocatalytic activity. Polym Int. 2022;71(7):777-89.
14. Metanawin S, Sornsuwit N, Metanawin T. Miniemulsion polymerization technique enhancement: The photocatalysis of commercial rutile-TiO_2 hybrids with nano poly(methyl methacrylate). Polym-Plast Technol Mater. 2022; 61(1):56-68.
15. Metanawin T, Panutumrong P, Metanawin S. Synthesis of Polyurethane/TiO_2 Hybrid with High Encapsulation Efficiency Using One-Step Miniemulsion Polymerization for Methylene Blue Degradation and its Antibacterial Applications. ChemistrySelect. 2023;8(11):e202204522.
16. Sztorch B, Nowak K, Frydrych M, Leśniewska J, Krysiak K, Przekop RE, et al. Improving the Dispersibility of TiO_2 in the Colloidal System Using Trifunctional Spherosilicates. Materials. 2023;16(4):1442.
17. Akhtar S, Shahzad K, Mushtaq S, Ali I, Rafe MH, Fazal-ul-Karim SM. Antibacterial and antiviral potential of colloidal Titanium dioxide (TiO_2) nanoparticles suitable for biological applications. Mater Res Express. 2019;6(10):105409.
18. Tsang CHA, Li K, Zeng Y, Zhao W, Zhang T, Zhan Y, et al. Titanium oxide based photocatalytic materials development and their role of in the air pollutants degradation: Overview and forecast. Environ Int. 2019;125:200-28.

DOI: 10.60101/jarst.2023.253757

19. Fujishima A, Rao TN, Tryk DA. Titanium dioxide photocatalysis. J Photochem Photobiol C. 2000; 1(1):1-21.

20. Reddy KR, Hassan M, Gomes VG. Hybrid nanostructures based on titanium dioxide for enhanced photocatalysis. Appl Catal A: Gen. 2015;489:1-16.

21. Mironyuk IF, Soltys LM, Tatarchuk TR, Tsinurchyn VI. Ways to Improve the Efficiency of TiO_2-based Photocatalysts (Review). Phys Chem Solid State. 2020;21(2):300-11.

22. Rong Y, Chen HZ, Wu G, Wang M. Preparation and characterization of titanium dioxide nanoparticle/ polystyrene composites via radical polymerization. Mater Chem Phys. 2005;91(2):370-4.

23. Melgoza-Ramírez ML, Ramírez-Bon R. Microstructural comparison between PMMA-SiO_2 and PMMA-TiO_2 hybrid systems using Eu^{3+} as ion-probe luminescence. J Non-Cryst Solids. 2020;544:120167.

24. Erdem B, Sudol ED, Dimonie VL, El-Aasser MS. Encapsulation of inorganic particles via miniemulsion polymerization. Macromol Symp. 2000;155(1): 181-98.

DOI: 10.60101/jarst.2023.253757

Received: September 5, 2023 | Revised: December 12, 2023 | Accepted: December 13, 2023

Real-time vehicle detection system on the highway

Pisanu Kumeechai*

Engineering Department, Education Branch, Royal Thai Naval Academy, Samut Prakan 10270, THAILAND

*Corresponding author: Pisanu41984198@hotmail.com

ABSTRACT

Locating and classifying different types of vehicles is a vital element in numerous applications of automation and intelligent systems ranging from traffic surveillance to vehicle identification, with deep learning models now dominating the field of vehicle detection. However, vehicle detection in Bangladesh remains a relatively unexplored research lacuna. One of the main goals of vehicle detection is its real-time application, with "You Only Look Once" (YOLO) models proving to be the most effective. This paper compared real-time vehicle highway detection systems using YOLOv4, Faster R-CNN and SSD algorithms to determine the best performance. A vehicle detection and tracking system was also developed that improved highway safety. Vehicle trials compared the real-time performances of the YOLO, Faster R-CNN and SSD algorithms in detecting and tracking highway vehicles by measuring precision, recall, F1-score and operating speed. Models for each algorithm were constructed and each model was trained and tested, with performance measured using a confusion matrix. This statistical tool assessed the efficiency of the system using a prepared test dataset and evaluated the results using appropriate indicators such as real-time road lines, traffic signs and vehicle detection false positive rates. Results showed that the YOLOv4 algorithm outperformed Faster R-CNN and SSD in real-time vehicle detection and tracking on highways. YOLOv4 also processed the results more quickly and proved superior in detecting and tracking objects in real time. The Faster R-CNN algorithm gave high object detection, tracking accuracy and recall while reducing the number of locations needing detection, with the SSD algorithm providing high precision, recall and good image detection results.

Keywords: Real-time vehicle detection, YOLOv4, Faster R-CNN, SSD, Highway safety

INTRODUCTION

Real-time detection and tracking of vehicles on highways have benefited from high-profile developments in image processing over the past decade. Vehicle detection and tracking systems are critical for maintaining highway safety by quickly identifying obstructions and traffic violations to control vehicle speed limits in the event of accidents. Cutting-edge technologies such as image processing and deep learning are now utilized to develop vehicle detection and tracking systems, delivering safety and efficiency in highway traffic. This research proposed a real-time vehicle detection and tracking system using image processing and deep learning algorithms. The developed system detected vehicles moving on highways in real time and accurately tracked them using the three experimental algorithms YOLOv4, Faster R-CNN and SSD. Each algorithm has advantages and disadvantages. YOLO (You Only Look Once) [1-3] is a high-speed algorithm that works in split-image mode (single-stage), making it possible to detect objects quickly and YOLO can detect larger objects better than other algorithms. However, YOLO has difficulties detecting small objects with oblique details, as shown in figure 1. The hallmark of Faster R-CNN [4-6] is accuracy and efficiency in simultaneously detecting multiple objects with oblique details. This algorithm is suitable for tasks that require detecting and identifying multiple objects in a single image. One disadvantage of Faster R-CNN is its slow performance, generated by a complex workflow. The area containing the object must first be extracted before predicting the memory required to detect the object. Faster R-CNN is slower than algorithms that do not have to perform this step, such as YOLO. The SSD (Single Shot MultiBox Detector) algorithm [7] can detect objects moving at high speed using a split image function that works in real time. This algorithm uses a data pyramid to detect multiple small objects in the image simultaneously. However, the SSD algorithm has difficulty detecting large objects with oblique details, object movements, or changes in perspective.

Several recent studies have addressed the problem of vehicle detection using aerial imagery [8-11]. Previously [12], we compared YOLOv3 with Faster R-CNN for vehicle detection from aerial imagery using a small dataset of low-altitude UAV images collected

DOI: 10.60101/jarst.2023.254011

JOURNAL OF APPLIED RESEARCH ON SCIENCE AND TECHNOLOGY

on the premises of Prince Sultan University. Imaging altitude plays an important role in accuracy detection. Advanced performance indicators include Intersection over Union (IoU) and mean Average Precision (mAP). This article considers several datasets with different configurations and presents a comprehensive comparison analysis between three state-of-the-art approaches: Faster R-CNN, YOLOv3 and YOLOv4. The challenges faced by photo physics were discussed in ref [13]. Problems in airborne vehicle detection include small objects and complex backgrounds. These problems were solved using neural networks. Other research problems when applying deep learning techniques to aerial imagery have been discussed in various contexts, including object detection and classification [14,15], semantic segmentation [16-18] and generative adversarial networks (GAN) [19]. Jiao et al. [20] surveyed many object detectors and reported results on a COCO dataset [21]. This study focused on an in-depth comparison of three recently published algorithms representing two main types of object detectors, Faster R-CNN [22] (a two-stage detector) and YOLOv3 [23] and YOLOv4 [24] (single-step detectors), to investigate a wide range of hyperparameters and evaluate the impact of size and characteristics of aerial view datasets.

This paper proposes a method that obtains the driving area of a vehicle through road line detection and captures the main color information of the motion area and non-motion area of a moving vehicle. The experimental algorithms YOLOv4, Faster R-CNN and SSD were used to detect and track the vehicles. The vehicle detection and tracking model is shown in figure 2. The detector is responsible for detecting the vehicles in each frame, while the tracker correlates vehicles in adjacent frames to form a complete vehicle trajectory.

The rest of this paper is organized as follows: Section II briefly reviews the existing object detection algorithms used for vehicle detection and tracking. Section III explains the method that applied in this paper. Section IV explains the use of a confusion matrix for measurement. The experiments and comparative analyses to evaluate the state-of-the-art methods are detailed in Section V and the conclusions drawn are presented in Section VI.

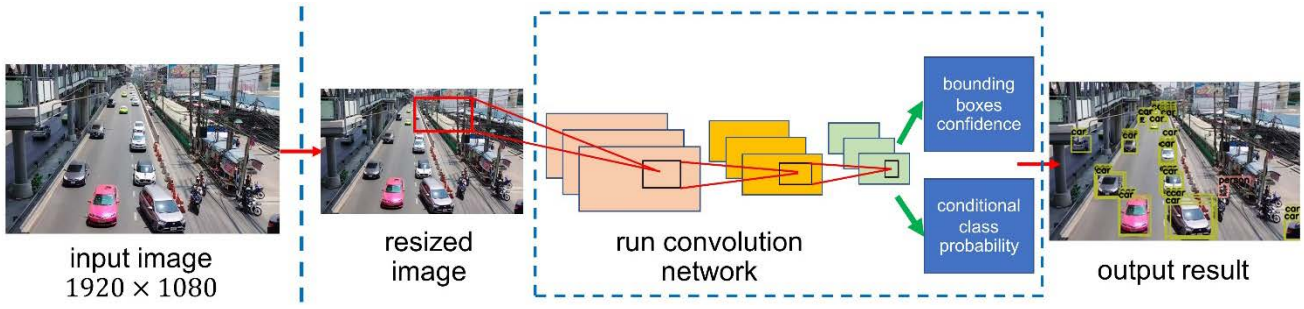

Figure 1 Working principle of YOLO.

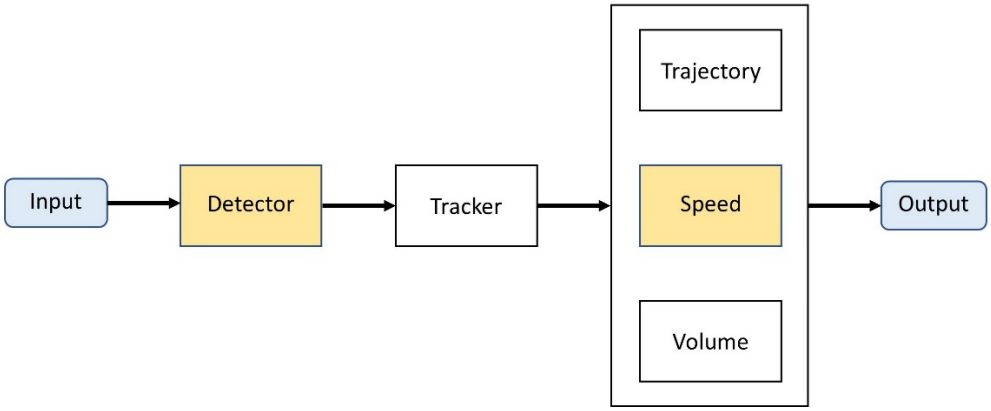

Figure 2 The detection-based vehicle tracking model.

MATERIALS AND METHODS

Research scope

The research objective was to compare the YOLOv4, Faster R-CNNF and SSD algorithms to determine the best performance and develop a vehicle detection and tracking system to improve highway safety. Digital cameras with image file sizes 640 by 840 and 50 frames per second were used to collect the information. The image dataset detected images from normal, well-lit surroundings and divided 1000 images into 800 training images and 200 testing images, representing different vehicles such as cars, trucks, motorcycles and buses to evaluate and measure the effectiveness of the system in detecting and tracking vehicles in actual traffic conditions.

The trial compared the performance of YOLO, Faster R-CNN, and SSD in detecting and tracking highway

DOI: 10.60101/jarst.2023.254011

vehicles by measuring precision, recall, F1-score, and operating speed. The accuracy and performance of each algorithm were assessed in the same situation.

This real-time vehicle detection and tracking system on highways used YOLO, Faster R-CNN and SSD algorithms and tuning parameters such as detector resolution to achieve a high-performance system in a highway environment for real-world use.

Related literature

1. Vehicle detection

Real-time detection of vehicles on highways represents an important field of study with benefits in many areas, including the prevention of road accidents. Highway vehicle detection and tracking is an integral part of the road safety system, covering events on the highway, such as changing lanes. Traffic control or vehicle problem detection to reduce road accidents using traffic management. Highway vehicle detection and tracking systems effectively manage vehicle speed while also controlling highway lighting. Data collection from highway vehicle detection and tracking was analyzed to gain insights into traffic trends, risks and factors affecting highway safety as a research area with potential for further development. Copious previous research has addressed these issues. Njayou Y, [25] used Convolutional Neural Network (CNN) image processing techniques for traffic sign classification and object detection with Faster R-CNN and YOLOv4 algorithms. The Faster R-CNN test results gave a mean average precision (mAP) of 43.26% at 6 frames per second (fps), which was unsuitable for real time use. By contrast, YOLOv4 yielded mAP of 59.88% at 35 fps as a suitable model for real-time traffic sign detection. Annam F, et al. [26] proposed a fast and accurate real-time vehicle detection method using deep learning techniques for unrestricted environments. They detected vehicles in the model image and real environment using deep neural networks as the main tool. The dataset consisted of vehicle images taken in various environments and was divided into training and test sets. The proposed detection method gave high speed and accuracy. The concept of the Faster R-CNN model used the feature extraction technique and depth processing model. Results demonstrated the efficiency of the proposed method in terms of vehicle detection accuracy and short image processing time.

Bochkovskiy A, et al. [27] proposed the YOLOv4 algorithm as a Single Shot Detector (SSD) object detection model that focused on providing optimal speed and accuracy for object detection using a combination of techniques to improve YOLOv3 and the existing models. They added depth and used new techniques to increase the efficiency and accuracy of the system. Results demonstrated that YOLOv4 detected objects in images with high speed and accuracy. Ren S, et al. [28] used real-time Region Proposal Networks (RPN) in the Proposal Generation process by combining CNN and RPN into a single structure, enabling fast and highly efficient rapid object detection. This new concept created images based on deep neural networks and then used these images for object detection. Results demonstrated the high speed and accuracy of Faster R-CNN in object detection. Liu W, et al. [29] proposed an SSD (Single Shot MultiBox Detector) algorithm using rapid duplex object detection. This method combined the detection and ranking of several class objects into a single structure, enabling fast and highly efficient detection of objects that did not require new proof procedures.

2. Vehicle tracking

CNN-based multi-target vehicle tracking technology has recently received increased attention [30]. Bewley et al. [31] used the Faster R-CNN algorithm as the target detector and proposed a simple online and real-time tracking (SORT) algorithm to track multiple targets simultaneously based on the Kalman filter and Hungarian matching algorithm, while Wojke N, et al. [32] considered both the movement characteristics and the appearance of the target. They proposed an improved DeepSORT algorithm where the appearance features of the target were extracted through the CNN model after target detection by the detector. Later, Wang Z, et al. [33] further improved the complexity of the DeepSORT algorithm by developing the JDE algorithm. This directly exported the target location and appearance features into the detection network using RetinaNet to embed an instance-level vehicle feature extraction network in the detector model, while Lu Z, et al. [34] created a RetinaTrack multi-target vehicle tracking model to combine vehicle movement and appearance characteristics for data association.

Method

YOLOv4 is a high-speed, high-precision rapid-duplex object detection model that uses deep neural networks (Convolutional Neural Network) to detect objects in images YOLOv4 includes Backbone: CSPDarknet53, Neck: SPP, PAN, Head: YOLOv3 and uses Bag of Freebies (BoF) and Bag of Specials (BoS) to optimize the model. BoF includes CutMix and Mosaic data augmentation, DropBlock regularization and Class label smoothing, while BoS includes Mish activation, Cross-stage partial connections (CSP), Multi-input weighted residual connections (MiWRC), SPP-block, SAM-block, PAN path-aggregation block and DIoU-NMS to increase model precision and speed.

YOLOv4's object detection and tracking algorithm uses a CNN (Convolutional Neural Network) structure that comprises the backbone. CSPDarknet53 is used as the core structure of the YOLOv4 model to extract image features. Neck uses SPP (Spatial Pyramid Pooling) and PAN (Path Aggregation Network) to increase object detection accuracy, and the head uses YOLOv3 (anchor-based) as the head of the YOLOv4 model to perform object detection.

DOI: 10.60101/jarst.2023.254011

To perform object detection and object tracking functions, YOLOv4 uses an improved CNN structure over YOLOv3 with the addition of Bag of Freebies (BoF), a model modification technique that is not a core part of the YOLOv4 model but enhances model accuracy. BoF includes CutMix and Mosaic data augmentation, DropBlock regularization, Class label smoothing, and Bag of Specials (BoS) to increase accuracy.

In YOLOv4, the input image is split into a grid S×S, with each grid cell in charge of vehicle detection. B bounding boxes are placed in each grid cell and the network then outputs an offset value for the bounding box and class probability. The bounding boxes are chosen and the vehicle in the image is then located using those with a class probability with a particular threshold (Figure 3).

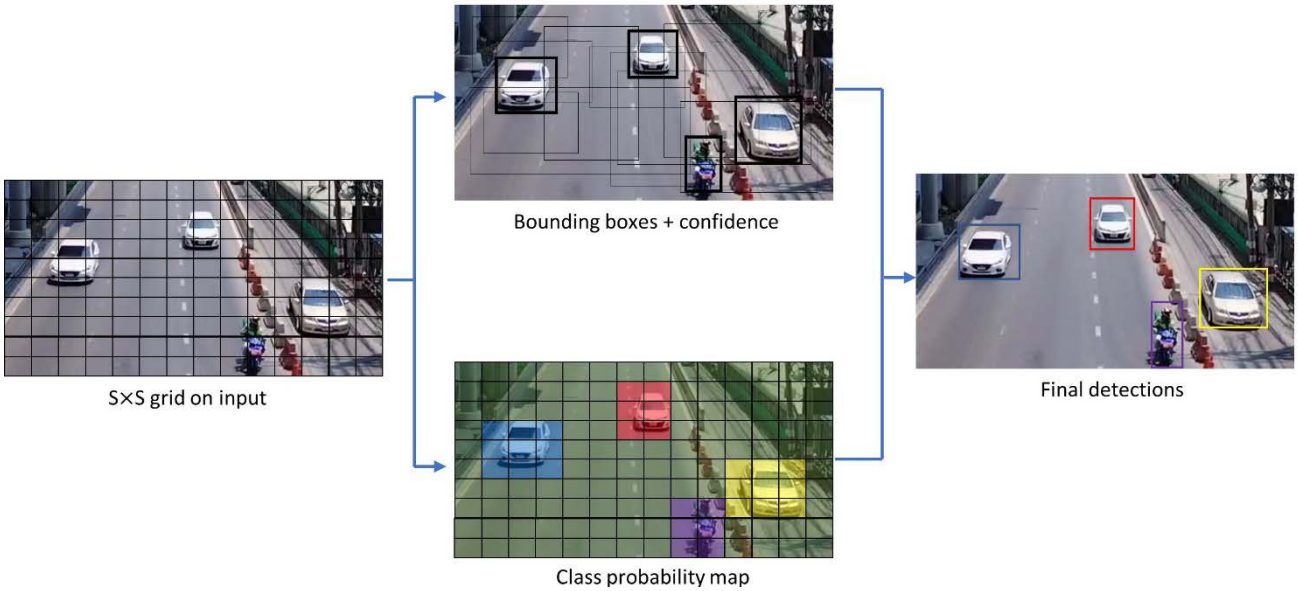

Figure 3 Illustration of YOLOv4 framework.

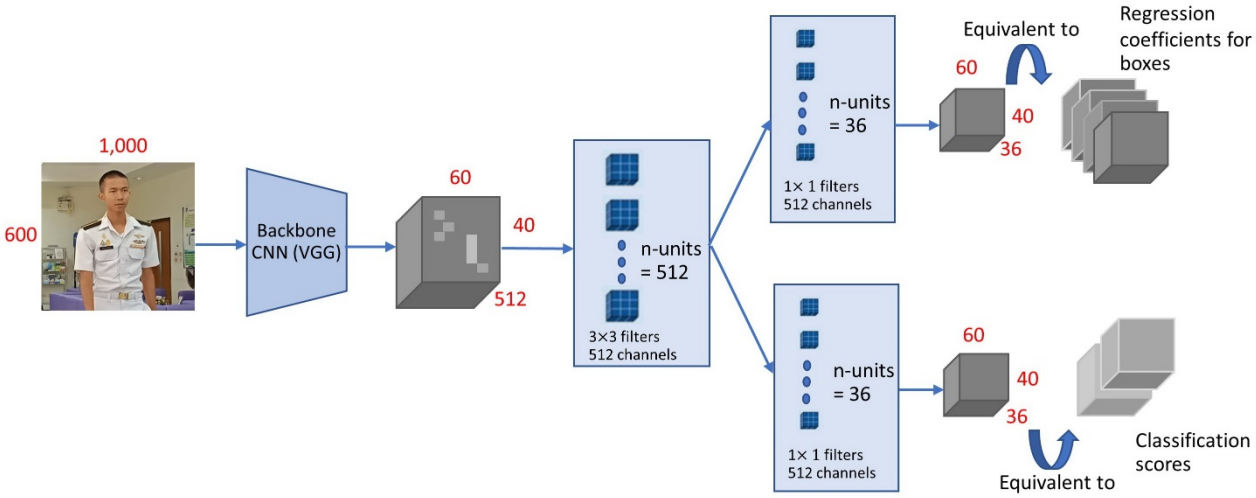

Figure 4 Faster R-CNN architecture.

YOLOv4 is a fully convolutional network with 110 convolution layers comprising 66 as 1 × 1 and 44 as 3 × 3. The input layer has a 3 × 3 convolution layer with 19 32 filters. This thesis used input size starting at 416 × 416 with 3 channels (RGB). The output layer is a 1 × 1 convolution layer with a stride and padding size of 1. The output layer has 33 filters and uses CSPDarknet53 as the backbone, SPP and PAN for the Neck, with the head of YOLOv4 used as the head in YOLOv4. Mini-batch gradient descent with momentum is used for optimization. CSPDarknet-53 extracts deep features of the input images, while SPP efficiently increases the receptive field, PANet extracts features across multiple scales and the heads detect objects. A linear activation function is used for the final layer, with input starting size 416 × 416 with 3 channels (RGB), YOLOv4 has more than 60M parameters.

Faster R-CNN [36] (Region-based Convolutional Neural Network) is an algorithm designed to detect objects and track images quickly with high accuracy (Figure 4). The algorithm can be divided into three parts as follows:

1) Faster R-CNN uses a Region Proposal Network (RPN) network to create a region proposal

DOI: 10.60101/jarst.2023.254011

as a region that may have straightforward objects. The pre-trained feature map is used as an assembly.

2) Region of Interest (RoI) pooling. Upon receiving an image proposal from an RPN, Faster R-CNN uses RoI pooling to adjust the size and position of the image proposal to fit the deep neural network for tracking the object.

3) Region Classification and Regression. The last step of the Faster R-CNN deep neural network classifies objects and adjusts the size and position of the bounding boxes found in the proposed segments of the image. Object classification is the process used to decide the type of object while adjusting the size and position of the squares to improve object detection accuracy.

Faster R-CNN is the most preferred and used version of the R-CNN family, using a particular selection of search algorithms for proposing regions and taking only 1 or 2 seconds per image to run the CPU computation. Faster R-CNN uses Region Proposal Networks (RPNs) to generate region proposals, reducing generation time from seconds to milliseconds per image.

In FASTER R-CNN,

- RPN generates bounding boxes as a rectangular box that surrounds an object and specifies its position, class (e.g. car, person) and confidence (how likely it is to be at that location).
- In this stage, CNN is used to generate features of these objects. Region proposal is not performed on the original image but on the final feature image, which is then input into the ROI pooling (Region of Interest Pooling fixes image size requirements for object detection).
- The output from the ROI pooling layer has a size of N, 7, 7, 512, where N is the number of proposals from the region proposal algorithm. After passing those ROI pooling outputs through two fully connected layers, the features are fed into the sibling classification and regression branches.
- A classification layer is present to determine the object's class.
- Finally, a regression layer is used to ensure that the coordinates of the bounding boxes are more precise, leaving no gaps for errors.
- Anchors are introduced in RPN to deal with different scales and aspect ratios of the objects. An anchor is positioned at each sliding location of the convolutional maps and at the center of each spatial window. Each anchor is associated with a scale and an aspect ratio.

SSD (Single Shot MultiBox Detector) [37] is a method of object detection and image tracking using a single deep neural network, which is shown in figure 5. The SSD divides the regions of the bounding boxes into a set of default boxes. The aspect ratio and scales differ for each feature map location. To hold objects of different sizes and shapes, the network generates a score for factoring each object category in each initial box and generates adjustments to make the box fit the shape of the object. Predictions from multiple property maps with different resolutions are used to handle objects of different sizes. SSDs have been tested, with results proving that increasing the number of carefully selected default boxes greatly improves object detection and tracking performance. SSD is a highly efficient and easy-to-use object detection and tracking model.

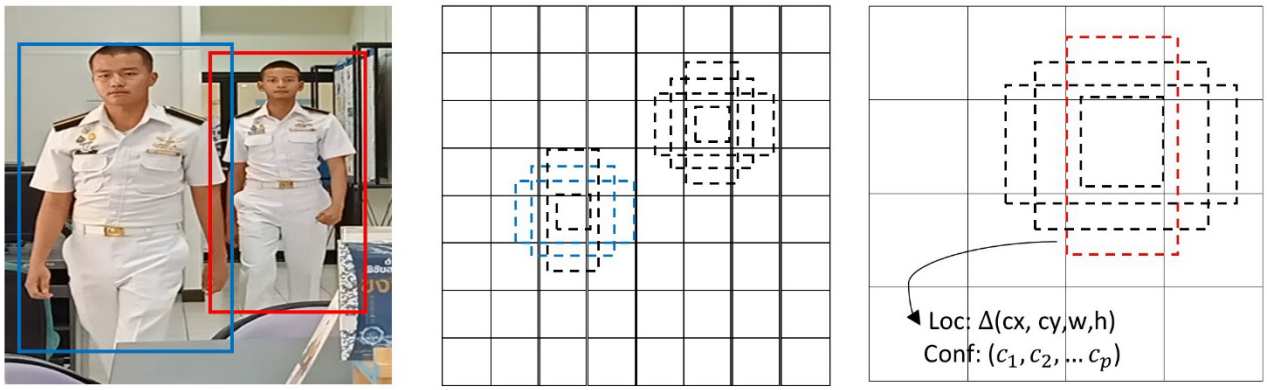

(a) Image with GT boxes (b) 8 × 8 feature map (C) 4 × 4 feature map

Figure 5 SSD framework.

(a) SSD only needs an input image and ground truth boxes for each object during training. A small set (e.g. 4) default boxes of different aspect ratios is evaluated in a convolutional fashion at each location in several feature maps with different scales (e.g. 8×8 and 4×4 in figure 5 (b) and (c)).

The key difference between training an SSD and a typical detector that uses region proposals is that ground truth information must be assigned to specific outputs in the fixed set of detector outputs. Some versions also require training in YOLO [38] and the region proposal stage of Faster R-CNN [39] and MultiBox [40]. Once this assignment is determined, the loss function and backpropagation are applied end-to-end. Training also involves choosing the set of default

DOI: 10.60101/jarst.2023.254011

JOURNAL OF APPLIED RESEARCH ON SCIENCE AND TECHNOLOGY

boxes and scales for detection as well as hard negative mining and data augmentation strategies.

Training Objective. The SSD training objective is derived from the MultiBox objective [23] but is extended to handle multiple object categories. Let $x_{ij}^{p} = \{1,0\}$ be an indicator to match the i-th default box to the j-th ground truth box of category p. In the matching strategy above, $\sum_i x_{ij}^{p} \geq 1$. The overall objective loss function is a weighted sum of the localisation loss (loc) and the confidence loss (conf) such that:

$$L(x,c,l,g) = \frac{1}{N}\left(L_{conf}(x,c) + \alpha L_{loc}(x,l,g)\right) \quad (1)$$

where N is the number of matched default boxes and the localization loss is the Smooth L1 loss [41] between the predicted box (l) and the ground truth box (g) parameters. Like Faster R-CNN [42], we regress to offsets for the center of the bounding box and its width and height. Our confidence loss is the SoftMax loss over multiple class confidences (c) and the weight term α is set to 1 by cross-validation.

4. Vehicle tracking method

Section III describes the Simple Online and Real-time Tracking (SORT) algorithm used to track an individual vehicle. SORT is a real-time and online tracking algorithm integrated with the Kalman filter and the Hungarian algorithm, with an accuracy comparable to state-of-the-art online trackers while supporting higher update rates. The state space of each vehicle is modeled as follows: $[x,y,s,r,\dot{x},\dot{y},\dot{s}]^{T}$, where (x, y) is the central location of the bounding box of the vehicle, s and r represent the scale (area) and the aspect ratio of the bounding box respectively and $\dot{x}$ and $\dot{y}$ are the velocity elements. When detection is associated with a vehicle, the detected bounding box is used to update the state of the vehicle. The location of the new bounding box for each vehicle is predicted based on the Kalman filter. SORT uses the intersection-over-union (IOU) between each incoming detection and all predicted bounding boxes of the existing vehicle. These values are then used to populate a cost matrix solved by a Hungarian algorithm to assign each track an appropriate detection. The vehicle tracking procedure of SORT is shown in figure 6.

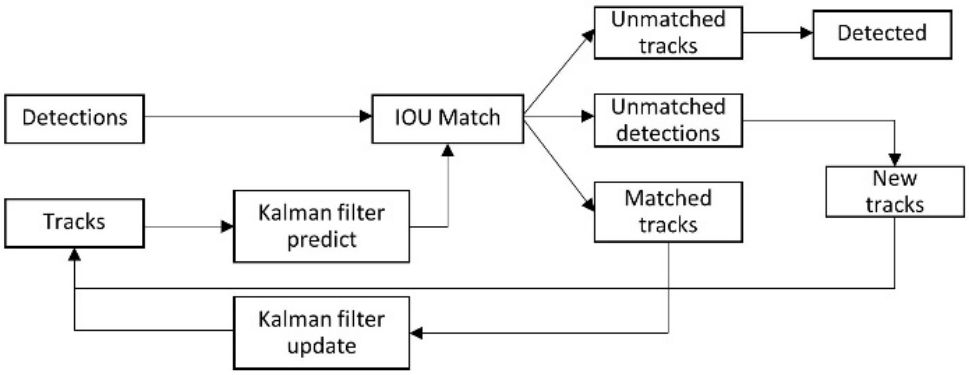

Figure 6 Vehicle tracking procedure of SORT.

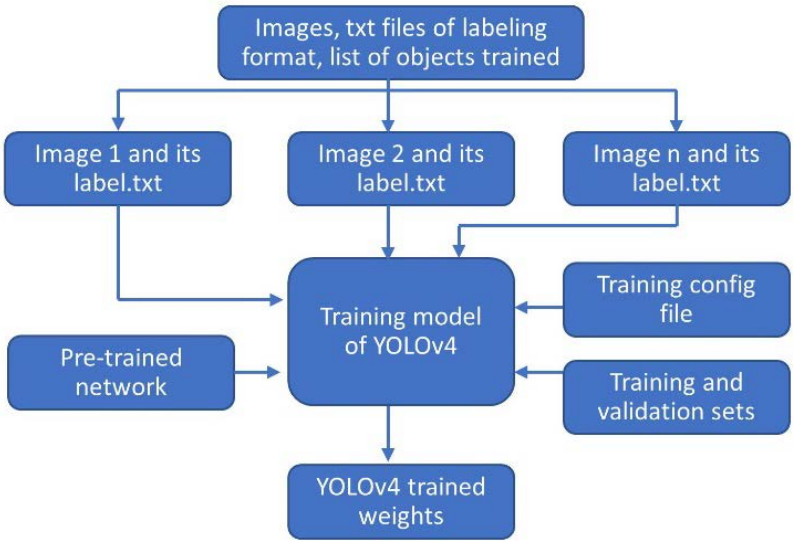

Figure 7 Training diagram of YOLOv4 on our dataset.

Confusion matrix theory

Confusion matrix theory is a statistical tool used to evaluate the effectiveness of classification systems, especially binary systems, by considering the predicted result against the ground truth of the sample data (rows) and the actual values (columns). Each cell in the confusion matrix represents the number of examples

DOI: 10.60101/jarst.2023.254011

correctly or incorrectly classified for each group of a sample type. The classification results can be divided into four parts, according to Table 1.

Table 1 Confusion matrix.

	Predicted positive	**Predicted negative**
Actual positive	True Positive (TP)	False Negative (FN)
Actual negative	False Positive (FP)	True Negative (TN)

The variables used in the confusion matrix are defined below.

1) True Positive (TP) is the number of samples predicted to be positive and truly positive.

2) False Positive (FP) is the number of samples predicted to be negative but are actually positive.

3) False Negative (FN) is the number of samples predicted to be positive but are actually negative.

4) True Negative (TN) is the number of samples predicted to be negative and true negative.

The TP, FP, FN and TN values were used to calculate system efficiency, with the important equations 2, 3 and 4 shown below.

$$Precision = \frac{TP}{(TP + FP)} \quad (2)$$

$$Recall = \frac{TP}{(TP + FN)} \quad (3)$$

$$F1\ score = 2 \times \frac{(Precision \times Recall)}{(Precision + Recall)} \quad (4)$$

$$mAP = \frac{1}{Q}\sum_{q=1}^{Q} AP_q \quad (5)$$

Precision is the accuracy of forecasting.

Recall is the accuracy of positive detection.

The F1 score is the mean of precision and recall and is used to evaluate the performance of a particular binary classification system.

The mAP is the average value of AP for each class.

Research process

This research used the following steps to compare the performance of YOLOv4 (Figure 7). Faster R-CNN and SSD real-time highway vehicle detection and tracking algorithms.

1) Set the objectives

The research objective was to develop a highway detection and tracking system to enhance the efficiency and accuracy of vehicle detection and increase road safety.

2) Create a dataset

Building the suitable dataset for training and testing the system involved taking photographs or videos of the highway vehicles being tracked to increase detection accuracy. The dataset was divided into two parts the training dataset and the testing dataset.

3) Train and test the model

A built-in dataset was employed to train and test the models used in vehicle detection and tracking using the YOLOv4, Faster R-CNN and SSD algorithm training methods on the defined dataset.

4) Measure the performance

The performance was measured using a confusion matrix after successfully training and testing the models for each algorithm. This statistical tool assessed the efficiency of the system using the prepared test dataset and evaluated the results using appropriate indicators such as detection rate and false positive rate.

RESULTS AND DISCUSSION

The dataset and evaluation index

Deep learning-based vehicle object detection algorithms learn features from data samples and the dataset must be representative. The dataset contained real image data collected from scenes such as urban areas, rural areas and highways. Each image contained up to 15 cars and 30 pedestrians, with various degrees of occlusion and truncation. The images reflected a variety of complex situations, such as multiple trucks and cars appearing in the same image or multiple trucks, vans and cars appearing in the same image under different lighting conditions, road environments and road conditions. For the peculiar application of vehicle object detection, the Car, Van, Truck, Pedestrian, Pedestrian (sitting), Cyclist, Tram and Misc classes in the dataset were converted to Car, Van, Truck and Other classes. The 1000 labeled images in the dataset were divided into a training set and a testing set at ratio 6:4. To validate the generalization ability of the algorithm, a vehicle dataset was established through online collecting and real-scene shooting. Figure 8 shows some samples from the dataset.

Experimental setup

The experiment was run in a Python environment using Google Collaboratory. The average usable memory of the machine was 8 GB and the average disk space used was 256 GB. The sample images were randomly split into 60% for training, 20%, for validation and 20% for testing. The batch size was 16 for all the models because smaller batches are noisy and can reduce generalization errors. Model Checkpoints were used to save the model with the best validation accuracy during the process. The convergence of the models depended on many parameters and the size of the weight parameters. Using the Early Stopping technique, the total time required to complete the training of all three models was more than 500 hours.

Research results

Small batch random gradient descent was used for training optimization and a set of values that improved

DOI: 10.60101/jarst.2023.254011

JOURNAL OF APPLIED RESEARCH ON SCIENCE AND TECHNOLOGY

the network quality was selected. The momentum parameter was set to 0.8, the weight attenuation coefficient was set to 0.0001 and the initial learning rate was set to 0.001. Due to memory limitations, the batch was set to 64 and the subdivision was set to 64. Two indicators were considered to verify the performance of each vehicle detection algorithm detection accuracy and detection efficiency. Comparative experiments were conducted to prove that each part of the modified YOLO was effective.

Real-time detection and tracking of vehicles on highways were conducted using YOLOv4, Faster R-CNN and SSD algorithms to determine the best performance, with research findings summarized in Tables 2 and 3.

Table 2 Confusion Matrix Measurement Results.

	True Positive (TP)	False Positive (FP)	False Negative (FN)	True Negative (TN)
YOLOv4	90	10	5	895
Faster R-CNN	85	15	7	893
SSD	88	12	8	892

Table 3 Precision, Recall and F1-score.

	Average IoU	Precision	Recall	F1-score
YOLOv4	93.17%	0.900	0.947	0.923
Faster R-CNN	85.86%	0.850	0.923	0.885
SSD	80.11	0.880	0.916	0.898

Detecting image objects was assigned into four categories. Each category had a True Positive (TP) value as the number of objects that were correctly detected and tracked by category, False Positive (FP) value as the number of objects that were detected but not tracked or incorrectly tracked by category, False Negative (FN) value as the number of objects that were present but were not detected or incorrectly detected as a category and True Negative (TN) value as the number of objects that were not objects in a category and were not detected as objects in a category (Table 2). YOLOv4 gave a good performance with the highest value of True Positive (TP) and the lowest value of False Negative (FN). The TP, FP, FN and TN values were then used to calculate the Precision, Recall and F1-score, including other values related to the image detection and tracking system performance, as shown in Table 3.

Real-time detection and tracking results of highway vehicles are shown in Table 3. In table 3, the YOLOv4 algorithm had Precision of 0.900, Recall of 0.947 and F1-score of 0.923, indicating good performance in detecting all images. The Faster R-CNN algorithm had Precision of 0.850, Recall of 0.923 and F1-score of 0.885, indicating good performance in image detection. The Faster R-CNN algorithm had the highest Recall but the Precision and F1-scores were lower than YOLOv4. The SSD algorithm had Precision of 0.880, Recall of 0.916 and F1-score of 0.898, indicating good performance in image detection. The SSD algorithm had relatively high Precision and Recall and a high F1-score. When comparing the Precision, Recall and F1-scores of all three algorithms, the YOLOv4 algorithm gave the best performance in image detection.

The faster R-CNN algorithm and SSD algorithm showed similar performances but SSD had higher precision and recall. The real-time vehicle detection and tracking system on the highway is shown in figure 8.

Figure 8 Real-time vehicle detection and tracking system.

In Table 3, when the IoU threshold of the YOLOv4 model trained on the Royal Thai Naval Academy 1000 dataset was changed from 0.5 to 0.75, the average IoU was 47.08%. The F1-Score of YOLOv4 was 0.923 when the IoU threshold was 0.5 but was relatively biased, with Faster R-CNN and SSD as 0.885 and 0.898, respectively, when the IoU threshold was 0.75. Thus, some classes were better learned than others. As shown in Table 3, after the feature extraction network of the original YOLOv4 was replaced by the skip-connection deep residual feature extraction network, in Table 3, the recall and mAP increased from Faster R-CNN of 7.31% and from SSD of 13.06%, respectively, because the feature extraction network proposed in this paper reused the features extracted from the input feature.

Additional experiments were conducted with different values of learning rates (10^{-5}, 10^{-4}, 10^{-3} and

DOI: 10.60101/jarst.2023.254011

10^{-2}) for each of the main algorithms (Faster R-CNN with Inception-v2, Faster R-CNN with Resnet 50 and YOLOv4 with input size 608 × 608) to measure the sensitivity of each algorithm to the learning rate hyperparameter. A learning rate of 10^{-3} yielded the best performance in most cases but on the Stanford dataset Faster R-CNN with Inception-v2 and YOLOv4 gave better results at lower learning rates (10^{-4} and 10^{-5}, respectively). A learning rate of 10^{-2} gave poor results in all cases except for YOLOv4 on both datasets and for Resnet50 on the dataset. A learning rate of 10^{-1} was also tested but this led to a divergent loss. These results highlighted the importance of testing different learning rate values when comparing object detection algorithm performances. Results in Table 3 and Table 4 confirm the superior performance of YOLOv4 and Faster R-CNN when the learning rate was well chosen.

Table 4 Detailed results of different configurations of YOLOv4, SSD and Faster R-CNN, on the Stanford dataset.

Algorithm	Feature Extraction	Input Size
YOLOv4	CSPDarknet-53	320 × 320 (fixed)
YOLOv4	CSPDarknet-53	416 × 416 (fixed)
YOLOv4	CSPDarknet-53	608 × 608 (fixed)
Faster R-CNN	Inception v2	600 × 816 (variable)
Faster R-CNN	Inception v2	608 × 608 (fixed)
Faster R-CNN	Resnet50	600 × 816 (variable)
SSD	Darknet-53	320 × 320 (fixed)
SSD	Darknet-53	416 × 416 (fixed)
SSD	Darknet-53	608 × 608 (fixed)

For YOLOv4, one-stage detectors performed well over a dense selection of potential object locations, enabling whole image detection in a single forward propagation. Two-stage detectors such as Faster R-CNN are generally more accurate than their one-stage counterparts but fast speeds and low memory costs render one-stage detectors more suitable for real-time applications such as autonomous driving.

CONCLUSION

YOLOv4 outperformed Faster R-CNN and SSD in real-time vehicle detection and tracking on highways because YOLOv4 processed the results faster and was ideal for detecting and tracking objects in real time, as a key feature in detecting high-speed highway vehicles. YOLOv4 offered high object detection and tracking accuracy by precisely identifying the location and size of the vehicle. This is important for managing and improving highway traffic. However, in some cases, YOLOv4 encountered difficulty or finely detailed objects, causing some detection discrepancies. Therefore, YOLOv4 may experience reduced performance in challenging environments.

Faster R-CNN had high object detection, tracking accuracy and recall. The system detected and tracked a wide range of objects in the test dataset by creating region proposals that accurately determined object boundaries. This reduced the number of locations that needed to be detected. However, the Faster R-CNN algorithm was executing slower because it had to create region proposals before performing object detection. This resulted in uptime that could limit fast deployment in environments that require immediate response.

The SSD algorithm gave high precision and recall and good image detection performance, with a high ability to detect small objects such as small rings or turn signals. However, limitations of SSD included accuracy in detecting large objects with fine detail.

Recommendations to improve real-time detection and tracking of vehicles on highways using YOLOv4 include: 1. Increase the amount of training data used to train YOLOv4 to improve the accuracy and detection of the system 2. Experimentally tune YOLOv4 parameters such as detection thresholds or filters to suit the dataset and objects to be detected 3. Increase YOLOv4 resolution by adding or enhancing model layers to detect and track objects in more detail.

Suggestions for further research

Real-time detection and tracking of vehicles on highways using the YOLOv4 algorithm can be improved as follows:

1) Customize and add training data: Increase the amount of training data used to train YOLOv4 to improve the accuracy and detection of the system. Consider adding information such as different weather conditions and lighting to improve system operation.

2) Parameter customization hyperparameter tuning. Experimentally tune YOLOv4 parameters such as detection thresholds or filters to suit the dataset and objects to be detected. Parameter tuning may achieve better results in vehicle detection and tracking.

3) Model refinement: Consider increasing the resolution in YOLOv4 models by adding or enhancing model layers to detect and track objects in more detail. For example, overlapping vehicle sections can be detected and tracked.

ACKNOWLEDGEMENT

This research was successfully accomplished with the assistance of the Engineering Department, Education Branch, Royal Thai Naval Academy, which provided both equipment and research facilities.

REFERENCES

1. Redmon J, Divvala S, Girshick R, Farhadi A. You only look once: Unified, real-time object detection. In Proceedings of the IEEE conference on computer

DOI: 10.60101/jarst.2023.254011

vision and pattern recognition. 2016;2016:779-788. doi: 10.1109/CVPR.2016.91.

2. Redmon J, Farhadi A. YOLOv3: An incremental improvement. arXiv preprint arXiv. 2018; doi: 10.48550/arXiv.1804.02767.
3. Bochkovskiy A, Wang CY, Mark Liao HY. YOLOv4: Optimal speed and accuracy of object detection. arXiv preprint arXiv. 2020;2004.10934.
4. Ren S, He K, Girshick R, Jian Sun. Faster R-CNN: Towards real-time object detection with region proposal networks. In Advances in neural information processing systems. 2015;91-9.
5. Girshick R. R-CNN F. In Proceedings of the IEEE international conference on computer vision. 2015; 2015:1440-8.
6. Ren S, He K, Girshick R, Sun J. Faster R-CNN: Towards real-time object detection with region proposal networks. IEEE Transactions on Pattern Analysis and Machine Intelligence. 2017;39(6): 1137-49.
7. Liu W, Anguelov D, Erhan D, Szegedy C, Reed S, Fu CY, et al. Berg. SSD: Single shot multibox detector. IEEE Transactions on Pattern Analysis and Machine Intelligence. 2018;40(4):817-23.
8. Li X, Luo M, Ji S, Zhang L, Lu M. Evaluating generative adversarial networks-based image-level domain transfer for multi-source remote sensing image segmentation and object detection. Int J Remote Sens. 2020;41:7327-51. doi:10.1080/01431161.2020.1757782.
9. Liu K, Mattyus G. Fast multiclass vehicle detection on aerial images. IEEE Geosci Remote Sens Lett. 2015;12:1938-42. doi: 10.1109/LGRS.2015.2439517.
10. Audebert N, Le Saux B, Lefèvre S. Segment-before-detect: Vehicle detection and classification through semantic segmentation of aerial images. Remote Sens. 2017;9:368. doi:10.3390/rs9040368.
11. Ma B, Liu Z, Jiang F, Yan Y, Yuan J, Bu S. Vehicle detection in aerial images using rotation-invariant cascaded forest. IEEE Access. 2019;7:59613-23.
12. Benjdira B, Khursheed T, Koubaa A, Ammar A, Ouni K. Car Detection using Unmanned Aerial Vehicles: Comparison between Faster R-CNN and YOLOv3. In Proceedings of the 2019 IEEE 1st International Conference on Unmanned Vehicle Systems-Oman (UVS), Muscat, Oman, 5-7 February 2019; p.1-6.
13. Xi X, Yu Z, Zhan Z, Tian C, Yin Y. Multi-task cost-sensitive-convolutional neural network for car detection. IEEE Access. 2019;7:98061-8. doi: 10.1109/ACCESS.2019.2927866.
14. Ševo I, Avramovi'c A. Convolutional neural network based automatic object detection on aerial images. IEEE Geosci Remote Sens Lett. 2016;13: 740-4. doi: 10.1109/LGRS.2016.2542358.
15. Ochoa KS, Guo Z. A framework for the management of agricultural resources with automated aerial imagery detection. Comput Electron Agric. 2019; 162:53-69. doi: 10.1016/j.compag.2019.03.028.
16. Kampffmeyer M, Salberg A, Jenssen R. Semantic segmentation of small objects and modeling of uncertainty in urban remote sensing images using deep convolutional neural networks. In Proceedings of the 2016 IEEE Conference on Computer Vision and Pattern Recognition Workshops (CVPRW), Las Vegas, NV, USA, 26 June-1 July 2016; p. 680-688. doi: 10.1109/CVPRW.2016.90.
17. Azimi SM, Fischer P, Körner M, Reinartz P. Aerial LaneNet: Lane-marking semantic segmentation in aerial imagery using wavelet-enhanced cost-sensitive symmetric fully convolutional neural networks. IEEE Trans Geosci Remote Sens. 2019;57:2920-38. doi: 10.1109/TGRS.2018.2878510.
18. Mou L, Zhu XX. Vehicle instance segmentation from aerial image and video using a multitask learning residual fully convolutional network. IEEE Trans Geosci Remote Sens. 2018;56:6699-711. doi: 10.1109/TGRS.2018.2841808.
19. Benjdira B, Bazi Y, Koubaa A, Ouni K. Unsupervised domain adaptation using generative adversarial networks for semantic segmentation of aerial images. Remote Sens. 2019;11:1369. doi: 10.3390/rs11111369.
20. Jiao L, Zhang F, Liu F, Yang S, Li L, Feng Z, et al. A survey of deep learning-based object detection. IEEE Access. 2019;7:128837-68.
21. Lin TY, Maire M, Belongie S, Hays J, Perona P, Ramanan D, et al. Microsoft coco: Common objects in context. In European Conference on Computer Vision; Springer: Berlin/Heidelberg, Germany, 2014; p. 740-55.
22. Ren S, He K, Girshick R, Sun J. Faster R-CNN: Towards Real-time Object Detection with Region Proposal Networks. IEEE Trans Pattern Anal Mach Intell. 2017;39(6):1137-49. doi:10.1109/TPAMI.2016.2577031.
23. Redmon J, Farhadi A. YOLOv3: An Incremental Improvement. arXiv. 2018;arXiv:1804.02767.
24. Bochkovskiy A, Wang CY, Liao HYM. YOLOv4: Optimal speed and accuracy of object detection. arXiv. 2020;arXiv:2004.10934.

DOI: 10.60101/jarst.2023.254011

25. Youssouf N. Traffic sign classification using CNN and detection using faster-RCNN and YOLOV4. Heliyon. 2022;8(12):e11792.

26. Farid A, Hussain F, Khan K, Shahzad, Khan U, Mahmood Z. A fast and accurate real-time vehicle detection method using deep learning for unconstrained environments. MDPI Applied Sciences. 2023;13(5):3059. doi: 10.3390/app13053059.

27. Bochkovskiy A, Wang CY, Liao HYM. YOLOv4: Optimal speed and accuracy of object detection. arXiv preprint arXiv. 2004;10934.

28. Ren S, He K, Girshick R, Sun J. Faster R-CNN: Towards real-time object detection with region proposal networks. In Advances in Neural Information Processing Systems. 2015;91-9.

29. Liu W, Anguelov D, Erhan D, Szegedy C, Reed S, Fu CY, et al. SSD:Single shot multibox detector. In European Conference on Computer Vision. 2016; 21-37.

30. Isaac-Medina BKS, Poyser M, Organisciak D, Willcocks CG, Breckon TP, Shum HPH. Unmanned aerial vehicle visual detection and tracking using deep neural networks: A Performance benchmark. In Proceedings of the 2021 IEEE/CVF International Conference on Computer Vision Workshops (ICCVW), Montreal, BC, Canada, 11-17 October 2021; p. 1223-32.

31. Bewley A, Ge Z, Ott L, Ramos F, Upcroft B. Simple online and real-time tracking. In Proceedings of the 2016 IEEE International Conference on Image Processing (ICIP), Phoenix, AZ, USA, 25-28 September 2016; p. 3464-8.

32. Wojke N, Bewley A, Paulus D. Simple online and real-time tracking with a deep association metric. In Proceedings of the 2017 IEEE International Conference on Image Processing (ICIP), Beijing, China, 17-20 September 2017; p. 3645-9.

33. Wang Z, Zheng L, Liu Y, Li Y, Wang S. Towards real-time multi-object tracking. In Proceedings of the 16th European Conference, Glasgow, UK, 23-28 August 2020; p. 107-22.

34. Lu Z, Rathod V, Votel R, Huang J. RetinaTrack: Online single stage joint detection and tracking. In Proceedings of the 2020 IEEE/CVF Conference on Computer Vision and Pattern Recognition (CVPR), Seattle, WA, USA, 13-19 June 2020; p. 14656-66.

35. Bochkovskiy A, Wang CY, Mark Liao HY. YOLOv4: Optimal speed and accuracy of object detection. arXiv preprint arXiv. 2020;10934.

36. Ren S, He K, Girshick R, Sun J. Faster R-CNN: Towards real-time object detection with region proposal networks. In Advances in Neural Information Processing Systems (NIPS). 2015; 91-9.

37. Liu W, Anguelov D, Erhan D, Szegedy C, Reed S, Fu CY, et al. Berg. SSD: Single Shot Multibox detector. ECCV 2016: Computer Vision - ECCV. 2016;21-37.

38. Redmon J, Divvala S, Girshick R, Farhadi, A. You only look once: unified, real-time object detection. In: CVPR. 2016.

39. Ren S, He K, Girshick R, Sun J. Faster R-CNN: towards real-time object detection with region proposal networks. In: NIPS. 2015.

40. Szegedy C, Reed S, Erhan D, Anguelov D. Scalable, high-quality object detection. arXiv preprint v3. 2015;arXiv:1412.1441.

41. Erhan D, Szegedy C, Toshev A, Anguelov D. Scalable object detection using deep neural networks. In: CVPR. 2014.

42. Yurtsever E, Lambert J, Carballo A, Takeda K. A survey of autonomous driving: Common practices and emerging technologies. IEEE Access. 2020;8: 58443-69. doi: 10.1109/ACCESS.2020.2983149.

DOI: 10.60101/jarst.2023.254011

Institute of Research and Development
Rajamangala University of Technology Thanyaburi

39 M.1 Klong 6, Thanyaburi, Pathumthani 12110, Thailand
Tel. (02) 549-4492 Fax. (02) 577-5038, (02) 549-4680

Website : https://ird.rmutt.ac.th